Electrowetting Enhancement of Critical Heat Flux

A Dissertation

Presented to

the Faculty of the Department of Mechanical Engineering

University of Houston

In Partial Fulfillment

of the Requirements for the Degree

Doctor of Philosophy

in Mechanical Engineering

By

Yi Lu

May 2017

Electrowetting Enhancement of Critical Heat Flux

Yi Lu

Approved:

Chair of the Committee
Dong Liu, Associate Professor
Mechanical Engineering

Committee Members:

Paul Ruchhoeft, Associate Professor
Electrical Engineering

Anastassios Mavrokefalos, Assistant Professor, Mechanical Engineering

Hadi Ghasemi, Assistant Professor
Mechanical Engineering

Cunjiang Yu, Assistant Professor
Mechanical Engineering

Suresh K. Khator, Associate Dean
Cullen College of Engineering

Pradeep Sharma, Professor and Chair
Mechanical Engineering

Acknowledgement

I would like to express my gratitude to my advisor Dr. Dong Liu for guiding me throughout the course of my graduate education. His vast knowledge, mentoring, philosophical inputs and attention to details always illuminate me during the process of pursuing knowledge. With his patient guidance and encouragement, I could only achieve a better performance in both life and study. I would also like to thank my co-advisor, Dr. Paul Ruchhoeft, for his invaluable inputs, which have guaranteed the feasibility of many essential aspects of this work.

I would like to thank two graduated Ph.D students Dr. Aritra Sur and Dr. Carmen Pascente. I much appreciated for the working experience with Dr. Aritra Sur for his precursor research study at the beginning of this project with either respect to the experimental setup or group discussions. I am deeply grateful for Carmen's diligent work, which is the primary reason behind the development of the device used in this work.

I would also like to show great appreciation for all the professors during my study here in University of Houston for all your knowledge inputs and instructions both in class and research study. I would like to thank all the other lab fellow students for your kind help. I benefit immensely from study and working during your accompany.

I would like to thank my parents and all my family members. Thanks for your spiritual support while I am in the course of pursuing the Ph.D degree. Without you, I would not grow up and have the determinacy to overcome various challenges and difficulties that I came across in my life. At last I want to thank all my friends for your tremendous help. Thank you! Everyone.

Electrowetting Enhancement of Critical Heat Flux

An Abstract

Of

A Dissertation

Presented to

the Faculty of the Department of Mechanical Engineering

University of Houston

In Partial Fulfillment

of the Requirements for the Degree

Doctor of Philosophy

in Mechanical Engineering

By

Yi Lu

May 2017

Abstract

Critical heat flux (CHF) represents the upper limit of nucleate boiling heat transfer, beyond which boiling transitions to the inefficient film boiling regime. Potentially catastrophic burnout conditions may ensue and endanger the safe and reliable operation of the boiling device. Thus, it is highly desirable to augment CHF in order to boost the thermal performance of various energy-intensive applications that rely on boiling to transport a large amount of thermal energy.

In this work, CHF enhancement was explored both theoretically and experimentally by capitalizing on the ability of electrowetting (EW) to modulate the liquid-vapor interfacial stabilities and the liquid-vapor-solid three-phase contact line motion. To do so, a Leidenfrost drop (i.e., a liquid drop hovering over a highly superheated solid surface) was first employed as a model system, due to its simplicity and close connection to film boiling and CHF, to investigate the effect of the electric field on the dynamics of the vapor film that separates the drop from the hot surface. It was found that the electrostatic attraction force alone cannot destabilize the vapor film, instead, it is the accelerated vapor flow that changes the critical wavelength of the Kelvin-Helmholtz instability, thus causing the film to collapse. The results show that, without the need for any complicated surface micro/nanostructures, the Leidenfrost point (LFP) temperature of water can be increased from 200°C to 380°C with a moderate voltage of 56 V a frequency of 50 Hz.

Subsequently, to better understand the impact of EW on the liquid-vapor interfacial behaviors, the dynamics of EW-induced motion of both liquid droplets and vapor bubbles was studied. Computational fluid dynamics models were developed by using the Volume of Fluid (VOF)-Continuous Surface Force (CSF) method to scrutinize the response of a

droplet when subject to EW actuating signals. In particular, a dynamic contact angle model based on the molecular kinetic theory was implemented as the boundary condition at the moving contact line, which considers the effects of both the contact line friction and the pinning force. The droplet shape evolution and the interfacial resonance oscillation were investigated in detail. On the bubble aspect, the nucleation, growth and departure of vapor bubbles on a hydrophilic surface, a hydrophobic surface both with and without the influence of EW, were compared, which revealed the significant effect of the EW force on the contact line and, therefore, on the bubble dynamics.

Lastly, to demonstrate the EW enhancement of CHF, a synchronized high-speed optical imaging and infrared (IR) thermographic technique was used to characterize boiling heat transfer at the CHF conditions. Simultaneous measurements of the bubble dynamics and the wall temperature and heat flux distributions on the boiling surface were acquired. The results showed that CHF can be enhanced by 133% by the use of EW. Additionally, by considering the force balance at the contact line of a nucleate bubble, a theoretical model was developed to delineate the threshold conditions for CHF to occur, which show very good agreement with the experimental measurements.

Table of contents

List of figures

List of tables

Nomenclature

θ_{app}, Apparent contact angle of droplet [^{o}];

θ_d, Apparent contact angle of droplet [^{o}];

θ, Young's contact angle with hydrophobic surface [^{o}];

σ_{lv}, Surface tension between liquid and vapor [N/m];

k_v, Thermal conductivity of vapor at saturation condition [W/(mK)];

h_{lv}, Latent heat at saturation condition [kJ/kg];

T_{sat}, Water saturation temperature at 1 atm [^{o}C];

T_w, Temperature of wall [^{o}C];

σ, Conductance of liquid at saturation conditions [S/m];

μ_l, Liquid viscosity [Pa·s];

μ_v, Vapor viscosity [Pa·s];

ς, Contact line friction coefficient [N·s/m^2];

ρ_l, Density of liquid [kg/m^3];

ρ_v, Density of vapor [kg/m^3];

$\Delta\rho$, Density difference between liquid and vapor [kg/m^3];

ρ_f, Volume density of free electric charge [C/m^3];

u_{cl}, Velocity of contact line [m/s];

u_m, Average Vapor velocity in vapor layer of Leidenfrost droplet [m/s];

$v_{z=\delta}$, Evaporation vapor velocity at droplet bottom interface [m/s];

ε_0, Vacuum permittivity [F/m];

ε_v, Vapor relative permittivity;

ε_l, Liquid relative permittivity;

ε_{eq}, Equivalent permittivity [F/m];

d, Thickness of dielectric layer [nm];

δ, Thickness of Leidenfrost vapor layer [μm];

r_0, Contact radius of droplet [mm];

R, Radius of droplet [mm];

d_d, Bubble departure diameter [mm];

D_c, Diameter of bubble at CHF conditions [mm];

H, Height of Leidenfrost droplet or bubble in CHF condition [mm];

V, Bubble volume [μl];

λ, wavelength of surface waves [mm];

λ_c, Critical wavelength [mm];

λ_D, Most dangerous wavelength [mm];

λ_H, Helmholtz wavelength [mm];

t_w, Waiting time of bubble nucleation [s];

t_g, Growth time of bubble nucleation [s];

k, wavenumber of interfacial waves [mm^{-1}];

k_c, Critical wavenumber of interfacial waves [mm^{-1}];

f, Frequency of bubble release [Hz];

f_c, Crossover frequency [Hz];

f_E, Actuation frequency [Hz];

f_n, Resonance frequency [Hz];

f_r, Charge relaxation frequency [Hz];

ω, Angular frequency of electric signal [Hz];

s, Angular frequency of interfacial wave growth [Hz];

E_0, Applied electric field of a non-deformed interface [V/m];

E_v, Electric strength in vapor layer [V/m];

F_i, Droplet inertia force [N/m]

F_v, Droplet viscous force [N/m]

F_c, Droplet capillary force [N/m];

F_v, Droplet contact line force [N/m];

F_{up}, Viscous pressure in the vapor layer [N];

α_s, Volume fraction of secondary phase;

α_p, Volume fraction of primary phase;

P_{atm}, Pressure at 1 atm [Pa];

U, DC voltage [V];

$U(t)$, AC sinusoidal voltage [V];

U_{rms}, Root mean square value of $U(t)$ [V];

C, Capillary number;

$Nu_{b,E}$, Nussle's number of micro-convection under EW;

$Re_{b,E}$, Reynold's number of micro-convection under EW;

Chapter 1 Introduction

Boiling has been employed for transferring a large amount of thermal energy in a broad range of industries, such as power generation, chemical processing, desalination, refrigeration and electronics thermal management. When the thermal load exceeds critical heat flux (CHF), the heat transfer surface is covered by a continuous vapor layer and film boiling occurs. The insulating vapor film severely deteriorates the boiling heat transfer and causes the wall temperature to rise drastically, eventually leading to catastrophic burnout of the boiling surface. The key to enhance CHF lies in re-establishing and maintaining the liquid-solid contact or, in other words, destabilizing the vapor film. Film boiling is highly sensitive to external perturbations, especially those arising from the interactions between the liquid-vapor interface and the solid surface (Bradfield, 1966; Vakarelski, Patankar, Marston, Chan, & Thoroddsen, 2012). In current CHF augmentation, various surface modifications are engineered to subvert film boiling by tailoring the surface characteristics, such as wettability, roughness and porosity (Ho Seon Ahn & Moo Hwan Kim, 2012; Bhavnani et al., 2014; D. E. Kim, Yu, Jerng, Kim, & Ahn, 2015; Y.-W. Lu & Kandlikar, 2011; Shojaeian & Koşar, 2015). Unfortunately, even with the surface enhancement, the highest CHF available to date for water at atmospheric pressure (600 W/cm^2) is still almost two orders of magnitude lower than the theoretical maximum (22,300 W/cm^2) (Bai, Zhang, Lin, & Peterson, 2016; Gambill & Lienhard, 1989), and the typical CHF in pool boiling experiments lingers around 200 W/cm^2 (Ho Seon Ahn, Jo, Kang, & Kim, 2011; R. Chen et al., 2009; K.-H. Chu, Enright, & Wang, 2012; K.-H. Chu, Soo Joung, Enright, Buie, & Wang, 2013; Dhillon, Buongiorno, &

Varanasi, 2015; Jun, Kim, Son, Kim, & You, 2016). Hence, CHF remains the dominant factor that limits the safe operation and efficient performance of practical boiling systems.

The present research aims to explore a new paradigm for CHF enhancement by using the ability of electrowetting (EW) to modulate the liquid-vapor interfacial stabilities and the liquid-vapor-solid three-phase contact line motion. Subsequently, the film boiling regime can be subverted to the more efficient nucleate boiling regime or the latter can be prolonged to higher CHF conditions. This work was inspired by the findings from an earlier study on electrowetting-enhanced nucleate boiling heat transfer (Y. Lu, Sur, A., Pascente, C., Ruchhoeft, P., and Liu, D., 2016; A. Sur, 2014; A. Sur, Lu, Y., Pascente, C., Ruchhoeft, P., and Liu, D., 2016). The experimental observations in that work revealed that the stable liquid-vapor interface in film boiling suddenly collapses upon the application of an EW signal, and the CHF is improved by 115% for water on a Teflon-coated silicon surface. However, the fundamental mechanisms underlying the EW enhancement remain largely elusive, owing to the experimentation complexities as well as the lack of a clear theoretical framework that couples the electromechanics to the interfacial instabilities during a phase change process. To address these issues, EW enhancement of CHF is investigated both experimentally and theoretically in this research in order to elucidate the effects of EW on the interfacial stabilities and phase transition in film boiling. The following specific research goals are proposed:

- To conduct pool boiling heat transfer experiments to demonstrate CHF can be augmented effectively by EW.
- To design experiments to explore the interfacial destabilization and the suppression effect by EW.

- To formulate theoretical and numerical models to understand the key constitutive processes physical mechanisms of EW-enhancement of CHF.
- To validate the theoretical and numerical models with experimental data.

To achieve these goals, a synergistic experimental, theoretical and numerical methodology is used to conduct the proposed work.

1) Droplet dynamics induced by EW is investigated to acquire the basic knowledge of the impact of EW on the liquid-vapor interfacial behaviors.

2) A Leidenfrost droplet system, drawn on its simplicity and close linkage to film boiling, is studied to establish the basic relationship between the control parameter of EW and the interfacial dynamics.

3) The boiling regime transition, boiling heat transfer and CHF enhancement is investigated in a pool boiling test facility. A synthesized high-speed optical imaging and infrared thermography method is utilized to obtain simultaneous measurements of the interfacial profile, bubble dynamics, local wall temperature and heat flux distributions.

4) Theoretical and numerical models are developed using the interfacial stability analysis and the volume of fluid (VOF) method, respectively, to understand various aspects of the EW-modulated droplet dynamics and CHF enhancement.

This Ph.D. dissertation is organized as follows. Chapter 2 presents the study of the dynamics of EW-induced droplet motion to lay the necessary foundation of EW. Chapter 3 describes the experimental and theoretical investigation of the EW suppression of Leidenfrost state of a droplet to highlight the impact of EW on the liquid-vapor interfacial instabilities. Chapter 4 details the experimental demonstration and the theoretical analysis of EW enhancement of CHF. Chapter 5 discusses the bubble dynamics of vapor bubbles under the influence of EW. Finally, the conclusions of the present study and recommendations for future work are summarized in Chapter 6.

Chapter 2 Dynamics of droplet motion induced by EW

2.1 Literature Review

Droplet spreading and oscillation on a solid substrate has attracted great research interest due to its relevance in a variety of engineering applications, such as droplet-based microfluidics (Mugele & Baret, 2005), opto-fluidic optical attenuators (Kuiper & Hendriks, 2004; Roques-Carmes, Hayes, & Schlangen, 2004) and reflective displays (Hayes & Feenstra, 2003), etc. Among various approaches to control the droplet motion, electrowetting (EW) is particularly convenient and versatile for its ability to tune the surface wetting property with an external electric field. With EW, it is now possible to design digitized active and reconfigurable cooling devices for high-flux thermal management of compact microsystems (Baird & Mohseni, 2008; Cha, Kim, & Ju, 2016; Garimella, Persoons, Weibel, & Yeh, 2013; Hale & Bahadur, 2015). EW originates from the electrical force concentrated at the three-phase contact line (TCL), which causes the apparent contact angle θ_{app} to deviate from the inherent equilibrium value θ_e. The EW-induced contact angle variation can be described by the Young-Lippmann equation

$$\cos\theta_{\mathrm{app}} = \cos\theta_{\mathrm{e}} + \frac{\varepsilon_0\varepsilon_r}{2d\sigma_{lv}}U^2, \tag{2.5.1}$$

where ε_0 is the vacuum permittivity constant, ε_r the relative permittivity of the insulating dielectric layer, d the thickness of the dielectric layer, σ_{lv} the surface tension of the liquid-vapor interface, and U the applied voltage.

As the foundation of EW theory, Eq. (2.5.1) has been widely used to predict the EW response of liquid droplets (L. Chen & Bonaccurso, 2014; Kang, 2002; Paneru, Priest, Sedev, & Ralston, 2010). It is expected to hold as long as the applied voltage is below the thresholds for contact angle saturation (i.e., the contact angle reaches a limiting value irrespective of further increase in voltage) and edge instability (i.e., satellite droplets are disintegrated from the mother droplet) (Mugele & Baret, 2005). However, the resulting θ_{app} only accounts for the final state of a droplet after it reaches the equilibrium. It has been long known that the static contact angle (SCA) concept is inadequate in dealing with the transient processes, where the droplet deforms as a function of time and θ_{app} varies between the limits set by the advancing and receding contact angles (Dussan, 1979; Hoffman, 1975). In EW, θ_{app} is affected by the interplay of the inertial, viscous, capillary, electrical and contact line friction forces, and may deviate significantly from the static prediction by Eq. (2.5.1) (T. D. Blake, Clarke, & Stattersfield, 2000; Decamps & De Coninck, 2000). Moreover, both direct current (DC) and alternating current (AC) signals can be applied to induce EW (referred to DCEW and ACEW, respectively, in this paper). The temporal evolution of a droplet in ACEW also depends on the relative magnitudes of the natural resonant frequency of the droplet, f_N, the driving frequency of the electric field, f, the charge relaxation frequency

$$\mathrm{f_r} = \sigma/\varepsilon_0\varepsilon_\mathrm{r}, \tag{2.5.2}$$

and the crossover frequency

$$\mathrm{f_c} = \frac{\sigma}{\left[\varepsilon_\mathrm{f}+\varepsilon_\mathrm{r}\left(\frac{\mathrm{R_d}}{\mathrm{d}}\right)\right]}, \tag{2.5.3}$$

where σ and ε_f are the electrical conductivity and the relative permittivity of the fluid, and R_d the characteristic size of the droplet. Therefore, a dynamic contact angle (DCA) model, rather than Eq. (2.5.1), must be employed to fully characterize the droplet motion under electrowetting actuation.

Historically, both the hydrodynamic theory (Cox, 1986a, 1998) and the molecular kinetic theory (MKT) (T. D. Blake & Haynes, 1969) have been developed to model the DCA of a droplet that is displacing on a solid surface. The hydrodynamic theory attributes the deviation of the DCA from SCA to bulk viscous dissipation in the liquid front near the moving contact line, whereas the MKT takes into account the friction force owing to the adsorption or desorption of fluid particles at the immediate vicinity of the contact line (Terence D. Blake, 2006). Past studies suggest the MKT is more suitable for the study of EW as it can be applied to a wider range of contact line velocities (3.16×10^{-5} – 10 m/s) (Ranabothu, Karnezis, & Dai, 2005) and offers a straightforward explanation of the contact angle hysteresis phenomenon, thereby yielding more accurate predictions of the droplet dynamics (Annapragada, Murthy, & Garimella, 2012; Jung Min Oh, Ko, & Kang, 2010; X. D. Wang, Peng, & Lee, 2003). Recently, a few experimental and numerical studies have successfully demonstrated the validity of MKT in DCEW applications (Annapragada, Dash, Garimella, & Murthy, 2011; T. D. Blake et al., 2000; Decamps & De Coninck, 2000; J. Hong, Kim, Kang, Oh, & Kang, 2013; S. J. Hong, Hong, Seo, Lee, & Chung, 2015; Keshavarz-Motamed, Kadem, & Dolatabadi, 2010; K. L. Wang & Jones, 2005). In particular, Keshavarz-Motamed et al. (Keshavarz-Motamed et al., 2010) implemented a MKT-based DCA model in the numerical simulation of droplet displacement in a parallel plate microchannel. The results revealed that the dynamic features of wetting must be considered, or the simulation will overestimate the effects of EW actuation, including the contact angle, aspect ratio and velocity of the droplet. By combining MKT with an idealized drop geometry, Annapragada et al. (Annapragada et al., 2011) investigated the EW response of a droplet to a DC step input signal, and formulated a kinematic equation for the time-dependent spreading of the drop on the substrate, which correctly predicted the overall trend of the contact line motion.

The utility of DCA models in ACEW analysis is further complicated by the presence of time-harmonic shape oscillations at the free surface of the droplet (J. Hong, Kim, Kang, Kim, & Lee, 2014; Mugele, Baret, & Steinhauser, 2006; Jung Min Oh, Ko, & Kang, 2008). The basic assumptions commonly adopted for DCEW, such as a quasi-steady state, the spherical cap shape of the droplet and the negligence of inertia, are no longer valid for ACEW. Consequently, most available theoretical and numerical studies of ACEW chose to circumvent the complexities involving DCA. Oh et al. (Jung Min Oh et al., 2008) conducted a theoretical analysis of interfacial oscillations of a droplet in ACEW by applying a domain perturbation method. The oscillating droplet was regarded as a half-region of a spherical drop in an unbounded domain, and its shape was represented by a linear combination of an infinite number of shape modes. This model was able to qualitatively reproduce the resonance modes observed in the experiments, but, since the capillary force and the contact line friction were completely omitted, it was only valid for weak viscous effect and small drop deformations. Ashoke Raman et al. (Ashoke Raman, Jaiman, Lee, & Low, 2016) numerically investigated the dynamics of ACEW-induced droplet jumping by the means of a high-density ratio based lattice Boltzmann method (LBM). The SCA model (Eq. (2.5.1)) was used together with a geometric formulation to describe the wetting boundary condition. The findings revealed some interesting features of the droplet lift-off and transport mechanism, however, no experimental validation was provided. Hong et al. (J. S. Hong, Ko, Kang, & Kang, 2007) employed an effective electrical wetting tension at the contact line to model the effect of electric field on the droplet wetting behavior. By treating the ACEW response as a quasi-electrostatic problem, they analyzed the AC electric field around the droplet and computed the electrical wetting tension from the integration of the Maxwell stress. The results were then applied in a varied form to acquire the time-averaged contact angle at different actuating frequencies. In a study of droplet dynamics in ACEW, Li et al. (Z. Li, Zhou, & Hu, 2012) followed the electrical wetting tension concept but used a dissipative particle dynamics (DPD) approach, which is a modified version of the lattice gas method by replacing single fluid molecules with coarse-grained particle clusters. Unfortunately, only the oscillations of a sub-micrometer droplet in ACEW were explored due to the computational limits of the DPD approach. Recently, Li et al. (X. L. Li, He, & Zhang, 2013) presented the first numerical simulation of droplet oscillation in ACEW that incorporated a DCA model to describe the contact line motion. They used an axisymmetric model, in conjunction with the moving mesh interface tracking (MMIT) method, for solving the Navier-Stokes equations. This study focused on the resonance phenomenon and the oscillation patterns at different actuating frequencies.

Gaining a fundamental understanding of the droplet dynamics is crucial to the performance prediction and design of current and future EW-based devices. The literature survey reveals that the available numerical and theoretical methods are inadequate in accurately simulating the complex electrohydrodynamic transport associated with EW, especially ACEW. Thus, it is the aim of the present study to overcome the deficiencies of existing numerical models and to provide more in-depth insights into the dynamics of EW-induced droplet motion. The rest of the paper is organized as follows. First, the elementary DCA models from the hydrodynamic theory and MKT are briefly reviewed. Then, the experimental setup for both DCEW and ACEW tests is presented. Subsequently, the numerical methods using VOF method are presented in detail. At last, the numerical predictions are validated with the experimental measurements and the key characteristics of the EW-induced droplet dynamics are discussed.

2.2 Dynamic contact angle model of EW actuated droplet

2.2.1 Dynamic contact angle in electrowetting

The dynamics of droplet motion can be quantified by the dynamic contact angle, θ_d, and the contact line velocity, u_{cl}, i.e., the velocity at which the liquid front moves across the solid surface. Hence, a certain relation is expected between θ_d and u_{cl} for a given system. Classical hydrodynamic models attribute the observed DCA to viscous bending of the liquid-vapor interface at a mesoscopic region near the contact line. The bulk viscous dissipation is assumed to be the dominant resistance to the contact line motion. However, solving the flow field alone does not yield a physically meaningful solution because a conceptual conflict exists between a moving contact line and the no-slip boundary condition at the solid wall, which predicts an unbounded stress at the contact line and an infinite force on the wall. To eliminate the singularity, hydrodynamic models separate the liquid into an outer region, where the conventional no-ship boundary is still applicable, and an inner region, where the continuum description breaks down and the fluid slippage occurs in the first couple of layers of liquid molecules adjacent to the wall. The resulting correlation describes the DCA in terms of the capillary number, *Ca* (Cox, 1986b; Schneemilch, Hayes, Petrov, & Ralston, 1998) as

$$\theta_d^3 - \theta_e^3 = \pm 9\mathrm{Ca}\ln\left(\frac{L'}{L_m}\right), \tag{2.6.1}$$

where $\mathrm{Ca} = \mu_l u_{cl}/\sigma_{lv}$ and η is the liquid viscosity. In Eq. (2.6.1), L' and L_m are the macroscopic and microscopic length scales for the outer and inner regions, respectively, and the plus sign applies to an advancing liquid front whereas the minus sign applies to a receding liquid movement. For small *Ca*, Eq. (2.6.1) can be approximated by the Hoffman-Voinov-Tanner law (Hoffman, 1975; Tanner, 1979; Voinov) as

$$\theta_d^3 - \theta_e^3 = C_T Ca, \tag{2.6.2}$$

where C_T is a numerical constant ($C_T \approx 72$). In contrast, by adopting the Frenkel/Eyring view of liquid transport (Frenkel, 1946; Glasstone, 1941), the MKT treats the contact line motion as a series of adsorption and desorption events of liquid molecules on the solid wall. Thus, the energy dissipation is not due to the bulk viscous flow, but rather the result of the attachment and detachment of fluid particles at the immediate vicinity of the contact line. In this theory, the velocity of the contact line is determined by the equilibrium frequency of the random molecular displacement, k^0, and the average length of each displacement, λ. Thus, the velocity-dependence of the DCA is attributed to the disturbance of adsorption equilibria and the subsequent out-of-balance surface tension, $F_w = \sigma_{lv}(\cos\theta_e - \cos\theta_d)$, acting as the driving force. The subsequent equation for the contact line velocity is

$$u_{cl} = 2k^0\lambda \sinh[\sigma_{lv}(\cos\theta_e - \cos\theta_d)\lambda^2/2k_B T], \tag{2.6.3}$$

where k_B is the Boltzmann constant and T the absolute temperature. If the value of the sinh function is sufficiently small, Eq. (2.6.3) reduces to

$$u_{cl} \approx \frac{k^0\lambda^3\sigma_{lv}(\cos\theta_e - \cos\theta_d)}{k_B T} = \sigma_{lv}(\cos\theta_e - \cos\theta_d)/\varsigma, \tag{2.6.4}$$

where $\varsigma = k_B T/k^0\lambda^3$ is called the coefficient of contact line friction. The physical implication of Eq.(2.6.4) becomes more evident if it is recast in the form of balance of forces at the contact line

$$\sigma_{lv}\cos\theta_d = F_c + F_{cl}, \tag{2.6.5}$$

where the capillary force is represented by $F_c = \sigma_{lv} \cos\theta_e$ and the contact line friction force is $F_{cl} = -\varsigma u_{cl}$.

In electrowetting, the contact line is made to move by the induced electrical force. To represent this effect, the force balance equation is modified as (Jung Min Oh et al., 2010)

$$\sigma_{lv} \cos\theta_d = F_{EW} + F_c + F_{cl}, \tag{2.6.6}$$

where F_{EW} is the electrical force

$$F_{EW} = \frac{\epsilon_0 \epsilon_r U^2}{2d}. \tag{2.6.7}$$

It is noted that, if the actuating frequency f exceeds f_c (given by Eq. (2.5.3)), the frequency-dependent electrical properties must be considered when solving for the electrowetting force (J. S. Hong et al., 2007; Mugele & Baret, 2005). As will be shown later, f_c is estimated to be 2.4 kHz in this study, one order of magnitude higher than f, which varies between 0 and 200 Hz. Thus, the droplet is expected to behave like a conductor, and Eq. (2.6.7) offers an adequate description of the electrical force for both DCEW and ACEW in the present work. Further, considering the pinned edge model (Walker, Shapiro, & Nochetto, 2009), a pinning force term, F_{pin}, is added to the expression of F_{cl} as

$$F_{pin} = c_{pin}\mathrm{sgn}(u_{cl}) - \frac{c_{pin}}{\pi/2}\tanh^{-1}\left[\frac{\varsigma u_{cl}}{c_{pin}/(\pi/2)}\right], \tag{2.6.8}$$

which represents the maximum force that can resist the motion of the droplet. c_{pin} is determined from the contact angle hysteresis effect (Jung Min Oh et al., 2010). Equation (2.6.8) indicates the pinning force attains its maximum, $c_{pin}sgn(u_{cl})$, when the contact line is about to move, and vanishes if u_{cl} becomes sufficiently high. Accordingly, the friction force becomes

$$F_{cl} = -\left\{ \varsigma u_{cl} + c_{pin} \operatorname{sgn}(u_{cl}) - \frac{c_{pin}}{\pi/2} \tanh^{-1}\left[\frac{\varsigma u_{cl}}{c_{pin}/(\pi/2)}\right]\right\}. \qquad (2.6.9)$$

Combining Eqs. (2.6.6), (2.6.7) and (2.6.9), the following DCA relationship is developed as

$$\theta_d = \cos^{-1}\left\{\cos\theta_e + \frac{\epsilon_0\epsilon_r}{2d\sigma_{lv}}U^2 - \left[\varsigma u_{cl} + c_{pin}\operatorname{sgn}(u_{cl}) - \frac{c_{pin}}{\pi/2}\tanh^{-1}\left[\frac{\varsigma u_{cl}}{c_{pin}/(\pi/2)}\right]\right]/\sigma_{lv}\right\}. \qquad (2.6.10)$$

This DCA model will be applied as a key boundary condition in the numerical simulations of EW.

2.3 Experimental Setup

The experimental apparatus for the electrowetting tests is shown in Figure 2.1.

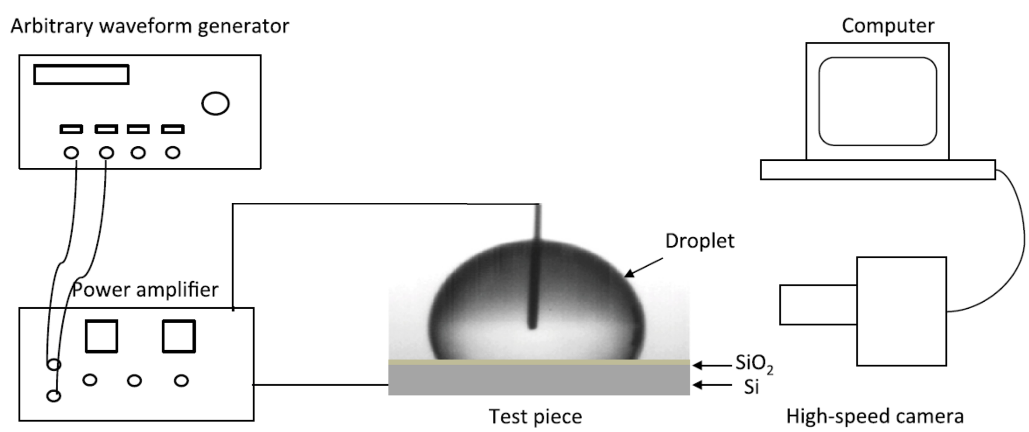

Figure 2.1. Experimental setup for EW tests

It consisted of the test piece, the control circuit and the imaging system. The test piece was made of a 3” silicon wafer (Silicon Quest) with a 500-nm-thick, thermally grown silicon dioxide (SiO_2) layer (ε_r = 3.9). A thin layer (70 nm) of Teflon (AF2400, Dupont) was spin-coated on the wafer to produce the hydrophobic surface. To improve the adhesion of Teflon to SiO_2, a silane-based adhesion promoter (FSM-660-4, Cytonix) was dip-coated on SiO_2 before the spin-coating procedure. Since silicon has a reasonable electrical conductivity (1.56×10^{-3} S/m at 20°C), the substrate works directly as the ground electrode. Before the experiment, a 9.0 ± 0.1 μL deionized water droplet was dispensed gently onto the test piece with a micropipette. A 99.99% pure platinum wire of a 100-μm diameter was inserted into the droplet from the top as the actuating electrode (as shown in Figure 2.1). Since the experiments were conducted at room temperature and each test only lasted for a few seconds, the effect of evaporation was negligible and the droplet volume was assumed constant. The properties of water are: electrical conductivity $\sigma = 2\times10^{-4}$ S/m, relative permittivity ε_f = 88, density $\rho_l = 998$ kg/m^3, viscosity $\mu_l = 1.002\times10^{-3}$ Pa·s, and surface tension $\sigma_{lv} =$ 0.0728 N/m. For a characteristic droplet size R_d = 1.18 mm, Eq. (2.5.3) yields a crossover frequency of $f_c \approx 2.4$ kHz.

The actuation signals for EW were provided by an arbitrary waveform generator (Fluke 294-U, Fluke) in combination with an inverting power amplifier (BOP 200-1D BIT 4886, KEPCO). A step-function signal was used for DCEW tests, and sinusoidal functions of various frequencies were applied to actuate ACEW. The EW response of the droplet was recorded at 6,000 – 10,000 frame per second (fps) using a high-speed video camera (FASTCAM Ultima APX, Photron). The shutter speed was set to 1/16000 s, and a cold light illumination source was used to compensate for the short exposure time at high frame rates. A Nikon 18-105 mm lens (f 3-5.6) was employed to observe the details of the droplet motion. The pixel resolution ranges from 17.1 μm to 33.5 μm, depending on the distance from the droplet to the lens. The control circuit and the imaging system were synchronized using a pulse generator (BNC 565, Berkeley Nucleonics).

Once the droplet motion was recorded, the stream of static images were extracted from the video and analyzed using an in-house image-processing program developed in MATLAB. The measurements included the instantaneous contact angle (θ_d), the contact radius (R) of the wetted spot on the wall and the height of the droplet. The experimental uncertainties in the contact angle and contact radius/height measurements are ± 2° and ± 0.02 mm, respectively. A subpixel smoothing method and a high-order polynomial fitting algorithm (Atefi, Mann, & Tavana, 2013) were employed to precisely identify the droplet profile and the contact points of the droplet with the solid surface. In particular, the polar coordinate system was used to fit the droplet profile with a fourth order polynomial. The tangent to the droplet profile at the contact point was used to determine the CA. The intrinsic CA of a water droplet on the Teflon surface was measured to be 118° ± 2° and the initial contact radius was $R_0 = 1.18 \pm 0.02$ mm.

2.4 VOF Model of simulating EW droplet

Numerous studies have demonstrated the effectiveness of the volume of fluid (VOF) method in predicting the droplet motion on a solid surface (Bussmann, Mostaghimi, & Chandra, 1999; Hirt & Nichols, 1981; Lunkad, Buwa, & Nigam, 2007; Sikalo, Tropea, & Ganic, 2005; Yokoi, Vadillo, Hinch, & Hutchings, 2009). In the current work, the VOF-Continuum Surface Force (CSF) model was used in the commercial computational fluid dynamics (CFD) software package, FLUENT, to investigate the transient droplet dynamics under the influence of DCEW and ACEW. Special attention was given to take care of two main challenges: (1) the prescription of the boundary condition at the moving contact line, and (2) the incorporation of the DCA model in the computation.

2.4.1 VOF-SCF model

The VOF model tracks the time-dependent deformation of the interface by computing the distribution of the volume fraction of two immiscible fluids in the computational domain. The volume fraction of a secondary phase, a_s, is obtained by solving the continuity equation

$$\frac{\partial \alpha_s}{\partial t} + \nabla\left(\alpha_s \bar{u}\right) = 0, \tag{2.7.1}$$

The volume fraction of the primary phase, a_p, can be computed from

$$\alpha_p = 1 - \alpha_s. \tag{2.7.2}$$

Here, $a_s = 1$ represents a computational cell that is completely occupied by the gas phase, and $a_s = 0.5$ is taken to be the location of the liquid-gas interface. The thermal physical properties in a single cell, such as the density and viscosity, are calculated as the volume average

$$\rho = \alpha_s \rho_s + \alpha_p \alpha_p \text{ and} \tag{2.7.3}$$

$$\mu = \alpha_s \mu_s + \alpha_p \mu_p \tag{2.7.4}$$

A single set of Navier-Stokes equations is solved for the average velocity of the mixture, which is shared by all the phases

$$\frac{\partial}{\partial t}\left(\rho \bar{u}\right) + \nabla\left(\rho \bar{u}\bar{u}\right) = -\nabla p + \nabla \cdot \left[\mu\left(\nabla \bar{u} + \overline{\nabla u}^{T}\right)\right] + \rho \bar{g} + \vec{F}, \tag{2.7.5}$$

where p, $\vec{g}$ and $\vec{F}$ are the pressure, gravitational acceleration and body force, respectively. For computational cells that are not at the liquid-vapor interface, only one phase is present and just $\vec{g}$ needs to be considered. For the interfacial cells, instead of treating the surface tension as a pressure jump boundary condition across the interface, an equivalent volumetric body force $\vec{F}$ is considered using the CSF formulation (Brackbill, Kothe, & Zemach, 1992). For a two-phases system, $\vec{F}$ is given as

$$\vec{F} = \sigma_{lv} \frac{2\rho\kappa_s \nabla \alpha_s}{\left(\rho_p + \rho_s\right)}, \tag{2.7.6}$$

where κ_s is the interfacial curvature for the second phase, and $\vec{n}$ is the unit vector normal to the interface

$$\kappa_s = -\left(\nabla \cdot \vec{n}\right) \text{ and} \tag{2.7.7}$$

$$\vec{n} = \nabla \alpha_s / \left|\nabla \alpha_s\right|. \tag{2.7.8}$$

The interfacial shape at the contact line is imposed by specifying the unit normal using the contact angle

$$\vec{n} = \vec{n}_w \cos\theta_w + \vec{t}_w \sin\theta_w, \tag{2.7.9}$$

where $\hat{n}_w$ and $\hat{t}_w$ are the unit vectors normal and tangential to the wall, which are directed into the fluid and the wall, respectively.

2.4.2 Computational model

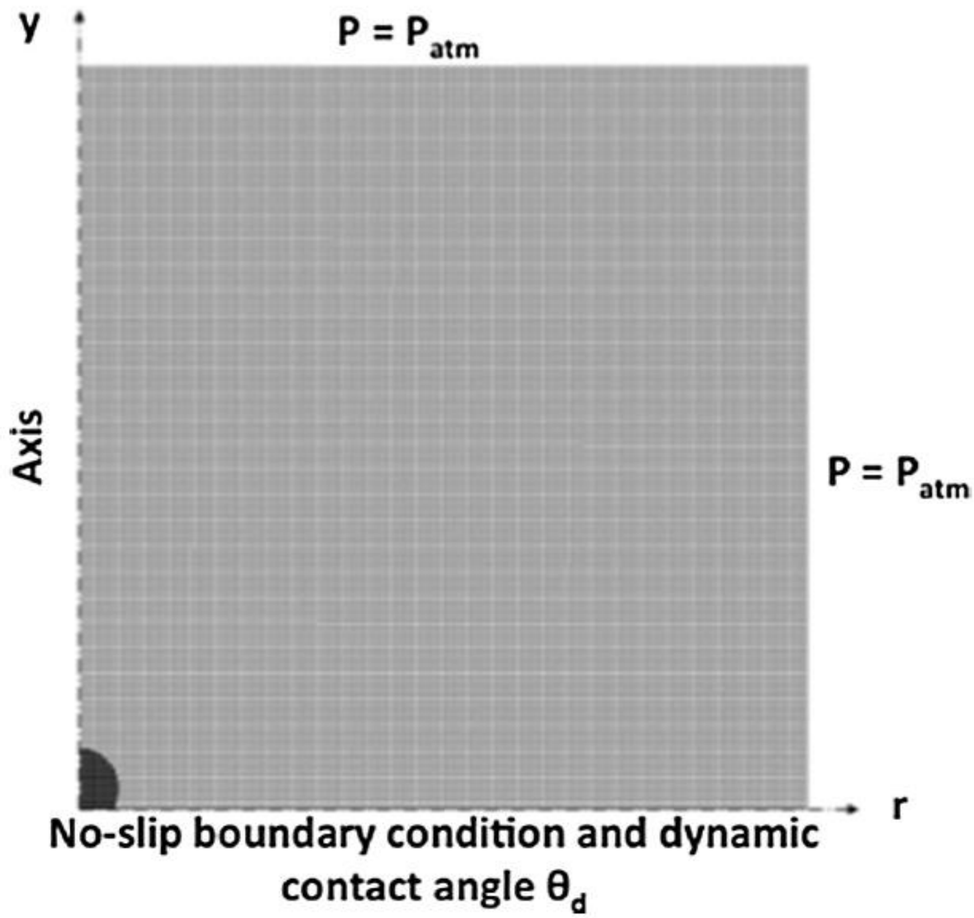

Figure 2.2. Computational domain and the boundary conditions

The computational domain is illustrated in Figure 2.2, where a truncated spherical drop of water (shown as the shaded black) is patched at the corner of the domain. The initial contact angle and contact radius were 118° and 1.18 mm, respectively. The shape change owing to the insertion of the electrode from the top of the droplet was neglected. Due to the axisymmetric nature of the drop geometry, a 2D axisymmetric VOF model was developed in FLUENT. A no-slip boundary condition was specified at the bottom wall.

The upper and right boundaries were set as at ambient pressure ($P = P_{atm}$). A rather large domain size of 24 mm × 24 mm was chosen in order to eliminate the effect of boundary-induced disturbances.

2.4.3 DCA implementation in VOF

In the VOF-CSF simulations, the MKT-based DCA model was applied as a boundary condition at the contact line via user-defined functions (UDFs). According to Eq. (2.6.10), the required inputs include the applied voltage $U(t)$, the contact line velocity $u_{cl}\left(t\right)$, the frictional coefficient ζ, and the pinning force c_{pin}..

A step input voltage was used to actuate DCEW, and sinusoidal signals with various driving frequencies (f) were used for ACEW

$$\mathrm{U(t) = U_0 sin(2\pi ft).} \qquad (2.7.10)$$

In the following discussion, the AC signal will be reported in terms of its root mean square (RMS) value, i.e., $U_{RMS} = U_0 / \sqrt{2}$.

Obtaining a rigorous estimate of the velocity of the contact line, $u_{cl}\left(t\right)$, is challenging, due to the singularity dilemma at the contact line (Roisman et al., 2008; X. D. Wang et al., 2003; Yokoi et al., 2009). If the no-slip condition is specified on the solid wall, the contact line cannot move. However, the contact line does move in reality, thereby leading to an infinite viscous shear and a diverging drag force on the wall. To avoid this, a Navier-slip boundary condition, $u_{slip} = \lambda \partial u / \partial y$, can be used to represent the contact line motion as a slip, where λ is the slip length, i.e., the distance from the boundary where a linearly extrapolated velocity profile would reach zero. Unfortunately, the actual slip length (few tens of nanometers) is much smaller than the mesh size in most numerical simulations, and the available computational resources do not allow the slip velocity to be accurately resolved (Lunkad et al., 2007; Renardy, Renardy, & Li, 2001). On the other hand, the VOF implementation uses the cell face normal velocity to advect the volume fraction, thus an implicit ("effective") slip length of one mesh size is included by default, even though the no-slip condition is enforced on the solid wall (Afkhami, Zaleski, & Bussmann, 2009). Consequently, the contact line velocity computed by the VOF methodology is mesh-dependent: a coarser mesh leads to a larger slip length and, therefore, a larger contact line velocity, and vice versa. However, it is seen from Eq.(2.6.6) to (2.6.10) that an increase in the contact line velocity results in a larger dynamic contact angle, and Afkhami et al. (Afkhami et al., 2009) showed larger contact angles allow the surface tension force to balance the stress singularity, thus slowing the moving contact line. As a result, the overall contact line motion becomes largely insensitive to the mesh spacing (Afkhami & Bussmann, 2009; Annapragada et al., 2011; Bussmann et al., 1999; Keshavarz-Motamed et al., 2010; Renardy et al., 2001). Following this observation, $u_{cl}\left(t\right)$ in the present work is taken as the normal velocity of the liquid-gas interface at one half-cell height above the solid wall. It is noted that an estimate of u_{cl} can be also calculated by numerically differentiating the interfacial contact radius: $u_{cl}\left(t\right)=\frac{dR}{dt}$ (Nichita, 2010; Sikalo et al., 2005). However, the result obtained from this approach is highly sensitive to the time step used. Hence, it was not used in the present work.

The friction coefficient, ζ, can be determined experimentally by fitting the measured DCA data with a certain DCA model. However, the value differs in the available reports. In general, it was found that a larger value (ζ = 0.2-0.4 Ns/m^2) fit the experimental data well when the contact angle hysteresis effect is not considered (Annapragada et al., 2011; Decamps & De Coninck, 2000; K. L. Wang & Jones, 2005), otherwise a smaller value ($\zeta = 0.18$ Ns/m^2) is more suitable (J. Hong et al., 2014; Jung Min Oh et al., 2010). In the simulations of this work, $\zeta = 0.15$ Ns/m^2 is used as it yields more accurate predictions of the experimental data.

The pinning force, c_{pin}, is deduced from the contact angle hysteresis (Jung Min Oh et al., 2010) as

$$c_{pin} \approx \sigma_{lv} \left| cos\theta_e - cos\theta_a \right| \text{ or} \tag{2.7.11}$$

$$c_{pin} \approx \sigma_{lv} \left| cos\theta_e - cos\theta_r \right|, \tag{2.7.12}$$

where θ_a and θ_r are the advancing and receding contact angles, respectively. The experimental results showed the maximum contact angle hysteresis ($\theta_a - \theta_r$) is about 16°. Hence, c_{pin} is set as 0.009 N/m in the simulations, which corresponds to $\left|\theta_a - \theta_e\right| = 8^\circ$.

2.4.4 Mesh Independence

Three different mesh sizes, 200 × 200, 267 × 267 and 400 × 400, were employed in this study, which correspond to 10, 13 and 20 grids per initial contact radius of the droplet, respectively.

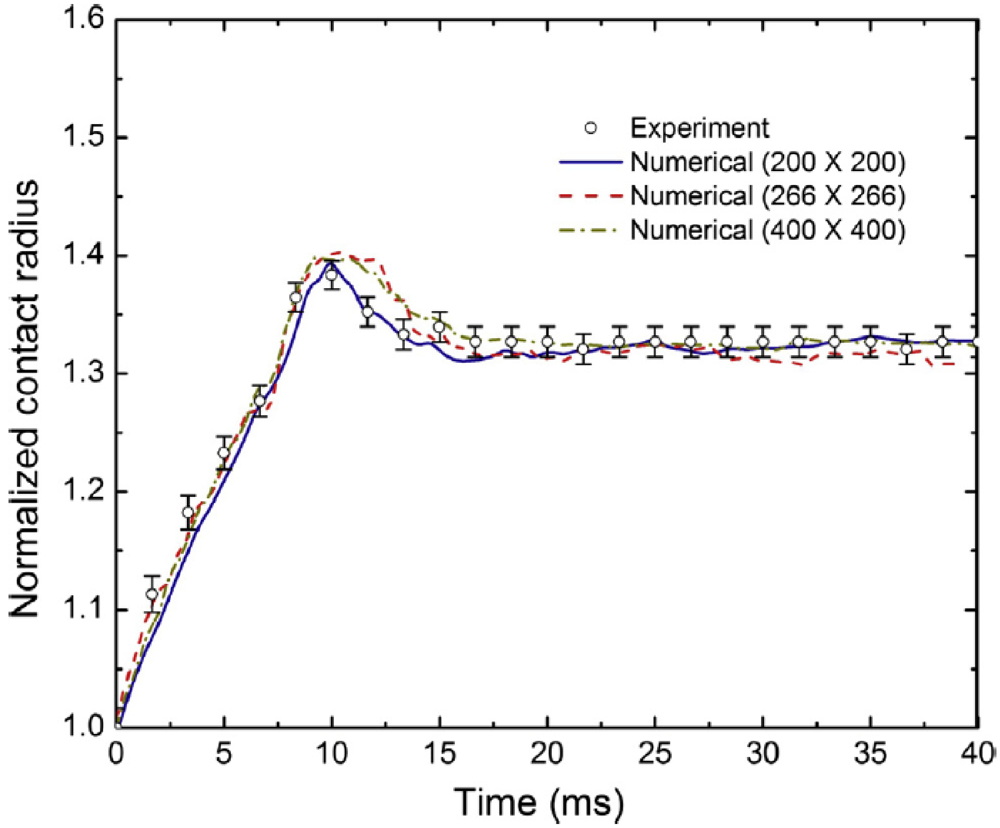

Figure 2.3. Comparison of the predicted time evolution of the normalized droplet contact radius vs. the experimental data for a step voltage (V=32 V)

Figure 2.3 illustrates the predicted time evolution of the contact radius of the droplet as compared to the experimental measurements (Note: the contact radius was normalized by the initial contact radius, R_0). The results show that the 200 × 200 mesh yields a satisfactory prediction of the measurements and further mesh refinement does not drastically improve the prediction accuracy. This is consistent with the findings in (Bussmann et al., 1999; Lunkad et al., 2007) that a resolution of 10 grids per drop radius is sufficient to capture the dynamics of the droplet motion. Hence, a mesh size of 200 × 200 was used in all the simulations of this work.

2.5 Results and Discussions

2.5.1 Droplet dynamics in DCEW

Figure 2.4 shows the comparison of the experimental results (left) with the VOF simulation predictions (right) of the instantaneous droplet shape at different time instants for a step input voltage (V = 32 V). It is observed that the droplet remains a spherical cap shape before the signal is applied (t = 0 ms). Once the voltage is turned on, the contact line moves outward. The shape of the droplet distorts as the electrical force reduces the contact angle from θ_e to the new equilibrium value θ_{app}.

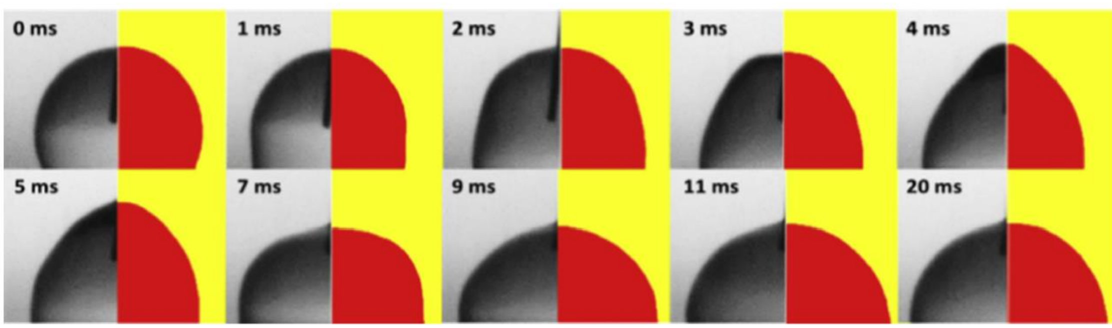

Figure 2.4. Comparison of the experimental results (left) with the predicted instantaneous droplet shape (right) for a step voltage (V = 32 V).

The detailed droplet dynamics can be visualized through the internal flow field within the droplet, as shown in Figure 2.5. Clearly, the droplet motion originates from the contact line at t = 0.1 ms. The high velocity region represents the commencement of capillary waves, and the rest of the fluid inside the droplet remains stationary. As time elapses, the capillary waves propagate upward along the liquid-gas interface, causing the impacted part of the droplet to deform continuously (t = 0.5 – 3.5 ms). At t = 4 ms, the wave fronts reach the apex and the focusing effect causes the droplet height to rise momentarily. Subsequently, the surface waves are reflected back to the bottom of the droplet, thereby lowering the height and further spreading the contact radius on the wall (t = 6 – 20 ms).

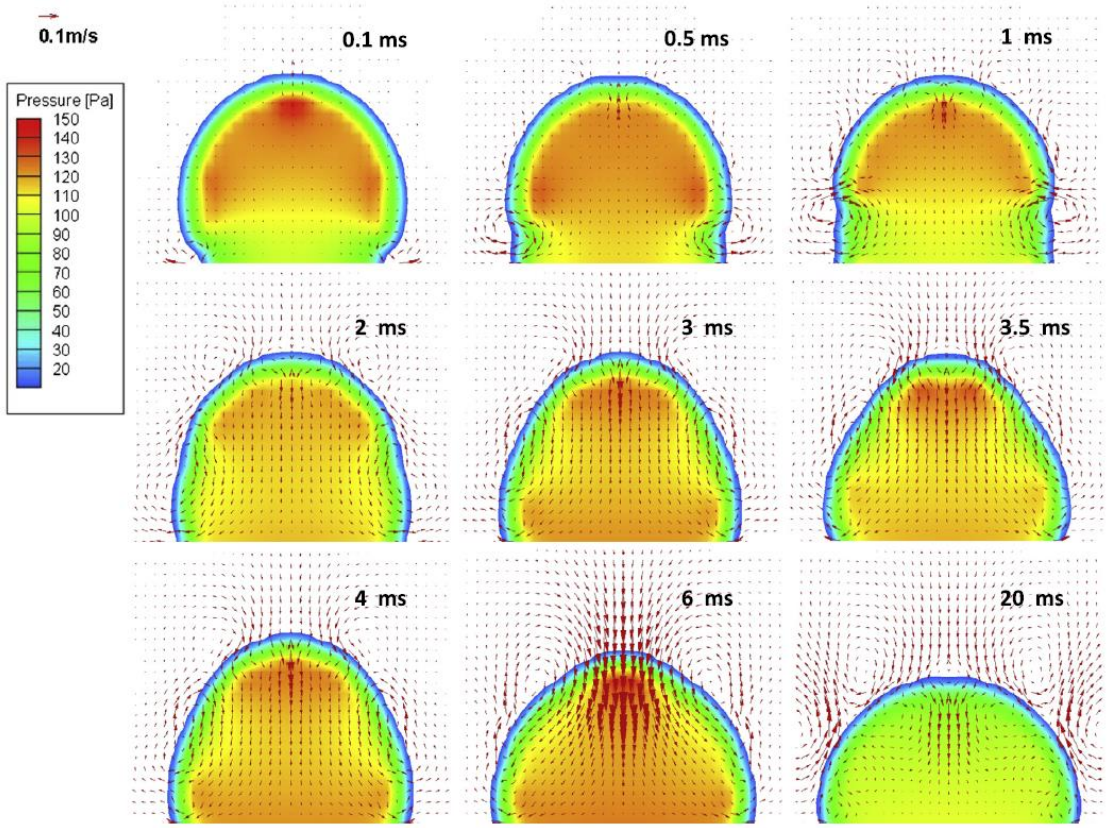

Figure 2.5. Internal flow field within the droplet for a step voltage (V = 32 V)

The time history of the normalized contact radius, normalized height and instantaneous contact angle of the droplet is plotted in Figure 2.6 for a pulse wave input (V = 32 V and the duty cycle T_0 = 500 ms). The height is normalized relative to the initial height of the droplet. The results show that the contact line first expands on the wall and, after reaching the maximum radius at t = 11 ms, it recoils and undergoes damped oscillations until a new equilibrium is established at t = 15~16 ms (The final normalized contact radius is about 1.35). The overshoot in contact radius is the consequence of the inertia of the internal flow induced by the contact line motion. After the voltage returns to zero (t = 500 ms), the contact line rapidly contracts to a minimum radius (t = 512 ms) before restoring to a final size, which is slightly larger than the initial radius due to the contact angle hysteresis effect. The time constants for the droplet expansion and contraction processes are found to be roughly the same, 15~16 ms. As compared to the short transient in contact radius, Figure 2.6 depicts a sustained oscillating behavior in the height evolution that barely reaches an equilibrium in the duration of the experiment. This can be attributed to the different damping mechanisms for the contact radius and the height (Annapragada et al., 2011): the motion of the contact line is dampened by the contact line friction, whereas the height becomes stabilized only after the inner flow is completely subdued by the much slower viscous dissipation. Another observation in Figure 2.6 is that the contact angle is out of phase with the height during the oscillation, i.e., an increasing contact angle is always accompanied by a decrease in the height of the droplet, as required by the constant volume constraint.

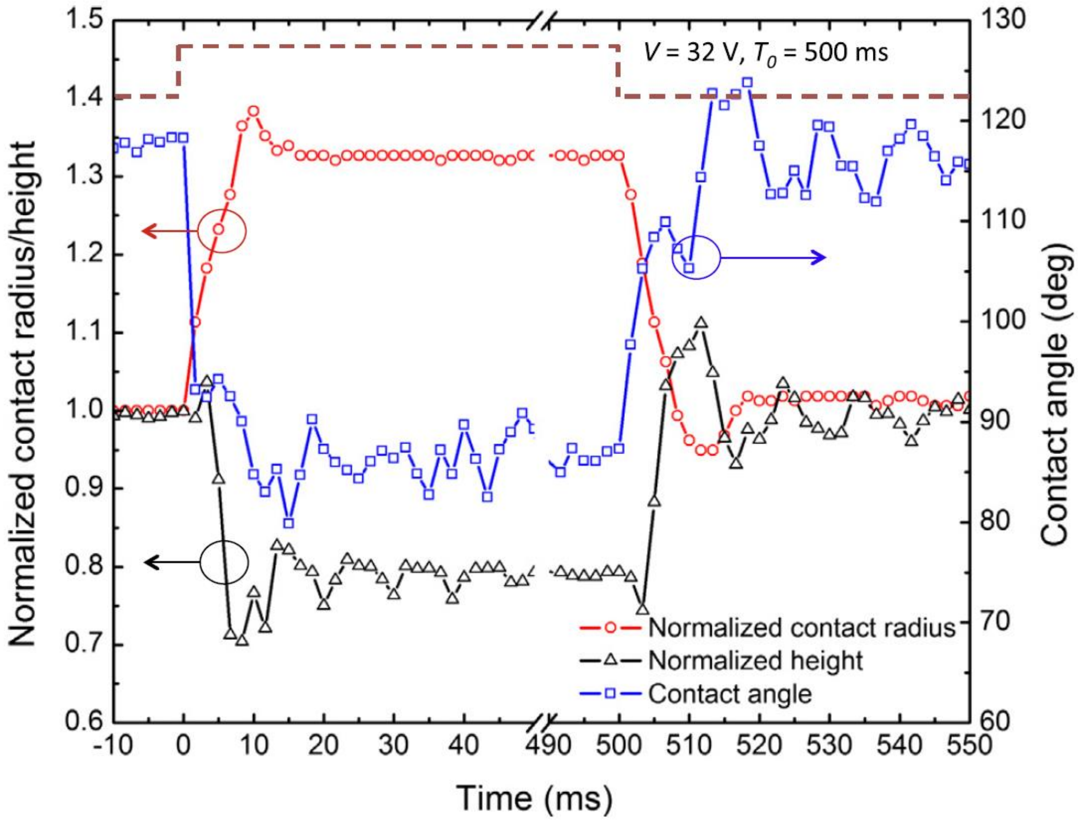

Figure 2.6. Time history of the normalized contact radius, normalized height and contact angle of the droplet for a pulse wave voltage (V = 32 V and T_0 = 500 ms)

2.5.2 Droplet dynamics in ACEW

Shape oscillations of the droplet in ACEW were investigated with sinusoidal input voltages of 32 V_{RMS}. The frequency of the actuating signal, *f*, varies from 0 to 200 Hz.

Figure 2.7 compares the simulation predictions (left) with the experimental results (right) of the instantaneous droplet shape at different time instants for three different actuating frequencies, f_E= 27 Hz, 79 Hz and 150 Hz, respectively. Resonance oscillations of the interface can be observed clearly from the images. It is interesting to note that the oscillating frequencies of the droplet (f_{exp}) are 50 Hz, 156 Hz and 278 Hz, about twice the corresponding signal frequencies. This is because the droplet oscillation originates from the cyclic motion of the contact line, which is driven by the electrical force that is proportional to the square of the input voltage (as indicated by Eq. (2.6.7)). The resonance frequency of a free, inviscid droplet, f_n, is given by (Lamb, 1932)

$$f_n = \frac{1}{2\pi}\left[n(n-1)(n+2)\frac{\sigma_{lv}}{\rho_l L^3}\right]^{1/2}, \tag{2.8.1}$$

here ρ_l is the liquid density, L is the volume-average radius of the droplet, and n is an integer corresponding to different oscillation modes (n = 1, 2, …).

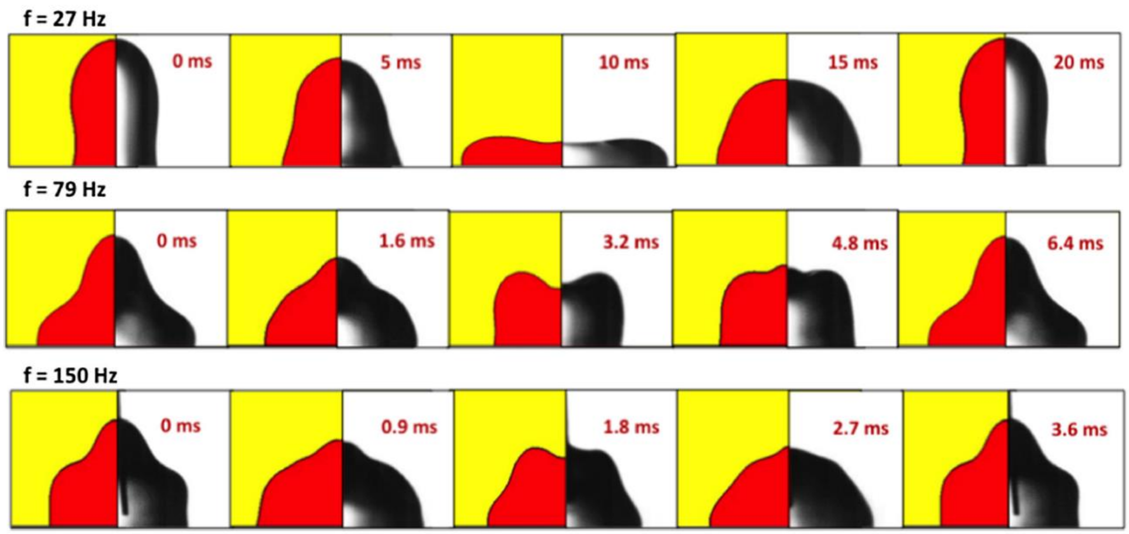

Figure 2.7. Comparison of the predicted instantaneous shape oscillations of the droplet (left) with experiments (right) during one oscillation cycle at 36 VRMS

Table 2.1 enumerates the actuating frequency, f, the measured oscillating frequency, f_{exp}, and the resonance frequency, f_n, of a 9 μL droplet. It is seen f_{exp} deviates from f_n by 10-13%, and this can be attributed to the viscous damping due to the presence of a moving contact line and the viscous boundary layer at the droplet-substrate interface. Hence, the droplet is oscillating at (or near) its resonance frequencies, and the shape patterns in Figure 2.7 correspond to three resonance modes, P_2, P_4 and P_6, respectively.

Table 2.1. Comparison of the actuating frequency, the oscillating frequency and the resonant frequency of the droplet.

Mode	Actuating frequency, f (Hz)	Oscillating frequency, f_{exp} (Hz)	Resonant frequency, f_n (Hz)
P_2	27	50	58
P_4	79	156	174
P_6	150	300	318

The shape modes of the droplet oscillations are better resolved in Figure 2.8. Each image is the superimposition of over 100 images recorded by the high-speed camera during at least one oscillation cycle. The black arrows denote the node points where the local displacement of the free surface is always zero. It is observed that, as the mode number increases, the number of nodes and lobes also increases, whereas the oscillation amplitude (i.e., the lobe size) becomes smaller. For instance, P_2 mode occurs at f = 27 Hz and is characterized by the oblate and prolate spheroidal shapes with two nodes and three lobes. Similarly, the P_4 mode takes place at 79 Hz with four nodes and five lobes, and the P_6 mode at 150 Hz with six nodes and seven lobes. In the experiments, it is possible to identify other higher-order shape modes, such as P_8 and P_{10}, etc. However, the size of the lobes decreases drastically with increasing mode numbers, making them difficult to distinguish.

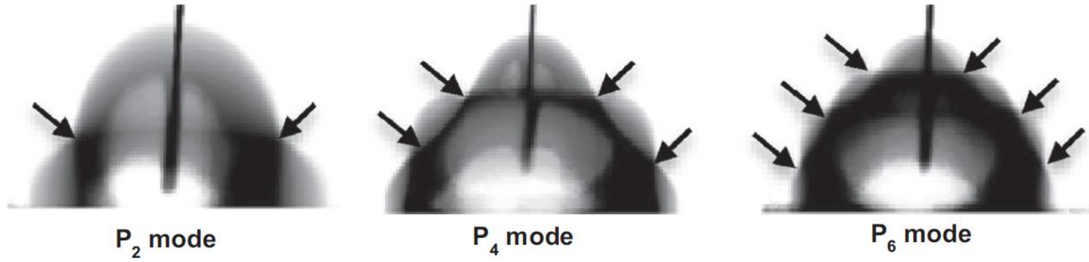

Figure 2.8. Resonance modes of shape oscillations of the droplet

Figure 2.9 shows the oscillation amplitudes (represented by the maximum normalized contact radius and height) as a function of the actuating frequency *f*. It is observed that the oscillation almost vanishes at high frequencies ($f \rightarrow 200$ Hz). Local maxima of descending amplitudes can be found at three Eigen-frequencies, $f = 27$ Hz, 79 Hz and 150 Hz, respectively. This observation can be explained as follows. In EW, four resistive forces, including the inertia (F_i), the viscous force (F_v), the capillary force (F_c) and the contact line friction force (F_{cl}), act against the droplet deformation induced by the electrical force (F_{EW}). Using $\mathcal{L} = 2R_0$, $T = 1/2\pi f_n$ and $u = R_0/T$ as the characteristic scales of length, time and velocity, these forces (per length) can be estimated as $F_i \sim \rho_l u^2 L$, $F_v \sim \mu_l u$, $F_c \sim \sigma_{lv}$ and $F_{cl} \sim \varsigma u$. The frequency-dependence of all five forces is plotted in Fig. 2.10.

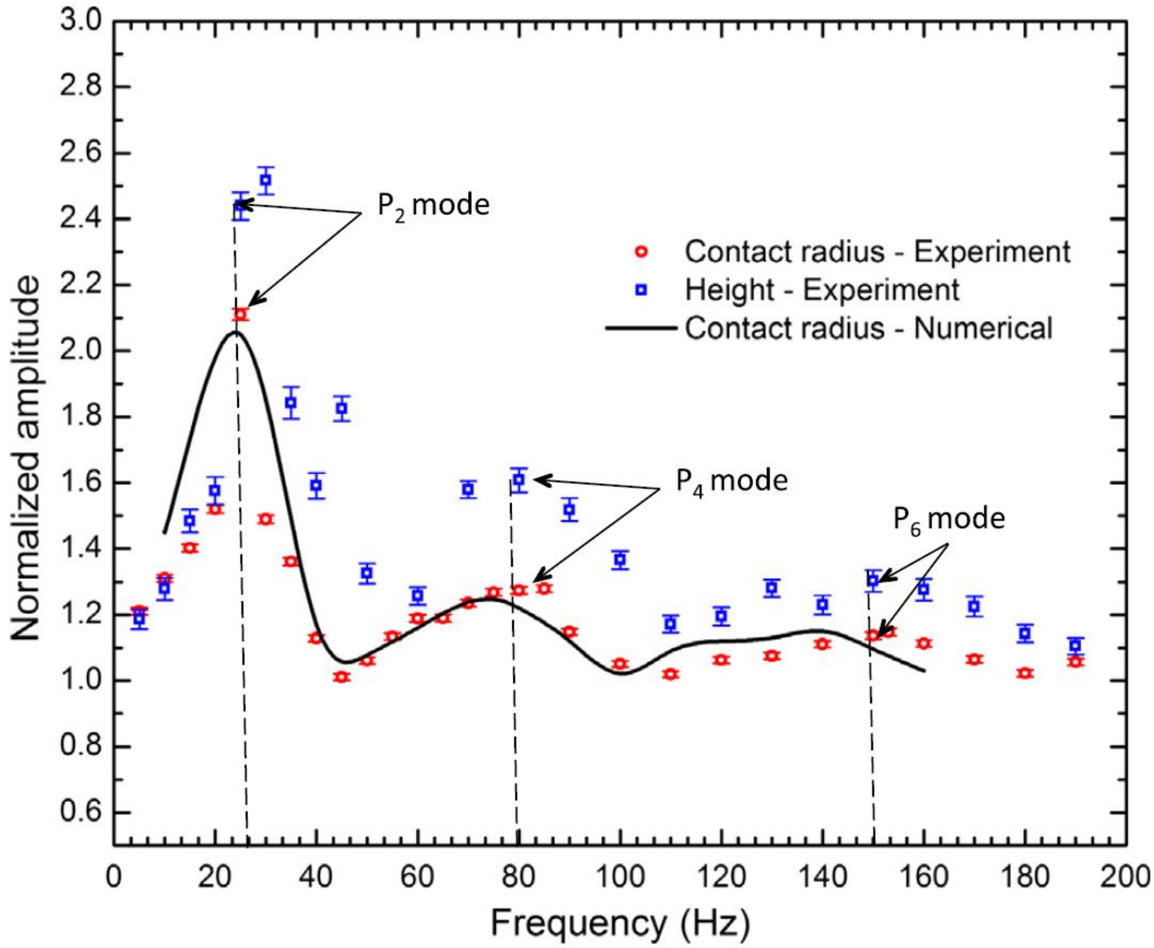

Figure 2.9. Oscillation amplitudes as a function of actuating frequency.

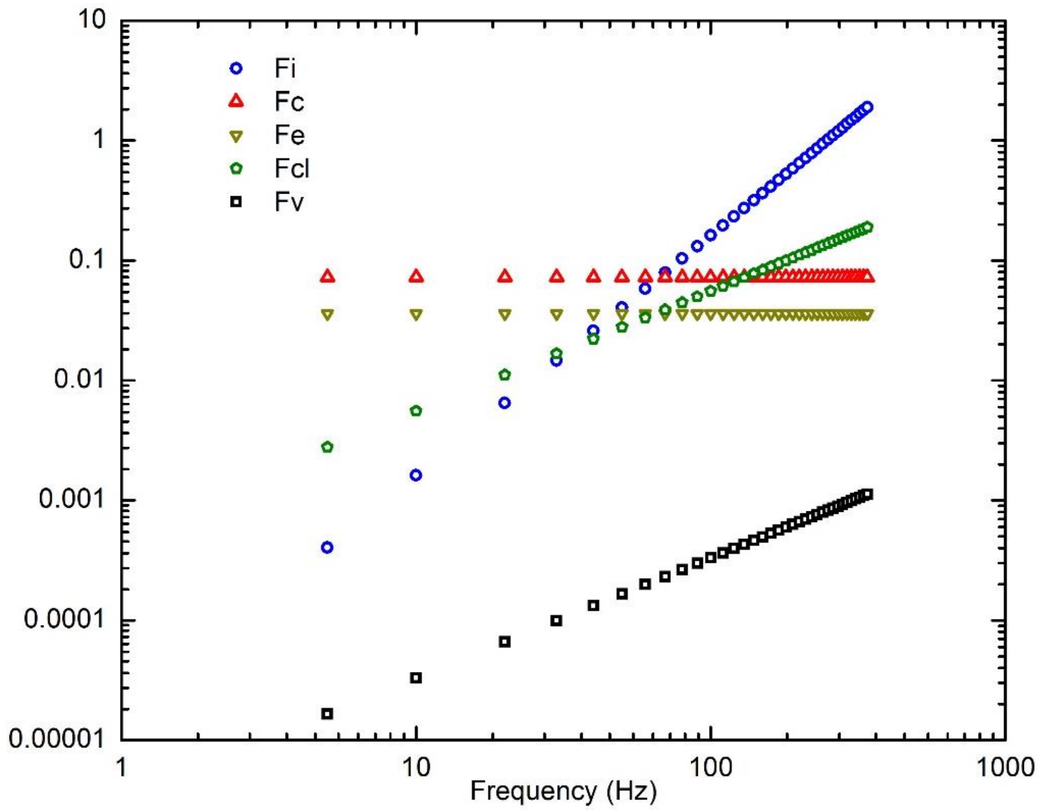

Figure 2.10. Comparison of the electrical force, inertia, capillary force, contact line friction force and viscous force.

It shows that, while the capillary force remains comparable to the electrical force, the inertia and the contact line friction become dominant as the frequency increases. At sufficiently high frequencies, they will prevent the droplet from following the external excitation. As a result, the droplet shape becomes essentially quasi-stationary, i.e., the oscillation will terminate. It is also noted that viscous dissipation is nearly negligible in ACEW due to the small magnitude of the viscous force.

Figure 2.11 depicts the details of the droplet oscillations in terms of the normalized contact radius, normalized height and contact angle at three resonance frequencies, f = 27 Hz, 79 Hz and 150 Hz. The symbols are data obtained from the experiments and the lines are sinusoidal fit. At all three frequencies, the instants of the maximum contact angle always correspond to the minimum contact radius. Thus, these two parameters are out of phase with a constant phase angle of 90°. In contrast, the phase relation between the drop height and the contact radius seems to be frequency-dependent. For instance, they are out of phase at 27 Hz and 150 Hz but in phase at 79 Hz. Furthermore, it is surprising to note that the droplet oscillations closely follow the sinusoidal waveform of the input signals at all three frequencies, although, according to the DCEW results in Figure 2.9, the droplet can respond fully to a step stimulus of frequency up to 67 Hz (with a corresponding actuating frequency f_E = 33 Hz) as it has a time constant of ~ 15 ms. In fact, both observations for DCEW and ACEW suggest the EW-actuated droplet system mimics a second-order dynamic system, such as a driven harmonic oscillator with viscous damping, which follows a parametric equation (Ogata, 2003)

$$\frac{d^2x}{dt^2} + 2\zeta\omega_n \frac{dx}{dt} + \omega_n^2 x = \frac{F(t)}{m}, \tag{2.8.2}$$

where x is the measure of the oscillation, ω_n is the resonant angular frequency, ζ is the damping ratio, m is the effective mass of the system, and $F(t)$ is the external driving force. Interestingly, a few phenomenological models with governing equations of a similar form to Eq. (2.8.2) have been developed to describe the droplet motion ((Annapragada et al., 2011) (Dash, Kumari, & Garimella, 2012) (Baret, Decré, & Mugele, 2007; Sen & Kim, 2009)). While it remains elusive if the EW-actuated droplet system complies rigorously with Eq. (2.8.2), the results in Figures 2.9 and 2.11 indicate that methodologies from the discipline of dynamic systems may prove very useful in understanding the nonlinear oscillating behavior of electrowetting systems in the future work.

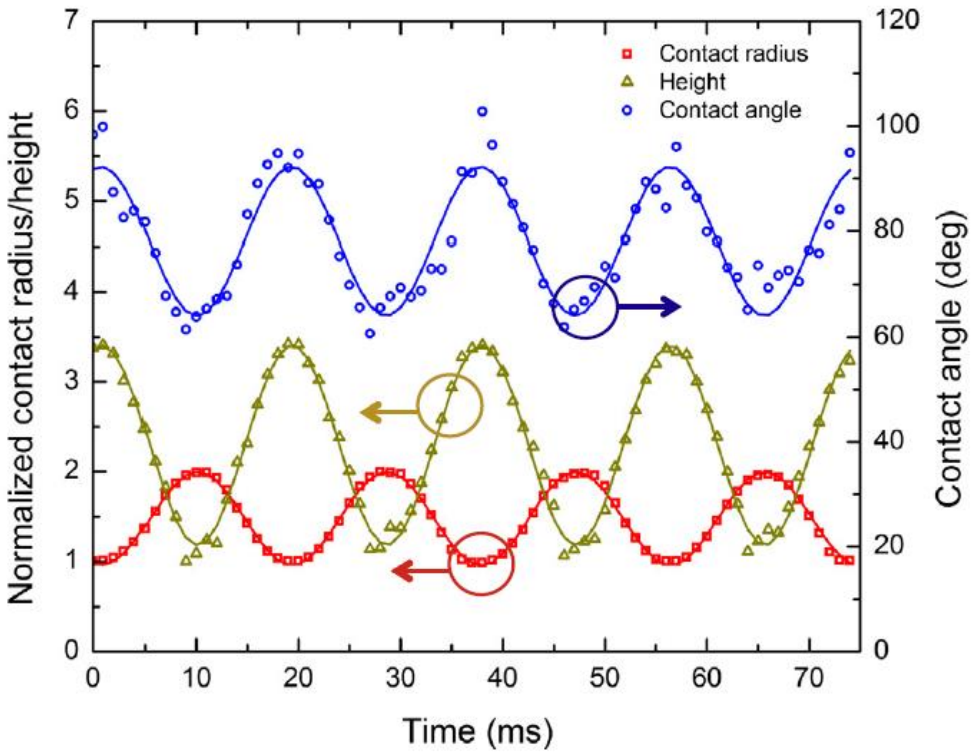

Contact radius
Height
Contact angle
Normalized contact radius/height
Contact angle (deg)
Time (ms)

(a)

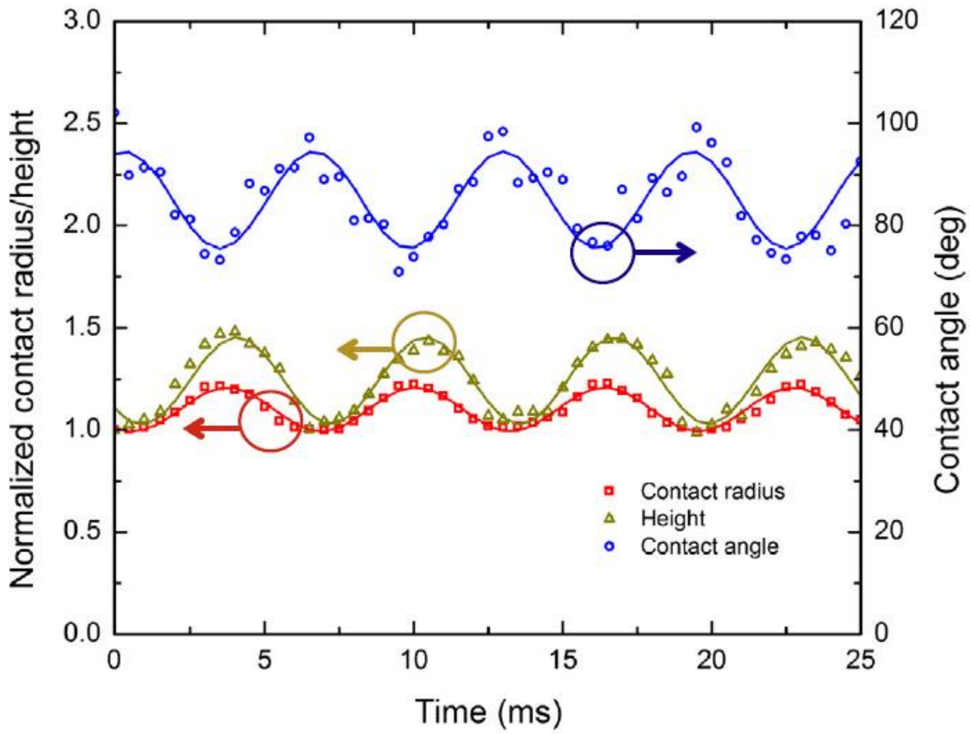

Contact radius
Height
Contact angle
Normalized contact radius/height
Contact angle (deg)
Time (ms)

(b)

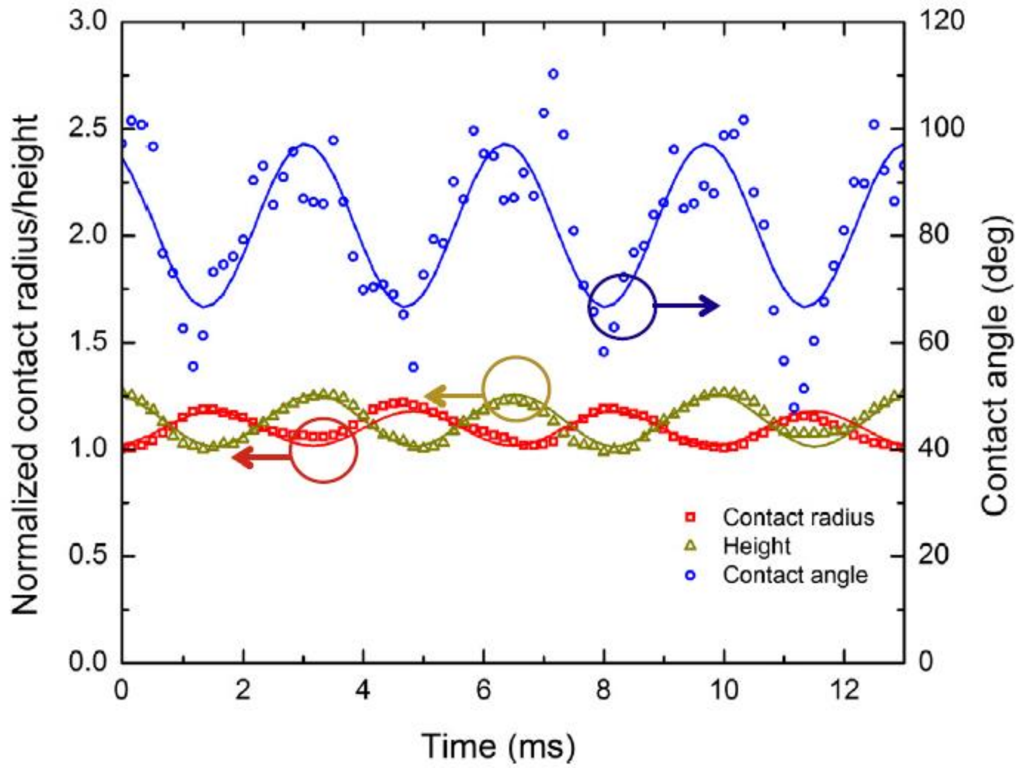

(c)

Figure 2.11. Droplet oscillation at resonance frequencies: (a) f = 27 Hz, (b) f = 79 Hz and (c) f = 150 Hz.

Figure 2.12 illustrates the velocity vector field and the pressure distribution inside and around the droplet obtained from the VOF-CSF simulations. The results correspond to three representative time instants in the P_2, P_4 and P_6 oscillation modes (Note: 1) the initial time instant, $t = 0$ ms, was chosen somewhat arbitrarily, and 2) the images shown were for the descending half-cycle of the droplet movement). It is interesting to notice that the velocity vector field is in very good agreement with the numerical results obtained in (Ashoke Raman et al., 2016; Z. Li et al., 2012). Furthermore, recirculation swirls can be identified from the streamline contours, and the number of vortices matches the respective resonance modes. For instance, two vortices can be observed for the P_2 mode, four for P_4 mode and six for P_6 mode. The centers of the vortices are located either at or close to the free surface, which correspond approximately to the nodal points marked in Fig. 2.8. It is also noticed that, due to the decaying oscillation amplitudes of the droplet, the size of the vortices decreases significantly from the P_2 mode to P_6 mode.

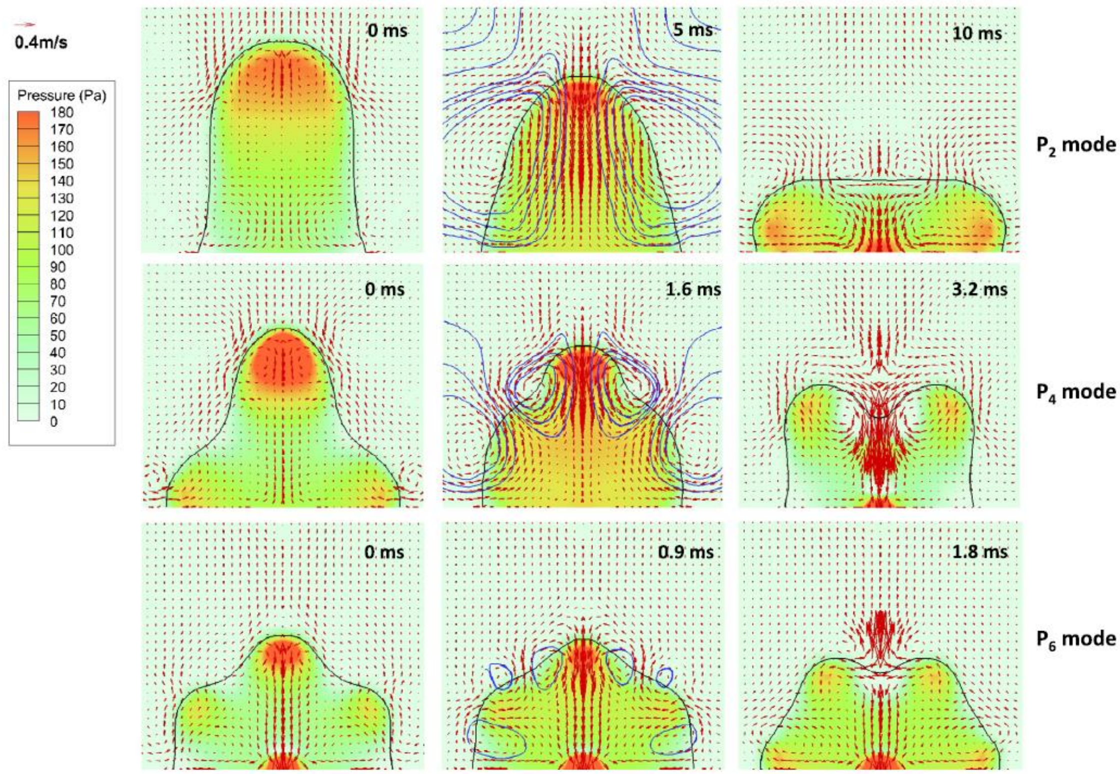

Figure 2.12. Velocity vector field, pressure distribution and vortex zone inside and around the droplet at resonance modes (Note: Pressure is relative to the ambient).

As discussed for the case of DCEW, the droplet motion originates from the moving contact line and the perturbation subsequently spreads along the interface toward the apex of the droplet. In ACEW, propagating surface waves are generated due to the cyclic forcing mechanism at the contact line. By setting the origin at the center of the droplet, Figure 2.13 depicts the instantaneous interfacial shape extracted from the numerical data (Figures 2.7 and 2.12). It is seen that t = 0 ms marks the moment at which the wave fronts meet at the apex ($\phi = 90°$) and the droplet height reaches the maximum due to the geometric focusing effect. Consequently, the waves are reflected back towards the contact line ($\phi = 0°$) without much damping of the oscillation amplitudes. The nodal points for the P_2, P_4 and P_6 modes can be identified in Figures. 2.13 (b)-(d) as the intersection points of the oscillation curves. A standing-wave type of behavior is also observed. Taking the P_6 mode as an example, it can be deduced from Figures. 2.5.13 (a) and (d) that the radius connecting the nodal point and the origin is $r_0 \sim 1.6\,mm$, and the central angle between two adjacent nodal points is $\phi_0 \sim 32°$. Thus, the wavelength of the surface waves can be estimated as the arc length, $\lambda_s \sim 2 r_0 \phi_0 = 1.79\,mm$. Since the P_6 mode corresponds to f_n = 318 Hz, the propagation speed of the waves can be calculated as $u_p = f_n\ \lambda_s = 0.57\,m/s$, which agrees well with the phase velocity for capillary waves (J. M. Oh, Legendre, & Mugele, 2012).

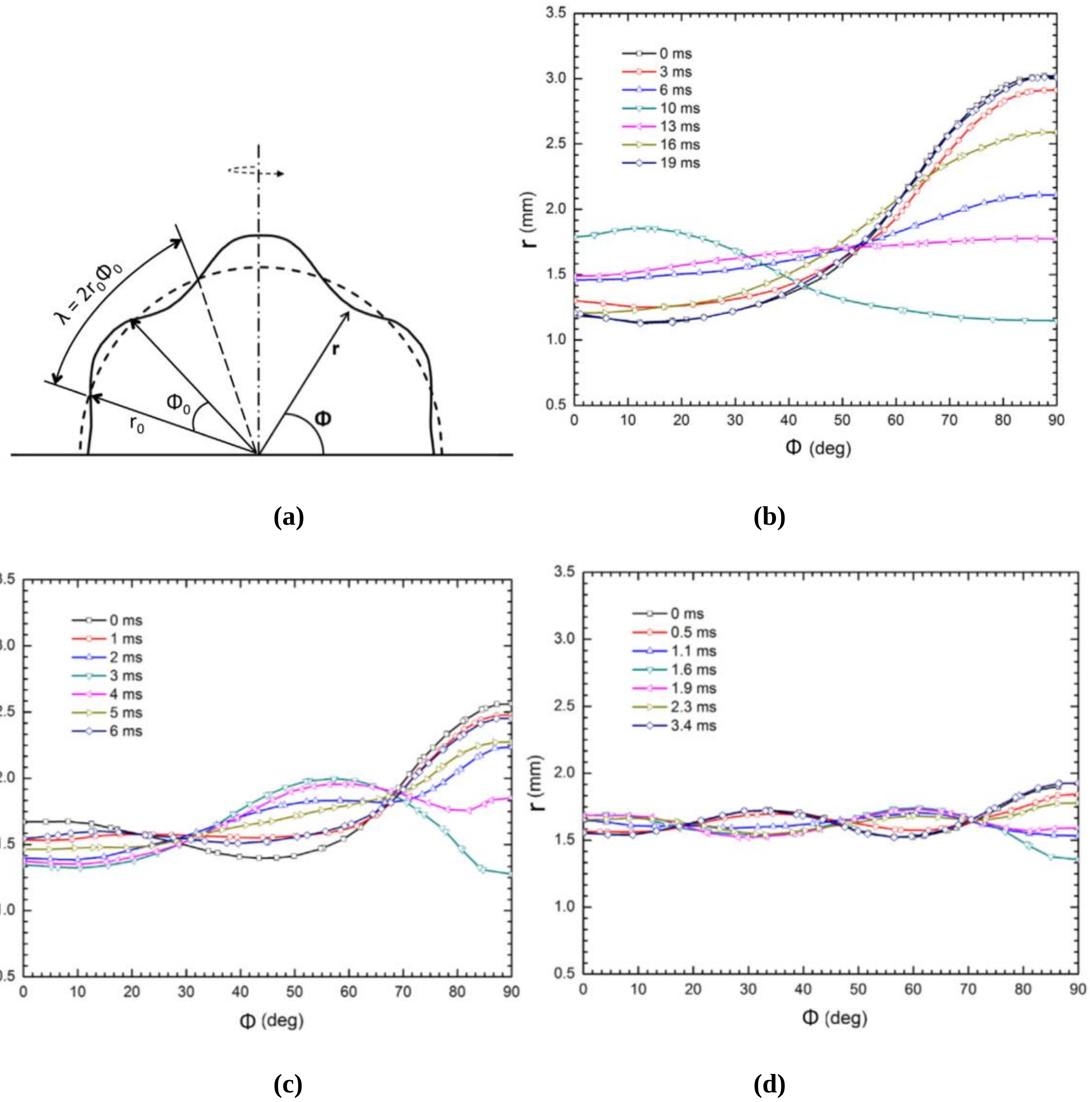

Figure 2.13. Instantaneous interfacial shapes of the droplet. (a) Schematic of the oscillating droplet, (b) P2 mode (f = 27 Hz), (c) P4 mode (f = 79 Hz), and (d) P6 mode (f = 150 Hz)

2.6 Summary

A combined numerical and experimental approach was applied to explore the dynamics of EW-induced droplet motion. The time history of the contact radius, height and instantaneous contact angle of the droplet was investigated for a step input DC signal.

The resonance oscillations of the droplet at different actuating frequencies were studied for sinusoidal AC signals. The VOF-CSF method was used to develop CFD models that incorporate an MKT-based dynamic contact angle model. Numerical predictions of various parameters of EW-induced droplet dynamics were validated with the experimental measurements obtained from high-speed photography. This work will help to advance the fundamental understanding of droplet dynamics involved in various EW-based systems, especially in the fledging field of digitized active cooling for high-heat-flux thermal management of microsystems.

The key findings can be summarized as follows:

1) A proper selection of the dynamic contact angle model is essential to numerical analysis of droplet dynamics. In this regard, an MKT-based model that considers the contact line friction and the pinning force at the moving contact line was successfully implemented. Special attentions were paid to the acquisition of the contact line velocity and the pinning force, whereas a fitting value was selected for the friction coefficient.

2) The response time of a droplet to external excitations can be characterized from the droplet's expansion and contraction processes under DCEW.

3) When actuated at resonance frequencies in ACEW, the droplet exhibits time-harmonic shape oscillations. The oscillation amplitude is found to decrease with increasing actuating frequency, due to the dominant effect of inertia over other forces. The surface wave propagates with a similar phase velocity for capillary waves.

4) Overall, the dynamics of EW-actuated droplet motion mimics that of a second-order dynamic system.

Chapter 3 Suppression of Leidenfrost State of a Drop by EW

3.1 Literature Review

Boiling heat transfer phenomenon was brought out by researchers for its advantages in high heat transfer coefficient and heat dissipation capacity during phase change. A great amount of energy could be potentially dissipated in the form of liquid evaporation. However, due to fast accumulation of evaporated vapor near heater surface and relatively low thermal conductivity of vapor, heat removal from the heating surface was hugely impacted. When heating up a substrate surface above a threshold temperature, liquid could be lifted up due to the formation of a stable vapor cushion between liquid bottom surface and substrate. This temperature limit usually refers to Leidenfrost point (LFP). It was named after a German physician (JG, 1756) to emphasize the contribution of his finding on this phenomenon. For most circumstances, Leidenfrost effect was attempted to be avoided for its undesirable consequences in industrial applications such as spray cooling (Wendelstorf, Spitzer, & Wendelstorf, 2008) and areas requiring fast heat exchange like nucleate reactors (Berthoud, 2000; Mochizuki, Singh, Nguyen, & Nguyen, 2014). In order to improve LFP, method or technology associated with this subject has been gained great attention.

The mechanisms that affect LFP were attempted to be unveiled and explained in order to effectively enlarge the regime of nucleate boiling. In retrospect, previous efforts were mainly dedicated from two perspective to improve LFP. First, from surface modification, passively suppressing Leidenfrost effect has achieved significant performance. For example, capillary wicking (S. H. Kim, Ahn, Kim, Kaviany, & Kim,

2013) was found to effectively improve surface energy according to Wenzel's effect (Yoshimitsu, Nakajima, Watanabe, & Hashimoto, 2002). Also increased surface wettability could defer the advent of vapor layer formation. What's more, influence according to surface modifications involved in changing the surface roughness or creating textures or ratchet (Dupeux, Bourrianne, Magdelaine, Clanet, & Quere, 2014). The impact of surface micro-structures (H. S. Ahn, Sathyamurthi, & Banerjee, 2009; Kwon, Bird, & Varanasi, 2013; Tran et al., 2013), porosity and surface wettability were also reported respectively and relatively in recent literatures (Bernardin & Mudawar, 1999; H. Kim, Truong, Buongiorno, & Hu, 2011). However, the complex micro-fabrication process and interaction of various surface factors (Adera, Raj, Enright, & Wang, 2013) usually compromised to achieve a very high LFP. Instead, surface modification was more frequently applied in areas where non-wetting surface was required (Vakarelski et al., 2012) . On the other hand, introducing external stimulus such as electric (Celestini & Kirstetter, 2012; Shahriari, Wurz, & Bahadur, 2014) and magnetic actuation (Piroird, Clanet, & Quere, 2012) or mechanical vibrations (Ng, Hung, & Tan, 2015, 2016) was reported more frequently and more effectively change Leidenfrost state. Those external fields were aimed at actively controlling and dynamically altering liquid-and-vapor motion and interfacial hydrodynamic conditions. A stable vapor film was supported by viscous pressure. It is due to fast vapor horizontal flows by droplet evaporation. As the vapor layer is very thin compared with contact radius, a proper simplification of Navier-Stokes equation could evaluate the viscous pressure according to lubrication theory (Biance, Clanet, & Quere, 2003)

$$\frac{dp}{dr} = \mu_v \frac{d^2u}{dz^2}, \tag{3.1.1}$$

where μ_v is viscosity of water vapor. The vapor layer serves as a one-way channel for evaporating vapor to escape. In the meantime, it creates an upward viscous stress to support the liquid's gravity. Experiments were attempted to dynamically interrupt Leidenfrost state, such that by injecting water jet into suspended liquid (Ahmed & Hamed, 2015). Those efforts were aimed at exerting a direct dynamic stress to overcome the vapor pressure. With a high impinging speed or strong interfacial oscillation, A large velocity was accounted for the liquid quenching and LFP improvement (Tran, Staat, Prosperetti, Sun, & Lohse, 2012). On the other hand, liquid rewetting was also explained and stressed from hydrodynamic perspective (Ahmed & Hamed, 2015; Johnson, 1968). It aimed at destabilizing the interface by promoting interfacial wave growth (Tanaka, 1988). Instability took place under disturbance with wavelength greater than critical wavelength

$$\lambda_c = 2\pi[\frac{\sigma}{(\rho_l - \rho_v)g}]^{0.5}. \tag{3.1.2}$$

Recently, it has come to the attention that electrowetting (EW) can help to improve boiling heat transfer and achieving a higher CHF and Leidenfrost values (Shahriari, Hermes, & Bahadur, 2016a) (Aritra & al, 2016). EW (Y. Lu et al., 2017) was known as a versatile tool to actively control micro fluid flows and capable of tuning the surface wettability et al. Those features seem to be in favor of maintaining a wetting surface and avoiding the dry-out. However, the physical explanation behind the scene were still to be illuminated.

3.2 Experimental setup

In this work, Leidenfrost suppression by EW was studied through a micro-liter sized droplet on a hot plate. The experimental setup for Leidenfrost drop were schematically shown in Figure 3.1 (a) and the forces and configuration of electric circuit were also shown in Figure 3.1 (b). For a microliter-sized drop which is smaller than capillary number ($c = \sqrt{\sigma_{lv}/\Delta\rho g}$) , a hemi-spherical geometry was rendered for most part of the testing drop except flattened in the bottom (Y. Lu et al., 2017).The test piece was a 3” silicon wafer (Silicon Quest, LLC) which was covered by a naturally grown silicon dioxide (100 nm). On this thermally grown (SiO2) layer ($\varepsilon_r = 3.9$), a thin layer (70 nm) of Teflon (AF2400, Dupont) was spin-coated on the wafer to produce hydrophobicity.

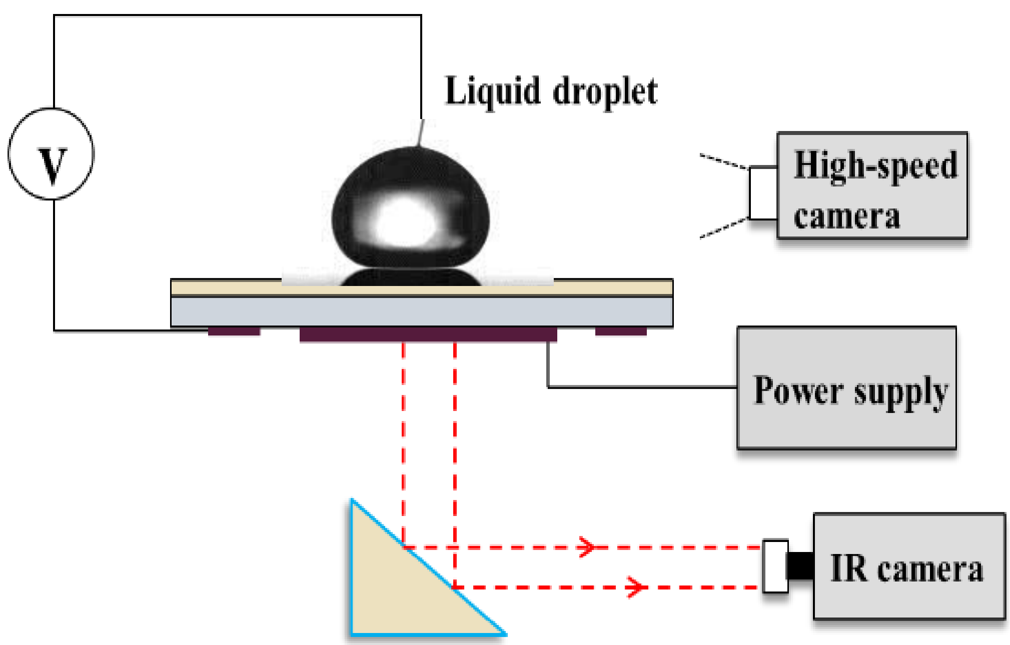

(a)

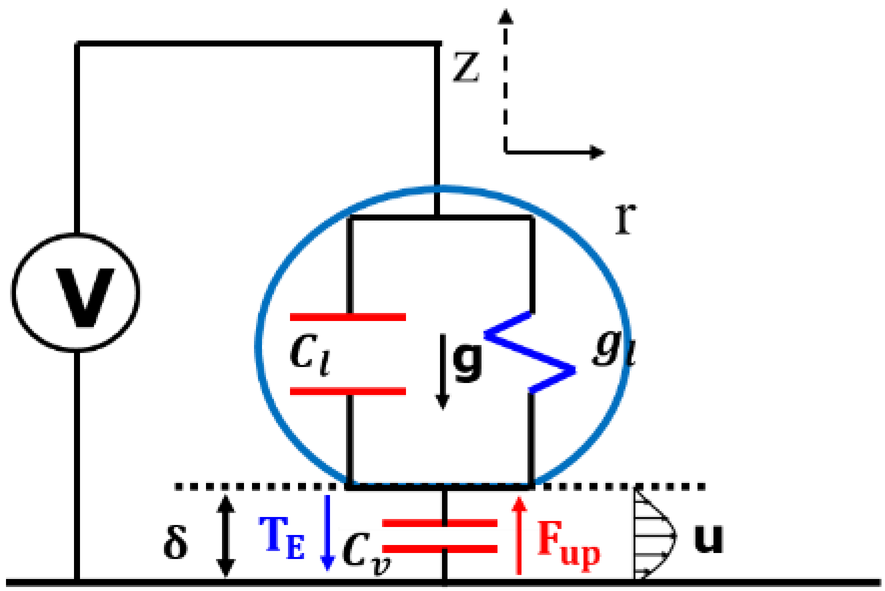

(b)

Figure 3.1. (a)Schematic plot of Leidenfrost setup on a Leidenfrost droplet. (b) Forces and electric circuit

To improve the adhesion of Teflon to SiO_2, a silane-based adhesion promoter (FSM-660-4, Cytonix) was dip-coated on SiO_2 before the Teflon spin-coating step for the purpose of avoiding surface burning and hydrophobic layer peeling-off. Since silicon has a reasonable electrical conductivity, the substrate serves as the ground electrode for EW. Micro-liter sized deionized water droplet was used for experiment and calculations. It was gently dispensed onto the test piece with a micropipette under the EW needle. The droplet was taken as finite conductive with a conductivity of 1 µs/m. A 99.99% pure platinum wire of a 100-µm diameter was inserted into the droplet from the top as the actuation electrode and helped with restricting the droplet's lateral motion. The images of droplet dynamic motion targeted on the zoom-in region of bottom interface were captured by high speed camera (FASTCAM Ultima APX Photon) with 6000 frames per second. The resolution of high speed is adjustable in the range of 17.1 μm to 33.5 μm per pixel size according to the distance away from the object. The IR camera was customarily calibrated and used to measure the temperature profile and heat flux contour on the back of substrate with the aid of reflective mirror.

3.3 Results and discussion

3.3.1 Forces and stresses at bottom interface

The state of film boiling on a hydrophobic surface and contact boiling suppressed under EW were respectively shown in Figure 3.2a. The experimental results showing in Figure 3.2b depicts the dependence of droplet evaporation time verses surface superheat. The duration of a microliter-sized (20 μl) droplet staying on the heating surface reflected the rate of energy dissipation. Temperature of the heating surface was gradually increased from 100 ℃ to 400 ℃. The measurement was conducted after the surface temperature became stable by increasing every 10 degree Celsius. To evaluate the evaporation time, we counted the process when first putting a micropipette quantified droplet underneath the needle until a small quantity of residue droplet was hanging on the needle and detached from the surface.

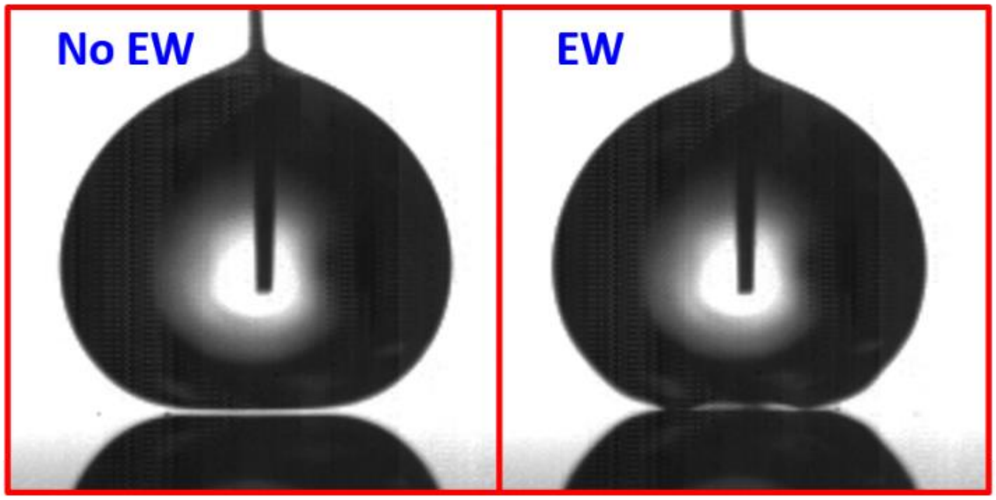

(a)

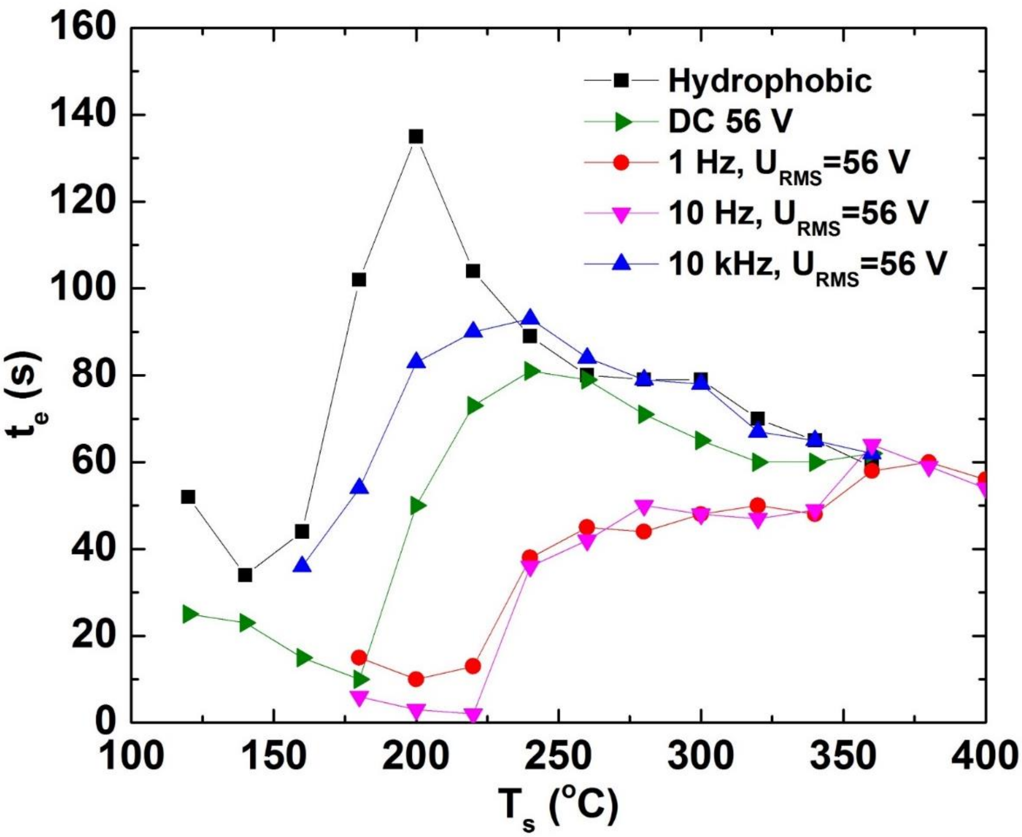

(b)

Figure 3.2. (a) Leidenfrost droplet with and without EW suppression. (b) Evaporation time of water droplet in a wide range of surface temperature with or without EW signals. AC sinusoidal signals were used at 56 V(RMS).

The testing piece experienced over three regimes of boiling under different surface temperatures: nucleate boiling, transitional boiling and film boiling. For a small quantity of liquid drop, energy is mainly dissipated in the form of latent heat due to liquid-vapor phase change. At nucleate boiling regime, heterogeneous bubbles were observed to form and grow inside the droplet from wall nucleation sites. Liquid conduction was rendered to be a major heat transfer scheme in the thermal boundary layer, the thickness (δ_t) of which is dependent on incipient boiling temperature (Hsu, 1962) and was estimated to be a few tens of microns. When temperature went high and got close to Leidenfrost point (LFP), the droplet was completely lifted up by a vapor cushion. Instead of liquid conduction, heat was transferred through vapor layer in this scenario. The radiation is a minor factor (Quere, 2013) considering for a relatively low surface temperature. Its contribution was negligible compared to heat transfer by conduction. The energy taken from the hovering liquid evaporation was only through the heat conduction and thus was expressed as (Gottfried, Lee, & Bell, 1966)

$$\frac{dm}{dt} = \frac{k_v}{h_{lv}} \frac{\Delta T}{\delta} A, \tag{3.3.1}$$

where h_{lv} is the latent heat of water. m is the droplet mass. ΔT ($T_w - T_{sat}$) is the temperature difference between wall and the water saturation temperature. δ is the thickness of vapor. k_v is water vapor conductivity. A is the contacting area of water on the heating surface which was calculated based on a non-dimensional scaling between gravity and surface tension (Mahadevan & Pomeau, 1999). The radius of contact was thus estimated by $r_0 = R^2/c$, where R and c are droplet radius and capillary number respectively. If δ_t and k_l were used to evaluate droplet evaporation at nucleate boiling regime through Eq. (3.3.1). The difference of thermal conductivity between liquid and vapor lead to a various difference of heat transfer rate. From the experimental data, EW had certainly extended the nucleate boiling regime, but the effect of electrowetting on CHF values was beyond the emphasis of this chapter. At transitional boiling stage (the region between film boiling and nucleate boiling), the droplet was observed intermittently contacting with the surface. Heat transfer rate was affected by continuous strike from droplet bottom interface and the substrate. The heat flux and droplet evaporation rate are based on the occupation fraction of liquid and vapor with the surface (Dhir & Liaw, 1989). The voltage dependence of Leidenfrost point was reported (Celestini & Kirstetter, 2012; Shahriari et al., 2014), but more interested things was showing that it is also relied on applied frequency difference. According to the modulation of frequency at a same given root mean square voltage, the evaporation time was different showing in Fig. 3.3.1 and it seems that a minimum frequency was required at each wall temperature for transition from film boiling back to contact boiling. Intuitively, the re-contact may be rendered to the attraction exerted by EW to overcome the supporting pressure. For a microliter sized droplet, the determination of vapor layer thickness mainly depends on the weight of the drop, electric force and surface superheat. Thus, the thickness of vapor layer may be evaluated from force balance perspective. To evaluate the viscous pressure, we equated the rate of evaporation from bottom surface with the mass flow rate through horizontal vapor passage (Biance et al., 2003; Wachters & Westerli.Na, 1966)

$$\pi r^2 v_{z=\delta} = \int_0^\delta 2\pi r u dz, \tag{3.3.2}$$

where $v_{z=\delta}$ is evaluated by mass loss of droplet through conduction which was obtained from

$$v_{z=\delta} = \frac{1}{\rho_l A}\frac{dm}{dt}. \tag{3.3.3}$$

The lateral vapor flow through the vapor layer was taken as parabolic (V. P. Carey, 2008) as

$$\frac{u}{u_m} = 6\left(\frac{z}{\delta} - \frac{z^2}{\delta^2}\right), \tag{3.3.4}$$

where u_m is the average horizontal velocity in the vapor layer and was taken as

$$u_m = \frac{1}{\delta}\int_0^{\delta} u dz. \tag{3.3.5}$$

Together with Eq.(3.3.1), a well-known format (Biance et al., 2003) in Eq. (3.3.6) was obtained to represent the upward supporting force by viscous pressure through the integration over the entire contact area

$$F_{up} = \frac{3\mu_v k_v \Delta T \pi r_0^4}{2 h_{lv} \rho_v \delta^4}. \tag{3.3.6}$$

The hydrostatic pressure and electric force stress exerted on the bottom surface were scaled as $\rho_l gH$ and $\frac{1}{2}\varepsilon_v\varepsilon_0(\Delta E_v)^2$ (Woodson & Melcher, 1968) (Stratton) (Jones, Fowler, Chang, & Kim, 2003) respectively. H is the height of the drop which was evaluated as $R + \sqrt{R^2 - r_0^2}$. ε_v and ε_0 are vapor and vacuum permittivity respectively. If U(t) was a constant DC potential or time dependent sinusoidal wave

$$U^2(t) = (U_{max}\sin(\omega t))^2 = U_{RMS}^2 - U_{RMS}^2\cos(2\omega t), \tag{3.3.7}$$

where ω ($2\pi f_E$) is the angular frequency of electric signals. The root mean square value for sinusoidal waves was expressed as $U_{max}/\sqrt{2}$. The dielectric and hydrophobic layer thickness are much thinner than water vapor layer, thus has a negligible role for the contribution of electric stress. However, due to the finite conductivity and effect of dielectrophoresis, the RC circuit model (Jones et al., 2003) was employed in Fig.3.2.1. The capacitance and conductance were expressed for liquid and vapor respectively in Table.3.1.

Table 3.1 **Conductance and capacitance of electric circuit**

C_l	C_v	g_l
$\frac{\varepsilon_l \varepsilon_0}{H}$	$\frac{\varepsilon_v \varepsilon_0}{\delta}$	$\frac{\sigma}{H}$

The compromised electric field in vapor film became

$$E_v = \frac{g_l^2 + C_l(C_l + C_v)\omega^2}{g_l^2 + (C_l + C_v)^2\omega^2} \frac{U(t)}{\delta}. \tag{3.3.8}$$

Here an approximation was made about the influence of needle on undermining the gravitational force contribution. σ_{lv}^* is surface tension at saturation temperature. $S^*$is the perimeter of inserted needle, the diameter of which is around 100 μm. Φ is the contact angle (30°) where water contacts with the needle. With the existence of top electrode needle, Leidenfrost temperature on the original hydrophobic surface may be lower than expected as well as contact radius. After taking all those stresses acting on the bottom interface into consideration, a more proper equation of second order differential equation to predict th dynamic variation of vapor layer thickness (δ) could be constructed as

$$\frac{3\mu_v k_v \Delta T r_0^2}{2h_{lv}\rho_v \delta^4} - \frac{3\mu r_0^2}{2\delta^3}\frac{d\delta}{dt} = \rho_l g H - \frac{\sigma_{lv}^* \ S^* \cos\varphi}{A} + \frac{1}{2}\varepsilon_v \varepsilon_0 \left(\frac{U(t)}{\delta}\right)^2 + \rho_l H \frac{d^2\delta}{dt^2}. \tag{3.3.9}$$

The velocity of horizontal vapor flow could be expressed by

$$u_m = \left(\frac{r_0}{2\delta}\right)\left[\frac{k_v \Delta T}{\rho_v h_{lv} \delta} - \frac{d\delta}{dt}\right]. \tag{3.3.10}$$

For a Leidenfrost droplet, an electrostatic force tended to drag the bottom interface to approach the wall. Based on the experimental observation. A proper threshold voltage was often required to change the Leidenfrost state (Shahriari et al., 2014). A minimum voltage was applied as lowering the bottom interface to initiate liquid re-contact with the hot surface. However, if just from force balance perspective, both the EW stress and upward vapor pressure seem to increase along the reduction of vapor layer thickness and the latter has a larger climbing rate. It seemed to make contact impossible (Shahriari et al., 2014). However, the lateral vapor flows faster beneath the drop from accelerated liquid evaporation due to thinner conduction thickness and also makes an accommodation to the more restricted vapor passage.

Figure 3.3 depicted that the vapor layer thickness variation by ACEW under different frequencies at a wall condition of 380 ^{o}C. From experiment, at a droplet (20 μl) experiencing a DC-transient signal (56 V) started to move from one equilibrium state to another equilibrium state but failed to rewet as the voltage was relatively low. When the bottom interface started to move, the impeding force decelerates the movement, and make it stable in another energy minimized state as long as the interface stayed stable.

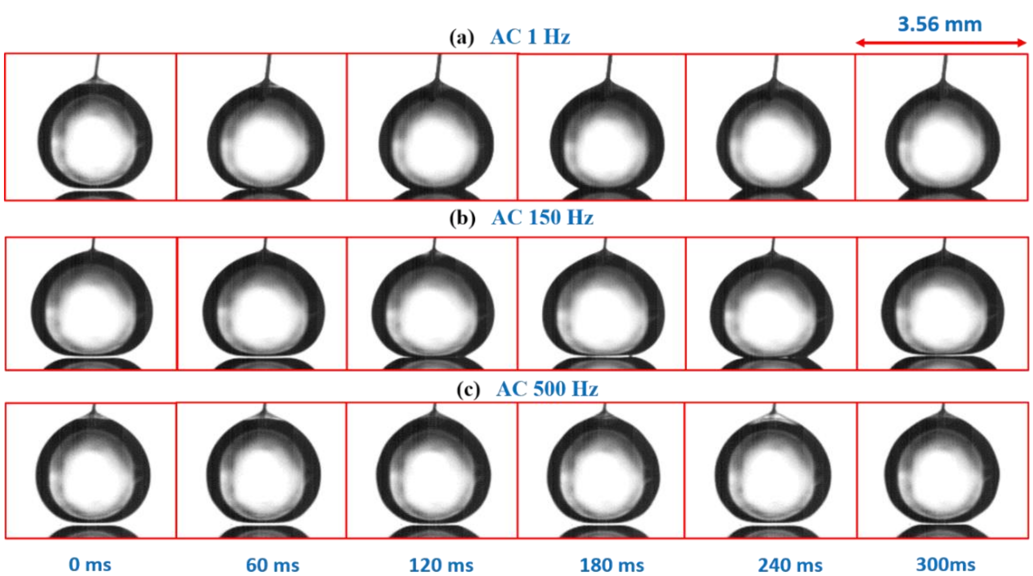

Figure 3.3. Experimental observation with the aid of high speed camera about vapor layer dynamic evolution by EW (U_{RMS}=56 V) under different frequency-driven conditions at 380°C: (a) f_E=1 Hz, (b) f_E=150 Hz and (c) f_E=500 Hz

The transient change of vapor layer thickness for a 56 V DC signal was computed in Figure 3.4a. Different from an impinging droplet, the shear force ($6\pi\mu Rv$) of surrounding vapor force maybe a considerable factor (Quere, 2013) for damping. For EW-actuated droplet, the additional viscous stress (the left second term of Eq. (3.3.9)) had a much higher order of magnitude to make the movement damped. On the other hand, electrostatic force and inertia made it oscillate and overshoot the equilibrium position a couple of times before reaching a steady state. At the same wall temperature, when a sinusoidal signal was applied as shown in Fig. 3.3.2 a to 3.3.2c, at a relative low frequency (f_E=1 Hz), the vapor layer is capable of rewetting the surface. However, when frequency increased to 500 Hz, the contact gradually diminished and failed to make any further contact. To investigate and explain the observed experimental phenomena. The numerical results as shown in Figures 3.4b and 3.4c may reflect the experimental observations for non-wetting at higher frequency regime. At low frequencies, the interface movement could follow up with the external excitement. The interface achieved a great vapor thickness reduction companied with great flow velocity and electric field strength. Afterwards, the droplet were doing irregular motions governed by spherical harmonics and shaking irregularly at different resonance modes (Y. Lu et al., 2017). When frequency was going up to this limit, the time-varying electric signal can no longer oscillate the vapor interface as well as the dielectrophoresis effect. This finding coincided with previous scientific reports for non-dimensional analysis as regard to forces acting on EW driven droplet at room temperature (Celestini & Kirstetter, 2012). If $\Delta\delta$ is a small disturbance of δ and represents the dynamic variation in the vicinity of equilibrium state at $U_{RMS.}$. The amplitude could be determined by differentiating the viscous pressure as $(\Delta P) \sim -\frac{6\mu_v k_v \Delta T r^2}{h_{lv}\rho_v \delta^5}\Delta\delta$. It may be balanced by the electric stress $(\frac{1}{2}\varepsilon_v \varepsilon_0 (\frac{U_{RMS}}{\delta})^2)$ and inertia $(\rho_l H d\delta f_E^2)$ in Eq. (3.3.11). The maximum thickness oscillation requires a high voltage and low frequency level. In addition, increased surface temperature can affect the thickness and thickness variation

$$\Delta\delta = \frac{\frac{\epsilon_v \varepsilon_0 V_{RMS}^2}{2}\delta^3}{\frac{6\mu_v k_v \Delta T r^2}{h_{lv}\rho_v} + \rho_l H f_E^2 \delta^5}. \tag{3.3.11}$$

3.3.2 Instability wavelength:

For the liquid-and-vapor interface, if any disturbance wave is present, we would like to know if it will grow or stay stable. Since any initial arbitrary waves generated on the interface could be expressed by Fourier series with a wide range of wavelengths. Here we focused on a certain range of wavelengths of Fourier waves that lead to wave growth. The Fourier wave could be expressed as

$$\delta(x, t) = A\cos(kx)e^{st}, \tag{3.3.12}$$

where s and k are angular frequency $(\frac{2\pi}{T})$ and wavelength number $(\frac{2\pi}{\lambda})$ respectively. The wave dispersion relation with respect to the wave form in Eq. (3.3.12) of the interface was well illustrated in literatures with or without the presence of Electric field (V. P. Carey, 2008; Johnson, 1968; Marco & Grassi, 1993) as

$$s^2 = k^2\left\{\frac{\rho_l \rho_v}{(\rho_l+\rho_v)^2}(\overline{u}_l - \overline{u}_v)^2 - \left[\frac{\sigma_{lv}k}{\rho_l+\rho_v} - \frac{\rho_l-\rho_v}{\rho_l+\rho_v}\frac{g}{k} - \frac{\varepsilon_{eq}E_0^2}{\rho_l+\rho_v}\right]\right\}, \tag{3.3.13}$$

where $E_0 (= \frac{U(t)}{\delta})$ is the applied electric field when the interface was not deformed. ε_{eq} is the equivalent permittivity.

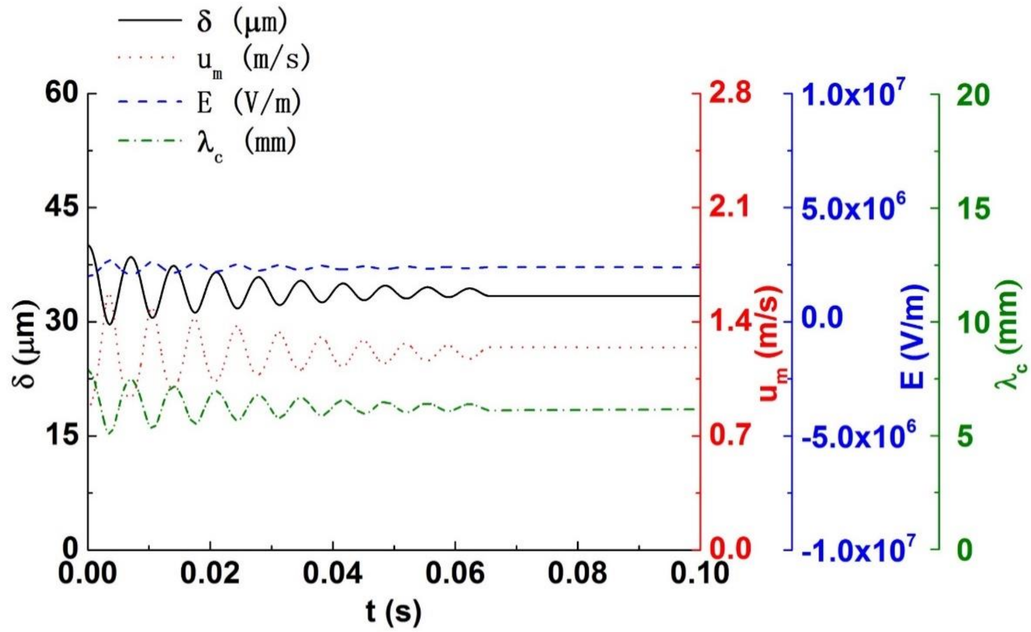

(a)

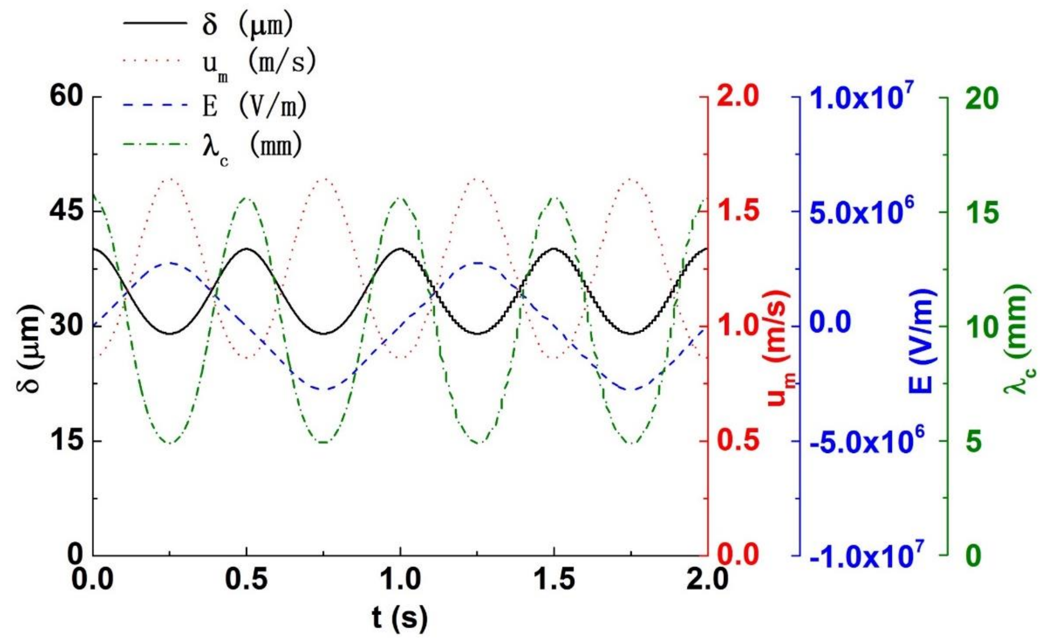

(b)

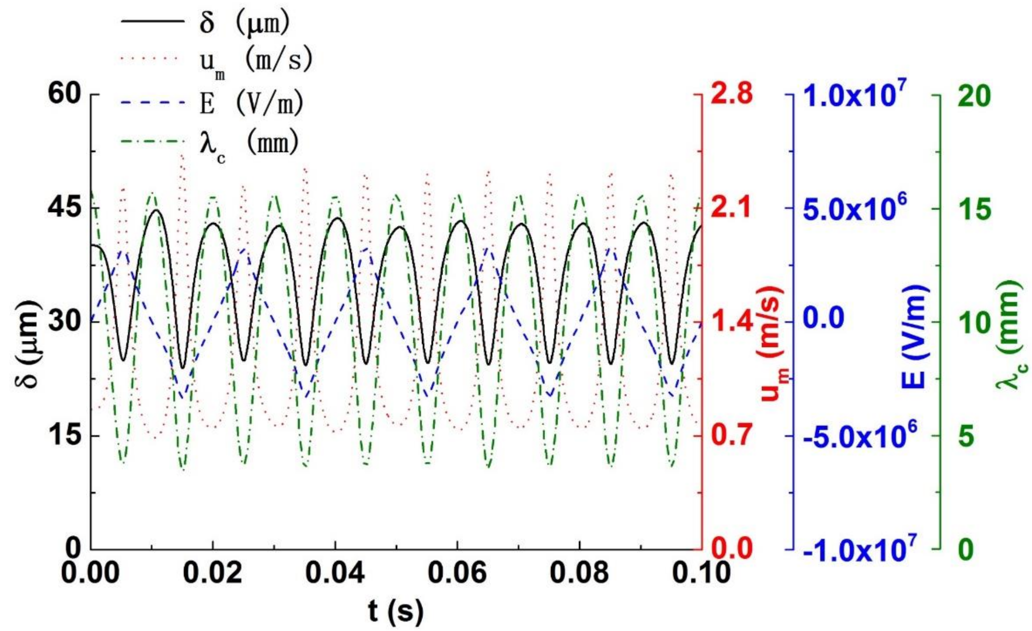

(c)

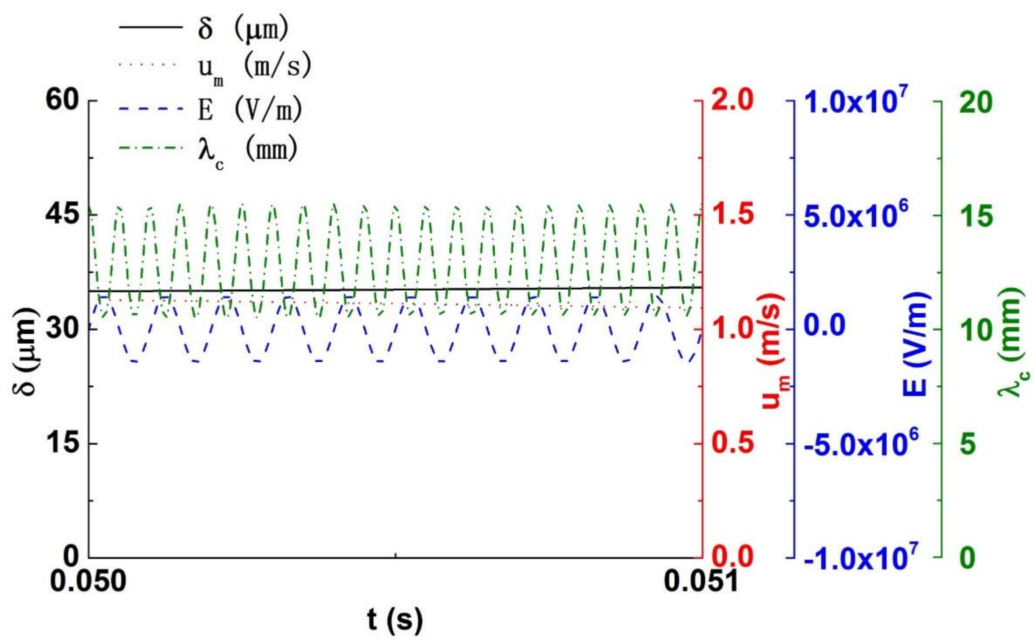

(d)

Figure 3.4. Vapor layer thickness, vapor flow velocity, electric strength (interface no deforming) and critical wavelength at 400 ^{O}C under (a) DC (56V) and AC Sinusoidal (U_{RMS}=56 V) (b) 1 Hz (c) 50 Hz (d) 10 kHz

The droplet was taken as conductive only deteriorate at extremely high frequencies. For a conductive liquid overlaying on a non-conductive vapor, ε_{eq} was usually expressed as $\varepsilon_0 \varepsilon_v$ (Carrica, DiMarco, & Grassi, 1996; F. Verplaetsen & Berghmans, 1997) while for an entirely insulted fluid ε_{eq} varies in different expression in the literature (Johnson, 1968; Marco & Grassi, 1993). $\overline{u}_l$ and $\overline{u}_v$ are horizontal velocity of vapor and liquid. As considered in a Leidenfrost droplet, $\overline{u}_l$ is much more trivial than $\overline{u}_v$, which may be approximately estimated as the average velocity of vapor flow u_m in Eq. (3.3.10).

From Eq.(3.3.10) , fast vapor flow generated by evaporation and a strong electric field when it got more approaching to the wall make the interface more vulnerably influenced for a wider range of instability wavelengths. The interface become unstable when the wave on the droplet boundary grew, in other words, s has a positive real part which gave a critical wavenumber as

$$k_c = \frac{2g(\rho_l - \rho_v)}{-(\rho_v u_m^2 + \varepsilon_{eq} E_0^2) + \sqrt{(\rho_v u_m^2 + \varepsilon_{eq} E_0^2)^2 + 4g\sigma_{lv}(\rho_l - \rho_v)}}. \quad (3.3.14)$$

In Figure 3.5(a), the critical wavelength λ_c in the presence of electrowetting at different wall temperatures were plotted. Here we compared it with droplet length scale (which is roughly the half of droplet perimeter). The interface became unstable below this limit. It certainly had a great meaning of vapor layer collapse. The collapse of interface indicated a Leidenfrost point at this specific frequency. Thus the dependence between LFP and frequency thus was presented in Figure 3.5b, which matches well with the experimental AC driven minimum threshold frequencies. This paper gave an outlook for future studies on film boiling under electric suppression, especially for those cases when a more sophisticated heat and mass transport system was involved as regard to enhancing CHF and LFPs.

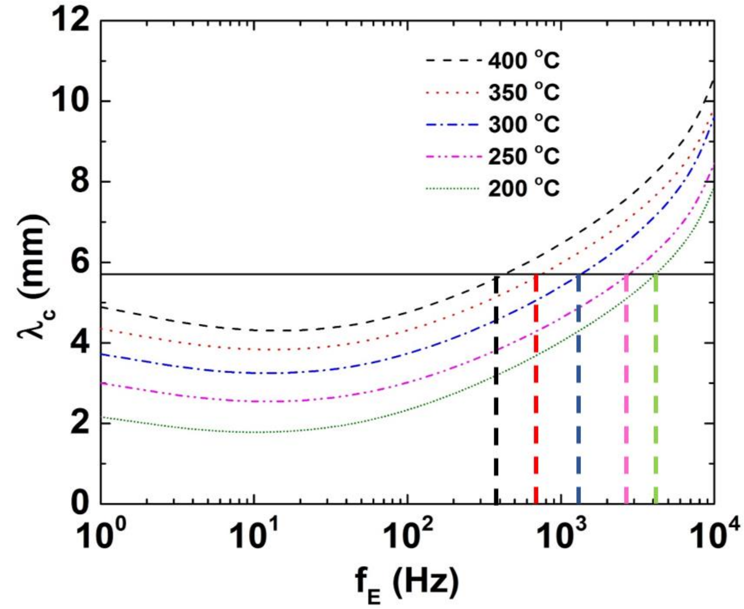

Figure 3.5. The minimum interfacial critical wavelength in different ACEW (U_{RMS}=56 V) frequency-driven conditions. The solid line is a length scale of the droplet. Under this limit, the interface becomes unstable.

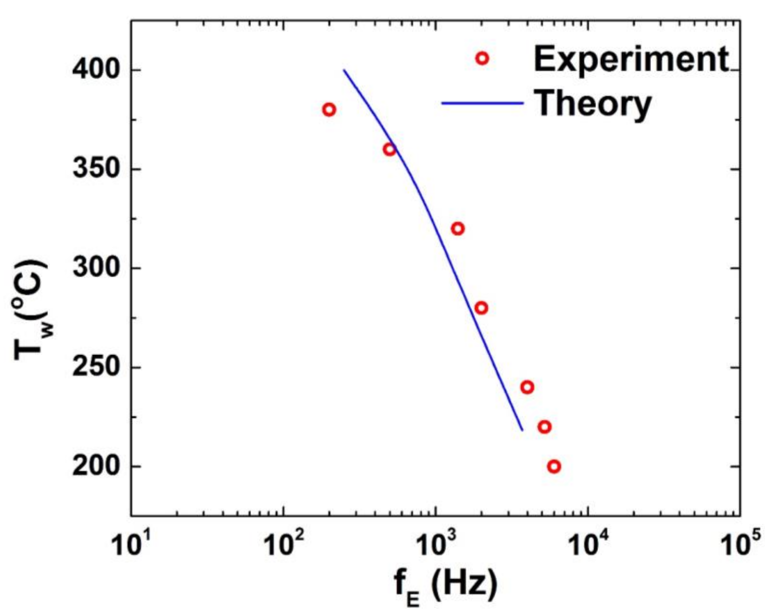

Figure 3.6. Scattered points were experimental results of minimum frequencies to cause suppression for a surface temperature of an equivalent AC sinusoidal waves (U_{RMS}=56 V), the solid curve was theoretical prediction.

3.4 Visualization of Leidenfrost suppression

Leidenfrost phenomenon is closely related to film boiling and the critical heat flux (CHF) limit of boiling heat transfer. Understanding the mechanisms of Leidenfrost phenomenon and devising effective ways to suppress it is of great interest to heat transfer enhancement community. In this work, a synchronized high-speed optical imaging and infrared (IR) thermography approach was employed to investigate the dynamics of a Leidenfrost droplet under the influence of electrowetting (EW). The Leidenfrost droplet was produced by dispensing a water drop on a Teflon-coated silicon wafer maintained at a wall temperature of T_{wall} = 210 ºC. Both direct-current (DC) and alternating-current (AC) electric fields were applied to induce EW effects to suppress the Leidenfrost state. The interfacial instabilities of the Leidenfrost droplet were observed, and the instantaneous temperature and heat flux distributions on the heating surface were measured. The results suggest that the electrical forces destabilize the liquid-vapor interface and cause the vapor film that insulates the heating surface from the droplet to collapse. The re-establishment of the liquid-solid contact helps to drastically improve the heat transfer, as evidenced by the reduced surface temperature and the enhanced heat flux.

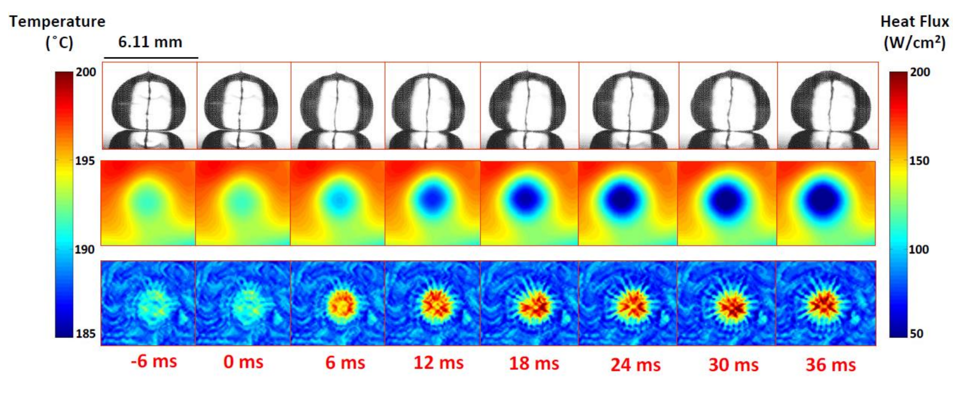

(a) DC signal (V=100 V)

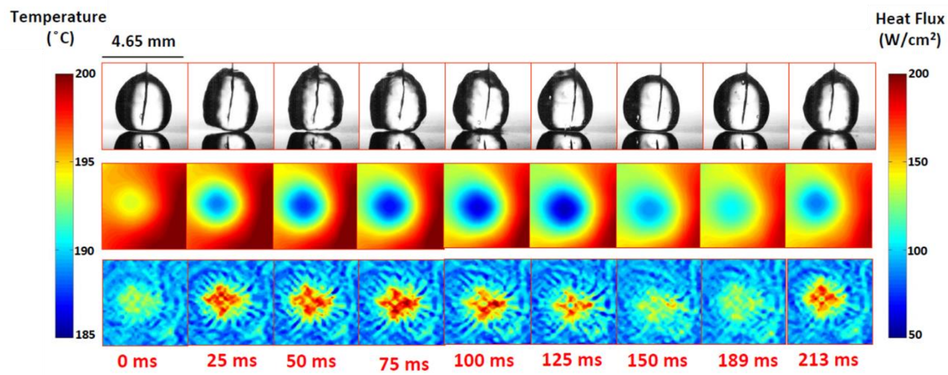

(b) AC signal (V_p=100 V, f_E=5 Hz)

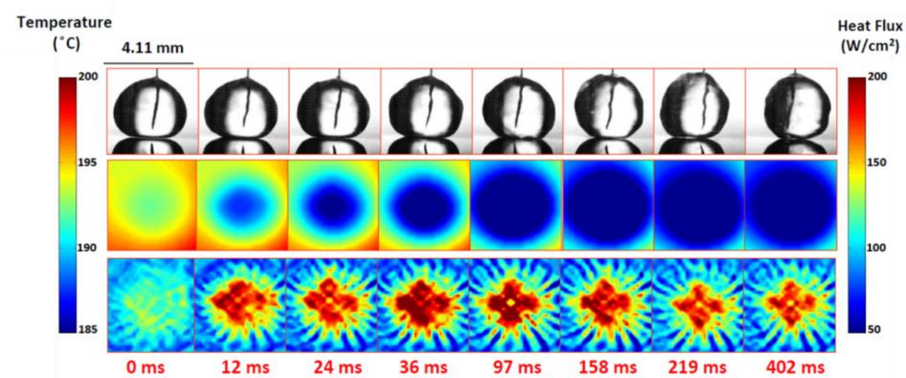

(c) AC signal (V_p=100 V, f_E=1000 Hz)

Figure 3.7. Synchronization of optical images for droplet dynamic motion and IR images for temperature and heat flux of heating surface during (a) DCEW and ACEW actuation at (b) 5 Hz and (c) 1000 Hz.

3.5 Conclusions

Study of electrowetting effect on Leidenfrost state suppression was carried out in this paper. Vapor layer vibrations and instability interface were observed. The stability of liquid-and-vapor interface was broken under DC or AC EW signals in a certain range of temperature. The major finding in this paper were summarized as below. a) Electric actuation on micro-liter sized drop under DC or AC signal were substantiated for suppressing Leidenfrost effect b) AC signal has a dynamically impact on LFP suppression and heat transfer enhancement c) We experimentally observed the contact between liquid and substrate took place and few liquid "fingers" appeared beneath the suspended liquid drop. d) Inertia played an important role on the dynamic liquid quenching process, thus to be a non-negligible factor in terms of applied frequencies, especially to compromise the electric signal in the high frequency regime. E) More violent vapor flows and strengthened electric field influenced the critical wavelength to cause vapor film unstable and liquid contact.

Chapter 4 Electrowetting Enhancement of Critical Heat Flux

4.1 Introduction

Critical heat flux (CHF) is an indication of a heat dissipation crisis, most of the time, occurs in a boiling system which is experiencing dramatic liquid-and-vapor phase change. The occurrence of a maximum heat flux threshold is imputed to the block of passage of liquid reverse flow and surface occupation of vapor. As a result, the loss of liquid-rewetting and a relative large vapor thermal resistance impede boiling heat transfer. A variety of models (Dhir & Liaw, 1989; Haramura & Katto, 1983a; Kandlikar, 2001; Kutatelasze, 1948; Lienhard & Hasan, 1979; Zuber, 1959) theoretically explained and were formulated in terms of critical heat flux (CHF) in the last few decades. Kutateladze (Kutatelasze, 1948) conceived the scenario that a drop experiences upward surrounding vapor viscous force and downward gravitational force. When the upward force exceeds the downward force, the drop can no longer return to the surface thus CHF occurs. Zuber's (Zuber, 1959) model was described that the substrate surface was spaced and consistently occupied by vertical vapor columns in Figure.4.1a. When stability was broken and the vapor column collapsed, the boiling system eventually reached a state of liquid-and-surface detached by vapor film in Figure 4.1b.

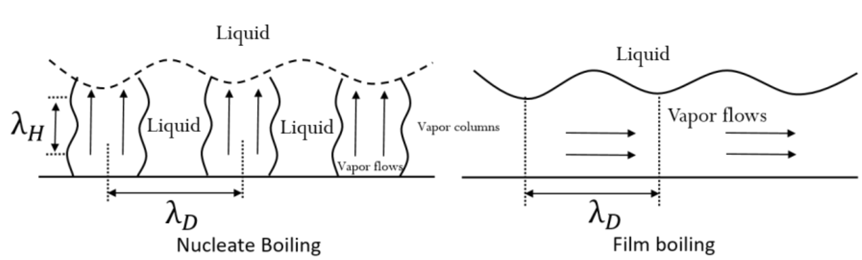

(a) (b)

Figure 4.1 a) Nucleate boiling (b) Film boiling

The stability of vapor column was governed by Helmholtz instability wavelength (λ_H). However, the distance of each adjacent vapor columns was assumed to be Tayler instability wavelength or most dangerous wavelength (λ_D). The equivalence of those two instabilities wavelength is perhaps the most obscure part to be visualized. But it provided a way to connect the stability of vapor jets to the expression of critical heat flux which was predicted

$$q_c" = K\rho_v^{1/2} h_{lv} [(\rho_l - \rho_v) g \sigma_{lv}]^{1/4}, \tag{4.1.1}$$

where values of K were chosen differently by 0.131 to 0.149 in Zuber's and Kutateladze's models. The hydrodynamic theory was also illustrated by Chang (Chang, 1961) for choosing a different pre-factor of K in vertical surfaces. CHF occurred when a critical value of Weber number was reached. Similar approach was conceived by Lienhard and Hasan (Lienhard & Hasan, 1979) through equating the rate of vapor kinetic energy to the rate of surface energy which is required to disintegrate vapor column into bubbles. The size of the vapor column and bubbles were determined by Taylor instability wavelength. Lienhard and Dhir (Lienhard & Dhir, 1973) discussed from hydrodynamic perspective in detail about the applicability of this model on a variety of heaters of different sizes and geometries. Later Haramura and Katto (Haramura & Katto, 1983b) brought out the idea of "microlayer" by describing that the critical velocity was not only dependent on the liquid vapor interfacial instability but also actual fluid behavior. The downward liquid flows restricted by wall will spread to form a numerous small feeder jets under the vapor columns. The CHF will occur when these liquid columns are totally evaporated before the hovering bubble releases.

Hydrodynamic model were also more frequently associated with surface conditions (O'Hanley et al., 2013) and the types of fluids (H. S. Ahn & M. H. Kim, 2012; S. J. Kim, Bang, Buongiorno, & Hu, 2007; Park & Bang, 2014) in a boiling system. Fig. 4.2 gave a comparison about CHF values achieved on different surface conditions in recent research studies.

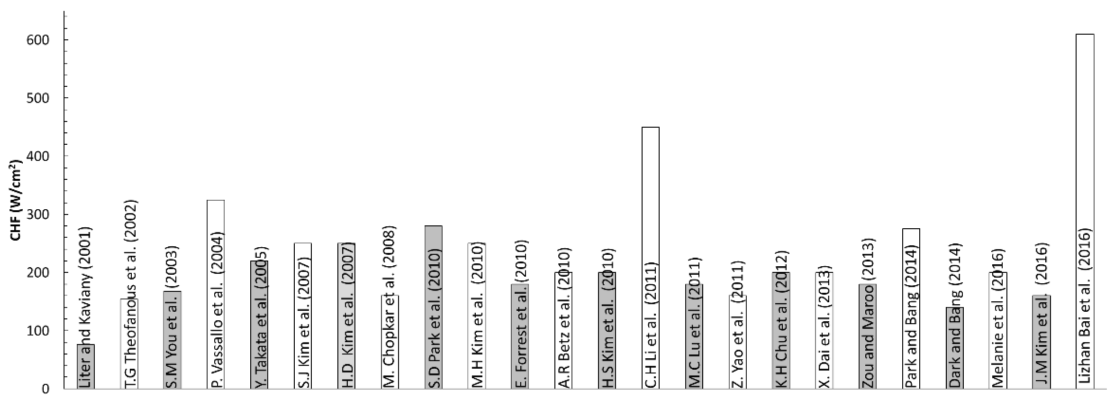

Figure 4.2. Review of recent research study on CHF

For example, surface microstructure (K. H. Chu, Joung, Enright, Buie, & Wang, 2013) or porosity (H. S. Ahn, Lee, Kim, & Kim, 2012) could effectively enhance the CHF value by affecting the hydrodynamic conditions. Structured surface was assumed to have an effect on the hydrodynamic Rayleigh-Taylor wavelength or vapor column area ratio compared with plain surface (Galloway & Mudawar, 1993; Hwang & Kaviany, 2006; Jo, Kaviany, Kim, & Kim, 2014; Liter & Kaviany, 2001; Quan, Dong, & Cheng, 2014; H. Wang, Peterson, & Asme, 2007). In addition, surface wettability was also a significant factor considered in earlier studies to play an important role in determining CHF. Hydrophilic surfaces have better liquid wetting capability than hydrophobic surfaces

(Takata, Hidaka, Masuda, & Ito, 2003). However, it was widely accepted that the wettability change could cause a direct influence on the contact angle. The contact angle dependent CHF model formulated by Kandlikar (Kandlikar, 2001) had a close relationship with hydrodynamic theory in expression of

$$\mathrm{K} = \frac{1+\cos\theta}{16}\left[\frac{2}{\pi} + \frac{\pi}{4}(1+\cos\theta)\cos\Omega\right]^{1/2}, \tag{4.1.2}$$

except that the coefficient of K is a function of contact angle β and surface inclination Ω.

The horizontal forces acting on a bubble could determine its lateral expansion thus affect the vapor film formation (Klausner, Mei, Bernhard, & Zeng, 1993). CHF occurs in the situation when a bubble starts to grow till covers the entire heater surface. At high heat flux level, the dominant expanding force is evaporation force which results in a large expanding momentum. However, surface tension and gravity act in an opposite direction to hold the bubble in place. In hydrodynamic model, surface tension and gravity have the same functioning in stabilizing the vertical liquid-and-vapor interface and preventing the system from becoming Helmholtz unstable. Therefore, Kandlikar's contact angle model (Kandlikar, 2001) shared common ideas with Zuber's hydrodynamic model (Zuber, 1959) by describing the transitional process from the nucleate boiling to film boiling. From either hydrodynamic or bubble dynamics perspective, it is worth noticing that surface tension and gravity on the one hand tends to maintain a relatively stable systematic heat and mass transport condition; On the other hand, a large heat flux and superficial velocity (A. Sur & Liu, 2012) cause destabilization and CHF advent. Recently, more advanced surface treatment technique made attempts to improve heat transfer coefficient (HTC) on less wetted surfaces. including UV-light oriented (Takata et al., 2005) or temperature-sensitive (J. M. Kim et al., 2017) smart materials. However, the changed wettability had a noneffective impact on CHF improvement according to experimental study (Maeng, Song, & Lee, 2016).

External fields (if applied) such as acoustic vibration (Jeong & Kwon, 2006), magnetic (Lee, Lee, & Jeong, 2012) and electric field (Johnson, 1968) were substantiated as ways to efficiently and dynamically affect interfacial wavelength and suppress vapor film formation. Especially, the electrohydrodynamic (EHD) effect enhanced CHF study was explored thoroughly through experimental (W & D, 2006) and numerical (G & al., 2009; W. & Welch, 2007) methods. The EHD effect was mainly illustrated to reduce the critical interfacial wavelength and cause the disruption of vapor film. It is greatly beneficial to enhance either heat transfer efficiency or CHF under various electric induced circumstances (Berghmans, 1976). The affected critical wavelength brought out by Johnson (Johnson, 1968) had a close relationship with CHF and minimum heat flux. And Yih (Yih, 1968) illuminated an time–dependent interfacial conditions under time-variant sinusoidal AC signals and theorized with Matheus equation. Although those studies shed light on a possible influence of electric field to CHFs, technically application of a strong electric voltage (as high as 10^4 V) (F. M. Verplaetsen & Berghmans, 1999; Welch & Biswas, 2007) is inevitable and energy consuming. And it is worth noting that almost all those studies were constructed on a fixed originally static liquid-and-vapor interface and also without specifying in a more sophisticated heat and mass transport system. In reality, especially in a dynamic and electromechanically interacted system, the thickness of vapor layer δ is mutually dependent on vapor evaporation rate, electric field strength and the horizontal vapor flows. Recently, Experiment has shown that a relative low amplitude of electric signal (10^2 V/m) was employed to potentially induce a 200% CHF enhancement

(S. A. e. al, 2015; Shahriari, Hermes, & Bahadur, 2016b). Also a stable film boiling state was greatly reversed to nucleate boiling in the presence of the electric field.

Electrowetting force has been frequently mentioned as a very effective means due to its relevance in controllable microfluidic flow, such as surface rewetting of micro-liter volume droplet (F. & al, 2005) or bubble in a liquid pool (Ko, Lee, & Kang, 2009; SK, 2010; Y & SK, 2006). In the followed context, EW's effect on boiling CHF would be discussed from traditional EHD perspective as well as bubble dynamic perspective (Kandlikar, 2001). The suppression of vapor film in a boiling setup resembles a Leidenfrost droplet. The improvement of LFP has been discussed. The stress acting on the interface was attributed for causing displacement and instability of and on the interface. However, EW can also be viewed as functioning on a bubble in a liquid pool. It was observed as low voltage requirement, low energy consumption and swift transition for a single bubble in a boiling apparatus. It leads to more efficient heat transfer under a relative weak electric field condition as EW was usually regarded in a form of a local strong electric stress (Maxwell stress) acting at the three-phase contact line (TCL) (K. K. e. al, 2002). It is regarded as a convenient tool to change the contact angle of a droplet on a dielectric coated surface. Via a very small voltage (1-100 V), it potentially creates a local stress to cause a 40 to 50 degree change of contact angle after it reaches equilibrium (Y. Lu et al., 2017). In pool boiling, EW can either contribute for expediting the lift-up process or limiting the lateral spreading by creating more wetting area. In a bubble nucleation cycle, the advent of CHF may depend on the horizontal force balance acting on the bubble, which is determined by the inertia and viscosity (Hao & Prosperetti, 1999) as well as the finite electric conductive property

(Jones, 2009) of surrounding liquid. A discreet and comprehensive consideration of all involved parameters seems to be necessary to illuminate the sophisticated process.

If simplified, bubble growth is governed by Rayleigh-Plesset equation (L, 1917; Plesset & Prosperetti, 1977) for incompressible and inviscid surrounding liquid as

$$R\frac{d^2R}{dt^2} + \frac{3}{2}\left(\frac{dR}{dt}\right)^2 = \frac{1}{\rho_l}(P_v - P_l). \tag{4.1.3}$$

This expression is obtained by balancing the total kinetic energy $(KE)_l$ in the moving liquid surrounding a vapor bubble with net work W_l done against the surrounding liquid. For a small amplitude interfacial oscillation actuated by an external source, the time evolution of radius follows a second-order harmonic form by linearization of internal pressure

$$\ddot{x} + 2\beta\dot{x} + \omega_0^2 x = -\varepsilon\alpha e^{i\omega t}, \tag{4.1.4}$$

where x is the oscillation amplitude of a homogeneous spherical bubble where R could be expressed as $R_0[1 + x(t)]$. $\varepsilon(= \frac{\varepsilon_d V_{eff}^2}{2d\sigma})$ is a small parameter accounting for the effect of EW.α is expressed as $P_\infty/\rho_l R_0^2$. The natural angular frequency ω_0 is expressed as

$$\omega_0^2 = \frac{3\gamma}{\rho R_0^2}\left(P_i - \frac{2\sigma}{R_0}\right). \tag{4.1.5}$$

The inertial force can be regarded as the total kinetic energy contribution in the surrounding moving liquid as

$$F_i = \frac{d}{dt}\left(\int_R^\infty \frac{1}{2}(v_r^2)(4\pi\rho_l r^2 dr)\right)\frac{1}{v_R}. \tag{4.1.6}$$

Dielectrophoresis (DEP) (K. L. Wang, Jones, & Raisanen, 2007) or Electrowetting on a dielectric (EWOD) (Jones, 2009; Jones et al., 2003) are two potential effective microfluidic mechanism for manipulation of bubble translation or interfacial oscillations.

The primary difference between a EWOD and DEP actuated liquid motion is the low-and-high frequency limits of electrochemical response of the fluid to an electric field. Compared with studies which categorically took outside liquid environment as perfectly conductive (Y & SK, 2006), where the dominance of interfacial electric field strength subjected to interfacial free electric charges. The mobility of electric charge relax to the interface may be compromised after the frequency surpass the relaxation frequency in Eq. (2.5.2). At high frequency domain, the Dielectrophoretic (DEP) force due to the polarization become much more remarkable. The EW and DEP coupled electromechanical system was theoretically illustrated and experimentally verified by Jones (Jones et al., 2003; Jones, Wang, & Yao, 2004) for a sandwiched bubble apparatus. Recently, Experimental research on EW-actuated bubbles (Ko et al., 2009) also indicated that the movement of bubble interface was not observed up to 6 KHz for an 1μl bubble at room temperature. At critical high heat flux level heat transfer controlled phase, the concern of whether the inertia and viscosity be a dominant factor was questionable (V. Carey, Second Edition; Kandlikar, 2001). Because in the heat-transfer controlled stage of bubble growth, the rate at which heat is transported to the liquid-vapor interface of bubble becomes a major factor that limits the growth rate. A comprehensive analysis around above-stated factors was presented to unveil the key-parameters that cause enhancement of CHF and elimination of vapor film.

4.2 Experimental Setup

The experiments were conducted in a pool boiling apparatus in Figures 4.3 to 4.5. A 3” silicon wafer was used as the substrate which was pre-polished and coated with 5000 nm natural grown silicon dioxide. The heater was 2 cm square and was made of Chromium through vacuum-deposition with a thickness of 200 nm. The temperature gradient was neglected in silicon during heating process. There was also a copper pad for extended wire connecting to silicon directly which used as the bottom electrode while the other electrode was inserted into the water directly. The information for material properties and parameters used in the experiment as referred in the following context. The electric signal was provided by an arbitrary generator and amplified by a signal amplifier. A step voltage is employed for all the electric signal input unless otherwise stated. Measurement was conducted on DI (Deionized) water under DC and up to 1000 Hz AC. The heat flux was recorded by data acquisition system and an average of 20 data points were used to diminish the error of fluctuation. The temperature of the surface was captured and recorded by Infrared (IR) visual technique.

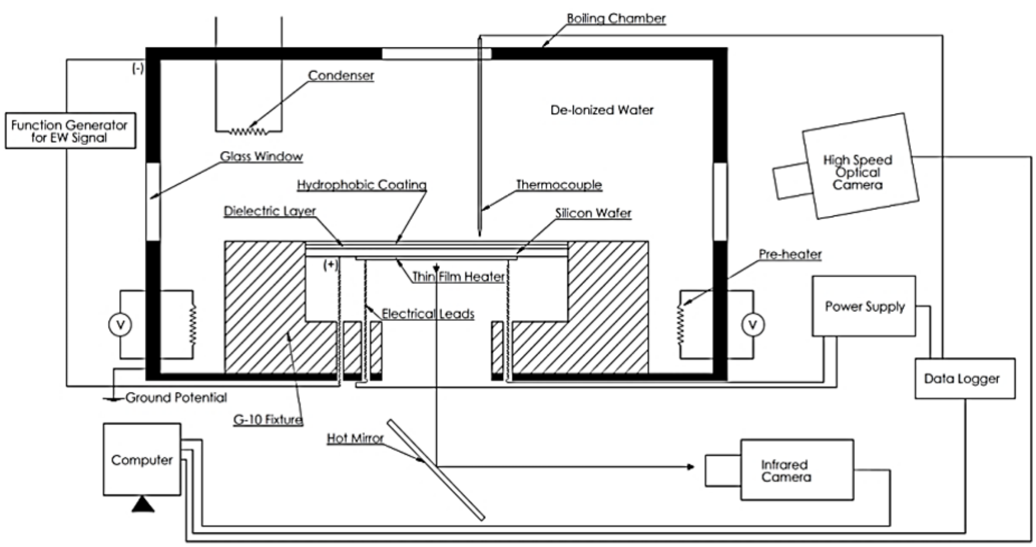

Figure 4.3. Schematics of boiling chamber for boiling experiment

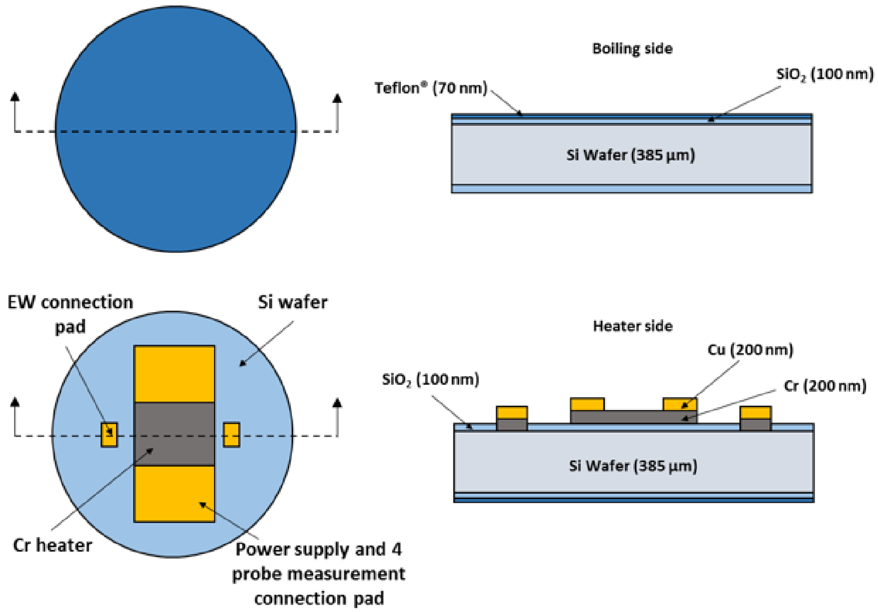

Figure 4.4. Silicon wafer microfabrication and functioning for both EW and heating substrate

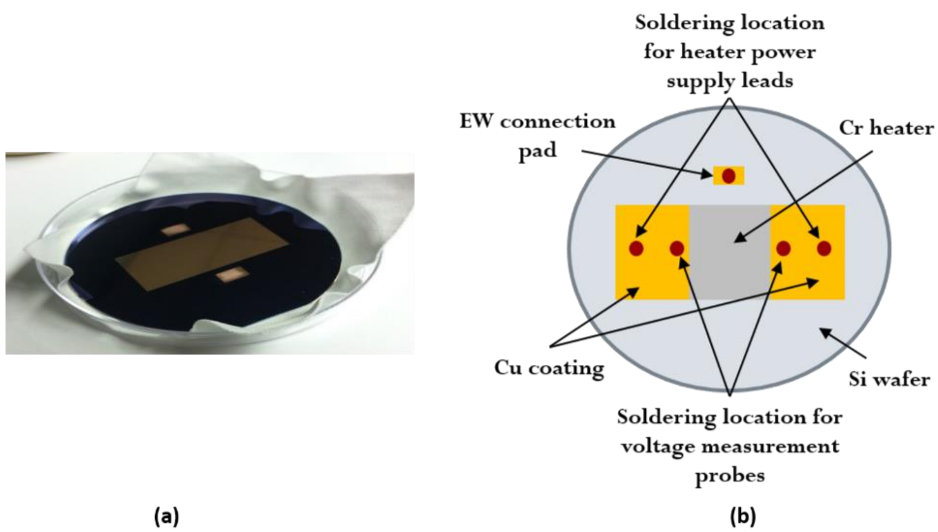

Figure 4.5 Heater and electric connections to the wafer

The boiling system under different electric signal was running from nucleate boiling to film boiling. The last point of every boiling curve shows where the system reaches film boiling. The average temperature of heater surface was calculated through an in-lab Matlab code to eliminate the influence of environment. The boiling chamber was preheated for 1.5 hour de-gassing process and all experimental measurement were conducThis dynamic motion has a dependence on the total horizontal forces acting on the liquid-and-vapor interface shown in Figure 4.6.

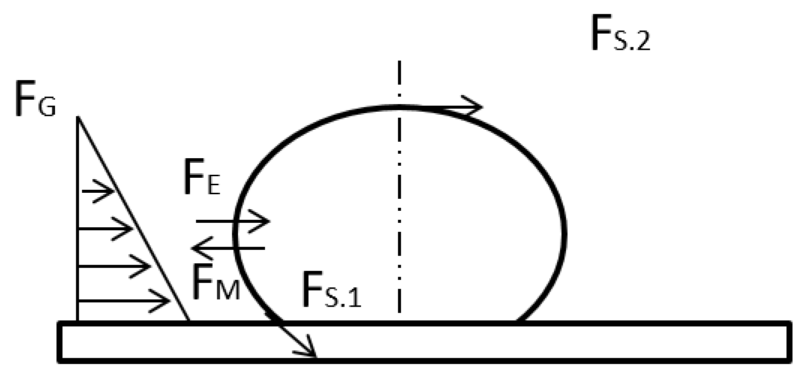

Figure 4.6. Forces acting on a bubble interface at CHF condition

The object was focus on the left half of the bubble of a 2D asymmetric schematic plotted at this condition.

4.3 Theoretical Background

CHF happens when unbalanced lateral forces made the bubble spread on the substrate

$$F_i = F_{S.1} + F_{S.2} + F_G + F_e - F_M, \tag{4.3.1}$$

Where the surface tension forces ($F_{S.1}$ and $F_{S.2}$) acting at the bottom and top surface respectively. The hydraulic pressure has a triangular distribution represented by F_G as a resultant. The force due to momentum change is represented as F_M due to the difference of specific volume of liquid and vapor in evaporation process. The inertial force (F_i) imposes a major restriction on the movement of interface. F_e is taken as a horizontal electric force caused by normal Maxwell surface stresses. CHF happens (Kandlikar, 2001; Klausner et al., 1993) if F_M become larger than the sum of all the impeding forces.

The surface tension forces were presented at top and bottom per unit length in the direction normal to the plane. At the bottom three phase contact line, the direction of surface tension force also depends on the contact angle in a form of

$$F_{S.1} = \sigma_{lg}\cos\beta \text{ and} \tag{4.3.2}$$

$$F_{S.2} = \sigma_{lg}, \tag{4.3.3}$$

where σ_{lv} and β are surface tension, N/m, and dynamic contact angle of the bubble. The receding or advancing contact angle were taken into consideration depending on whether liquid retreats or spreads. The gravitational force due to static pressure change along the interface is linear distributed. This results in a force parallel to an upward facing surface

$$F_G = \frac{1}{2}g(\rho_l - \rho_g)H^2. \tag{4.3.4}$$

The momentum force was produced due to the expansion of vapor during evaporation. It is the product of the evaporation mass flow rate and vapor velocity relative to the interface as

$$F_M = \left(\frac{q_I^{"}H \cdot 1}{h_{lg}}\right) \cdot \left(\frac{q_I^{"}}{h_{lg}\rho_g}\right), \tag{4.3.5}$$

where $q_I^{"}$ represents the heat flows across the surface with bubble's height (H) per unit width pointing normal outward. It is an average value during the growth of a bubble. By considering the size effect when it is close to a critical wavelength ($2\pi[\frac{\sigma}{g(\rho_l - \rho_g)}]^{1/2}$), a factor of η representing the ratio between heat release area and heat supply area was fitted for the experimental heat flux (M. C. Lu, Chen, Srinivasan, Carey, & Majumdar, 2011; M. C. Lu, Huang, Huang, & Chen, 2015). The heater size can be used instead to replace Helmholtz instability wavelength (M. C. Lu et al., 2015). the coefficient used in our paper was coincidentally the same with the one (0. 055) that Mingchang Lu (M. Lu, 2010) used for a same heater size. It directly relates to the general surface heat flux $q^{"} = \frac{1+\cos\beta}{16}\eta q_I^{"}$ under hydrodynamic condition (SG, 2001). The inertial force can be regarded as the total kinetic energy contribution in the surrounding moving liquid

$$F_i = \frac{d}{dt}\left(\int_R^{\infty}\frac{1}{2}(v_r^2)(4\pi\rho_l r^2 dr)\right)\frac{1}{v_R}, \tag{4.3.6}$$

where $v_R = v|_{r=R}$, and R is bubble radius. In spherical coordinate, for incompressible, radially symmetric flow of liquid near the bubble, conservation of mass gives a form of $\frac{dR}{dt}(\frac{R}{r})^2$ to represent v_R at an arbitrary location r. The final form of F_i per unit length is which coincides with the form given for a spherical cavitation bubble (MS. & A., 1977)

$$F_i = \rho_l v_R' R^2 + \frac{3}{2}\rho_l v_R^2 R. \tag{4.3.7}$$

The bubble was taken into consideration of a spherical-like geometry unless interfacial harmonic effect was considered in addition in our work. After substituting the expressions for all the forces, a heat flux representing the maximum heat flux at CHF condition was obtained

$$q_{CHF}^{"} = h_{lg}\rho_g^{\frac{1}{2}}\left(\frac{1+\cos\beta}{16}\right)\eta[\frac{\sigma_{lg}(1+\cos\beta)}{H} + (\rho_l - \rho_g)g\frac{H}{2} + \frac{F_e - F_i}{H}]^{1/2}. \tag{4.3.8}$$

where $H = \frac{D_c}{2}(1+\cos\beta)$ is the height of bubble. D_c is obtained by assuming it to be half of the wavelength of Talyer instability ($\lambda_c = 2\pi[\frac{\sigma_{lg}}{g(\rho_l-\rho_g)}]^{1/2}$) from hydrodynamic theory (SG, 2001; Zuber, 1959).

$$D_c = \lambda_c/2. \tag{4.3.9}$$

To determine the electric force on the interface, Korteweg-Helmholtz body force density (Woodson & Melcher, 1968) is used for the derivation of any potential forces

$$\vec{f}^e = \rho_f \vec{E} - \frac{1}{2} E^2 \nabla \epsilon + \nabla [\frac{1}{2} E^2 \frac{\partial \epsilon}{\partial \rho} \rho_l], \tag{4.3.10}$$

where E is the electric field, ρ_f is the volume density of free electric charge which is assumed to vanish everywhere in the bulk liquid but possibly exist at the surface, $\boldsymbol{\epsilon}$ is the permittivity. The last term on the right hand side of equation represents electrostiction. For a homogeneous and incompressible fluid, this term can be neglected. Clearly, the electric free charge and $\nabla\epsilon$ have only non-vanishing value on the interface. Thus, the component of electric forces that contributes to the motion of liquid are (i) the pondermotive force proportional on $\nabla\boldsymbol{\epsilon}$ and (ii) the force caused by free charge on the interface. A substitution form of ρ_f was expressed as $\nabla(\varepsilon\vec{E})$ in Gauss theory and an interfacial Maxwell stress tensor was thus formulated to represent the forces acting near the interface

$$T_{mn}^e = \varepsilon E_m E_n - \delta_{mn} \frac{1}{2} \varepsilon E_k E_k. \tag{4.3.11}$$

The Maxwell stress tensor may be used to give an expression for the pressure change across the interface (Jones et al., 2003)

$$\Delta P_e \approx \frac{1}{2} (\varepsilon_0 \varepsilon_l E_l^2 - \varepsilon_0 \varepsilon_v E_v^2), \tag{4.3.12}$$

where ΔP_e is the additional pressure caused by electrostatic force. The pressure difference depends on the electric field E and permittivity $\boldsymbol{\epsilon}$ on each side of the interface. In order to obtain the electric field strength, an equivalent electric RC circuit (Bhaumik, Das, Chakraborty, & DasGupta, 2014; Chatterjee, Shepherd, & Garrell, 2009) was employed for each section of the interested pill-box surface in Figure 4.7.

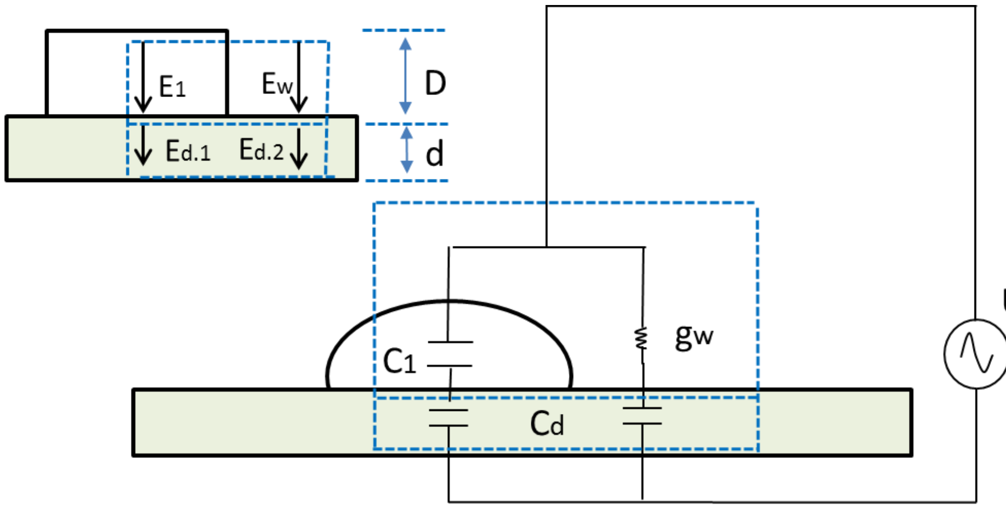

Figure 4.7. RC circuit for potential electric field on each side of surface

The component of time averaged electric forces were obtained from Eq. (4.3.13) to eq. (4.3.16), which takes the method of integrating the electric field along the pill box (Jones et al., 2003; Jones et al., 2004)

$$E_1 = \frac{U}{H} \cdot \frac{C_d}{C_1 + C_d}, \quad (4.3.13)$$

$$E_{d.1} = \frac{U}{d} \cdot \frac{C_1}{C_1 + C_d}, \quad (4.3.14)$$

$$E_{D.2} = \mathrm{Re}\left[\frac{U}{d} \cdot \frac{g_w/j\omega}{C_d + g_w/j\omega}\right] \text{ and} \quad (4.3.15)$$

$$E_{D.2} = \mathrm{Re}\left[\frac{U}{H} \cdot \frac{C_d}{C_d + g_w/j\omega}\right]. \quad (4.3.16)$$

The value of electric field strength was calculated based on the capacitance of each part of circuit. d is the thickness of dielectric layer. The capacitance and conductance were expressed per unite area and expressions for each phase are listed in Table 4.1.

Table 4.1. Capacitance and conductance for RC-circuit model of modeling EW force acting on a bubble

C_1	$C_{d,1}$	$C_{d,2}$	g_l
$\frac{\varepsilon_v \varepsilon_0}{H}$	$\frac{\varepsilon_d \varepsilon_0}{d}$	$\frac{\varepsilon_d \varepsilon_0}{d}$	$\frac{\sigma}{H}$

A combined form representing net electric force was expressed which included all the electric contribution to the forces acting on the bubble.

$$F_e = \frac{1}{2}\epsilon_d\epsilon_0 E_{d.1}^2 d + \frac{1}{2}\epsilon_v\epsilon_0 E_1^2 H - \frac{1}{2}\epsilon_w\epsilon_0 E_{w.1}^2 H - \frac{1}{2}\epsilon_d\epsilon_0 E_{d.2}^2 d. \tag{4.3.17}$$

4.4 Results and discussions

When turned on the electric signal where system was experiencing film boiling, the vapor film gradually retreated and nucleate boiling took place and liquid rewetted the surface after a few seconds. Figure 4.8 has shown at CHF state the boiling surface on original hydrophobic surface and under EW by IR and optical visualization technique. It also shown in Figure 4.9 the transition between nucleate boiling and film boiling and vice versa from film boiling back to nucleate boiling under EW.

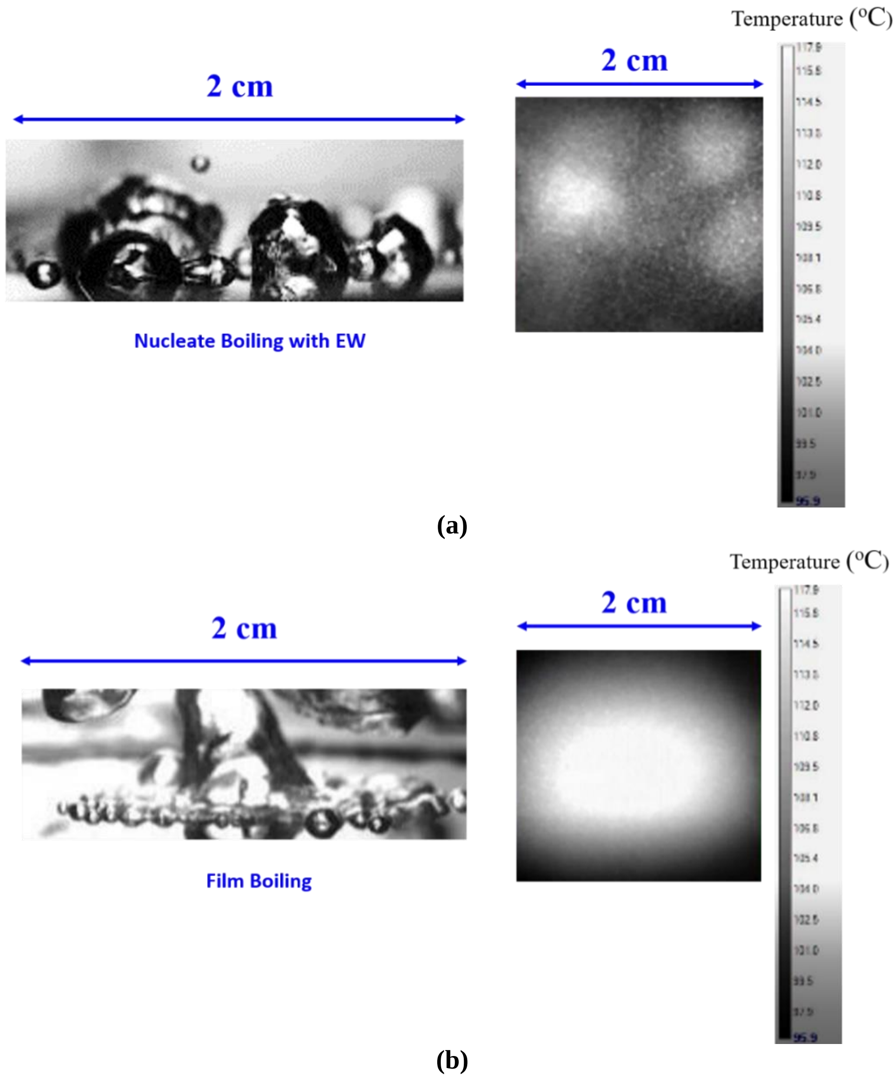

Figure 4.8. At same heat flux 7.5 W/cm^2 (a) Film boiling was suppressed under AC electric signal (110V, 100 Hz). (b) Film boiling after reaching CHF.

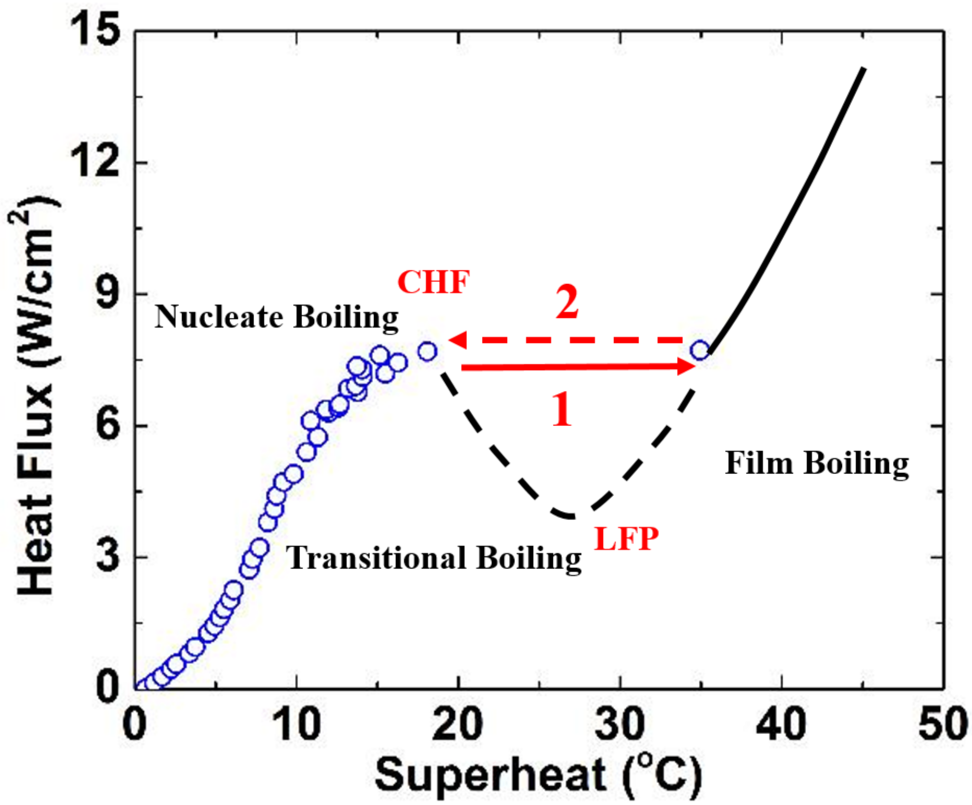

Figure 4.9. Film boiling curve on a hydrophobic surface, the transition from nucleate boiling to film boiling and from film boiling to nucleate boiling under EW actuation.

Based on above finding, it is reasonable to believe that EW can contribute to enhance CHF. A follow-up study about boiling curves under different EW conditions was plotted in Figure 4.10 by controlling electric frequency and voltage on a hydrophobic surface. In the same way, the scattered data consisting of each boiling curves were measured when system reaches a steady state with and without EW. Temperature was obtained as the average value of heat flux became steady. Repeatability of the measurements was repeated and verified by conducting multiple tests for each experimental condition. When heat flux increased to a certain level, the upper limit representing CHF was reached and a heat dissipation crisis took place.

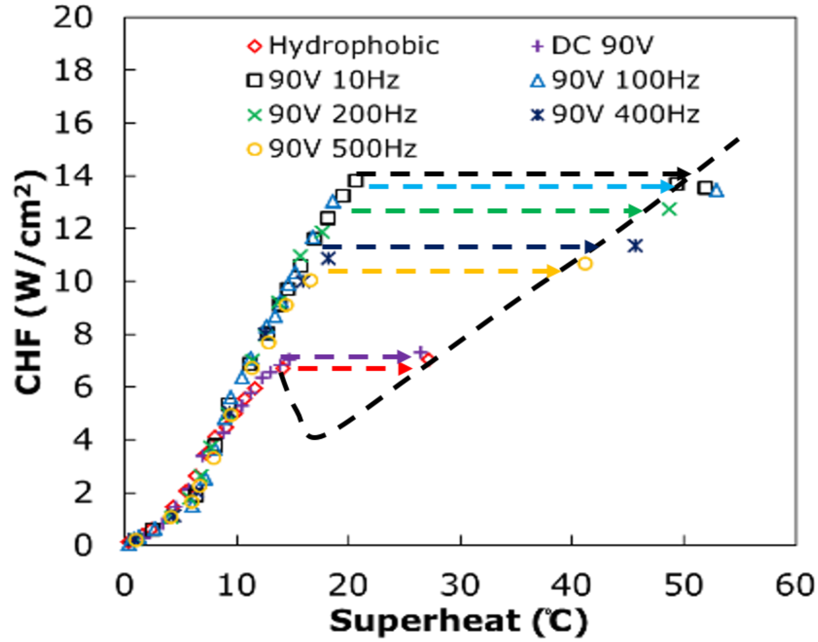

Figure 4.10. EW effect on boiling curves and modulation of CHF

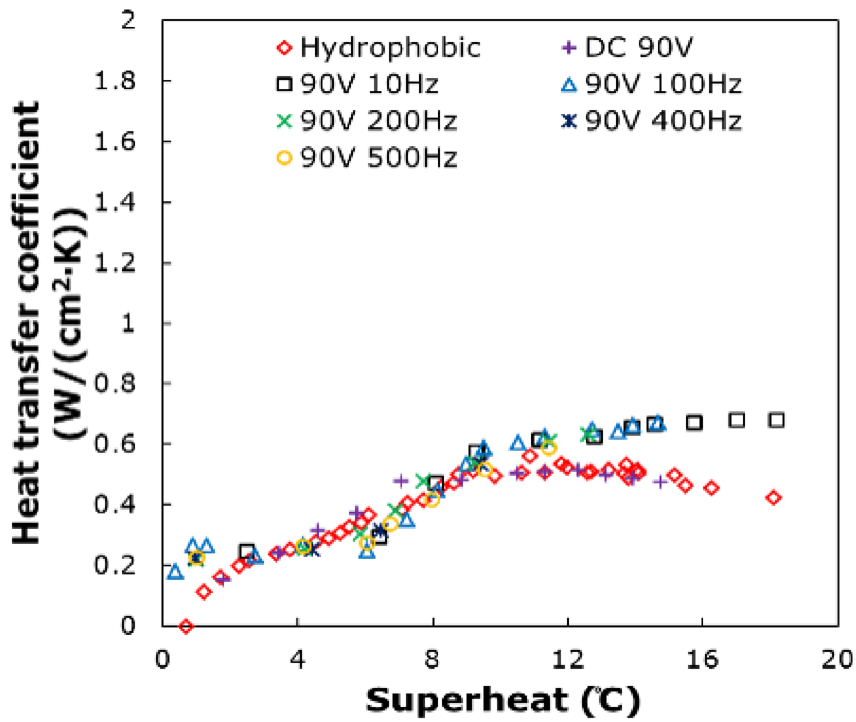

Figure 4.11. EW effect on heat transfer coefficient of boiling

Compared with 5 various conditions of electric frequency in Figure 4.10, CHF have been improved when AC electric signals were applied. In Figure 4.11, heat transfer coefficient has also shown a clear deviation after heat dissipation crisis was reached on the original surface. However, there was a continuation for each EW-driven curves until reach a higher level of heat flux via EW application. In addition, it was intriguing to find that a high frequency will deteriorate the effect of EW and data measured under DC signal shown little difference with bare hydrophobic surface. The explanation on how electric signal influence CHF may originate from multi-fold reasons. In the following discussion a possible reason was given from force balance perspective to illustrate the above findings.

The CHF values reach different values under different electric frequencies. As discussed in Chapter 2, One of a reason is that the increased inertia impede the bubble dynamics like EW-driven droplet (Y. Lu et al., 2017). Another reason from the discussion of Leidenfrost droplet in Chapter3 electric force has been weakened by dielectrophoresis effect. Figure 4.12 has plotted the electric force calculated from Equ.(4.3.17) in terms of different applied electric signals.

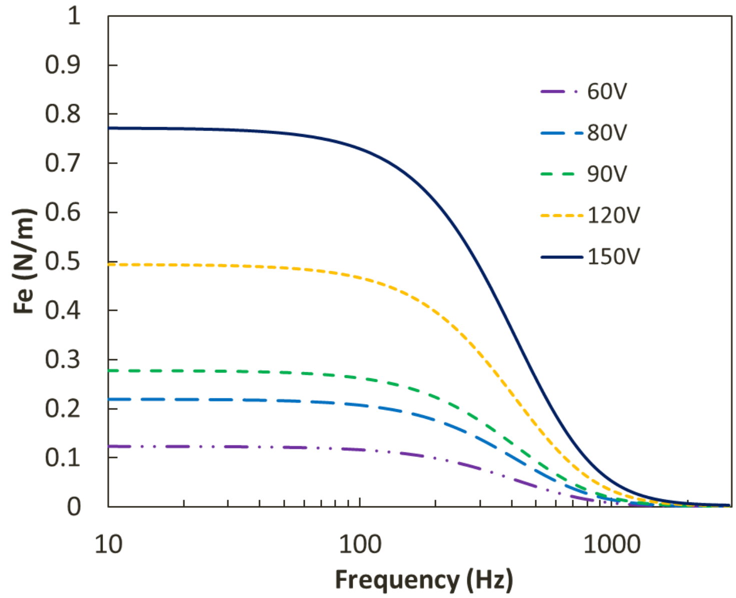

Figure 4.12. Electric force dependence on electric frequency and voltage

When the applied frequency exceeds a critical value, the accumulation of electric charge at the interface near the contact line is expected to diminish rapidly once $\omega > \omega_c$. The curves shown as a function of frequency in logarithm coordinates. It further clarified that beyond a critical frequency electric force decline rapidly. From the comparison of the capacitance in each part of the circuit, it is not difficult to observe that the critical angular frequency (ω_c) could be expressed

$$\omega_c \approx \frac{g_w}{C_d}. \tag{4.4.1}$$

When $\omega \ll \omega_c$, water was regarded as fully conducting and all the free charges accumulated at the contact line. On the other hand, if the frequency exceeded the critical frequency, the dominance of DEP undermines the electric force. The electric charge failed to relax to the three-phase contact line (TCL). The expression for EW and DEP was listed as

$$F_E = \begin{cases} \frac{\varepsilon_0 \varepsilon_d V^2}{2d} & \omega \ll \omega_C \\ \frac{(\varepsilon_w - \varepsilon_v)\varepsilon_0 V^2}{2D} & \omega \gg \omega_C \end{cases}. \tag{4.4.2}$$

From the expressions, it represents a voltage dependent electric force form respectively. The two expressions correspond to the perfectly conducting and perfectly insulating limits for liquids, again respectively. Clearly, the EW force is much greater than the DEP force. This transition from a strong EW force to a weak DEP force is due to the transition of electric charges from contact line to be evenly distributed over the liquid-vapor interface.

The inertia force may be a potential resisting force for bubble expansion and interfacial oscillation. But when compared the momentum force, the overall movements impeded by inertia was negligible.

Figure 4.13 has given a prediction by taking all the effects into account. The frequency dependent electric force model apparently did not include the DC case and frequencies below 10 Hz. Since film boiling was a dynamic process, we calculated the characteristic time for the cycle of a departure bubble expanding to a CHF bubble with critical wavelength dimension according to

$$\tau_c = \frac{q_1^{"} A}{h_{lg} m}, \tag{4.4.3}$$

where $q_1^{"}$ is the heat flux which stands for phase change efficiency. A is bubble dynamic surface area that evaporation take place. m is the total evaporated mass. An integration of time evolution from a nucleated bubble to a fully developed bubble that cause CHF

$$\tau_c = \int_{D_0}^{D_c} \left(\frac{16q''}{\eta(1+\cos\theta)} \frac{\pi D^2(1+\cos\theta)}{2}\right) / \left(h_{lv}\rho_v \pi D^3 \frac{2+3\cos\theta-\cos^3\theta}{24}\right) dD. \tag{4.4.4}$$

It is a characteristic time scale that represents bubble growth from nucleate boiling to film boiling.

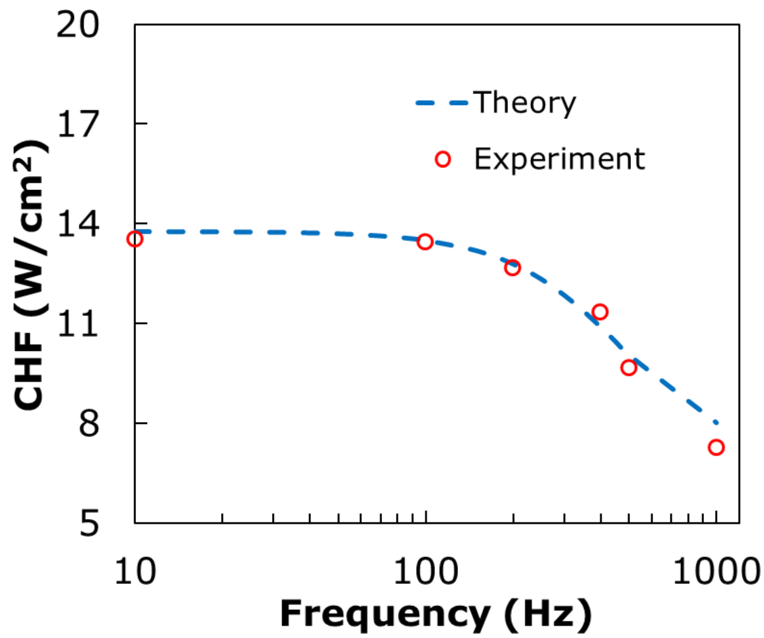

Figure 4.13. CHF values dependent on electric frequencies

The dimension D_0 for departure bubble is given as the maximum diameter for a nucleated bubble

$$\sqrt{\frac{g(\rho_l-\rho_v)D_0^2}{\sigma}} = 0.0208\theta, \tag{4.4.5}$$

where θ is the contact angle of bubble on a hydrophobic surface, here , the value of which equals to 120 degree. And D_C as defined in Eq.(4.3.9) From Eq.(4.4.4), the reciprocal of time τ_c was obtained as the minimum frequency that is needed for external electric force to take effect. The value we got for critical frequency is 0.1 Hz. We believe any frequency under this value is valueless to cause CHF. Considering all parameters and substituted into Eq. (4.3.8), the experimental results matches well with theoretical prediction.

4.5 Summary

Critical heat flux (CHF) was remarkably enhanced via AC electric signal. A predicted theoretical explanation was given through force analysis methodology. The Maxwell stress tensor in the form of electrowetting (EW) force plays a major role that impedes the vapor film expanding .The EWOD and DEP combined electrical force near the bubble-liquid interface was investigated to be frequency-dependent. The theory was verified by experimental data and observations.

The important findings can be summarized as: 1) The advent of CHF was delayed as a result of resisting electric force, (2) Electric force is dependent on frequency and work effectively below critical frequency, and 3) Boiling heat transfer rate was significantly improved at high heat flux regime compare with that on the hydrophobic surface. IV.The effect of other influencing factors such as inertia, friction force were proved as a minor factor that affect CHF and will be investigated in further experimental studies.

Chapter 5 Bubble Dynamics

5.1 Background

The process of one bubble ebullition cycle consists of liquid heating, bubble nucleation, bubble growth and departure. The frequency of bubble release defines as the reciprocal of total time of stated four different periods

$$\frac{1}{f} = t_w + t_g, \tag{4.5.1}$$

where t_w is the time period for liquid heating until required nucleation temperature was reached. $t_g$is the time from the appearance of bubble to departure from the surface. The frequency of bubble release was dependent on the departure volume, in other words, bubble's size. And the bubble's size was determined by the net force that was acting on the bubble which include vertical forces and horizontal forces. Vertical forces were commonly considered as the equilibrium of buoyancy force F_b and surface tension force F_s. Dynamically, the additional growth force F_g representing the resistance of surrounding liquid to the bubble growth was also considered. When the break of the balance took place or in other words, when the arising forces exceeds the downward forces, the bubble can no longer stay on the surface and depart. Otherwise it needs to be satisfied the equation

$$V(\rho_l - \rho_v)g - \pi r^2 \frac{2\sigma}{R} - 2\pi r\sigma \sin\theta = \pi R^2 \rho_l \frac{1}{2} u^2. \tag{4.5.2}$$

The horizontal force balance was simply subjected to Young-Lipmann equation

$$\cos\theta_E = \cos\theta + \frac{\varepsilon_0 \varepsilon_r}{2d\sigma} U^2. \tag{4.5.3}$$

In addition, the geometry contour of bubble tends to be a spherical subjected to surface tension which gave the relation of radius R and contact radius r

$$r_0 = R\sin\theta. \tag{4.5.4}$$

From Eqs. (4.5.2) to (4.5.4), it was not difficult to find that the departure volume V or bubble's size is reduced in the existence of EW. As the frequency and departure volume reflect the rate and capacity of energy transport by one bubble respectively and the relationship between these two factors are expressed as

$$fd_d = 0.59[\frac{\sigma_{LV} g(\rho_l - \rho_v)}{\rho_l^2}]^{1/4}, \tag{4.5.5}$$

where d_d is the departure diameter. From Eq. (4.5.5), it seems that the amount of liquid evaporated in one ebullition cycle is independent on the different condition of the surfaces. But bubble growth in different periods, dV/dt varies according to the limitation of surface properties such as contact angle, pattern boundary etc.

Due to the numbers of nucleated bubbles at low heat flux regime, the evaporation of bubble seems to be a minor factor for system heat transfer. On the other hand, bubble dynamic motions which include shrinking or spreading and interfacial spherical harmonic motion were induced by EW. Those dynamic effects were considered further facilitate the convection process originally enhanced through the agitation of surrounding liquid by the growth of nucleate bubbles. The heat transfer coefficient was affected by Reynolds number ($Re_{b,E}$) under EW effect at nucleate boiling regime and was written with a relation of the form

$$Nu_{b,E} = \frac{hL_b}{k_l} = ARe_{b.E}^n Pr_l^m, \tag{4.5.6}$$

where $Re_{b,E}$ was expressed by

$$\mathrm{Re}_{b,E} = \frac{\rho_v V_{b,E} L_b}{\mu_l}. \tag{4.5.7}$$

$V_{b,E}$ and L_b are velocity scale and length scale respectively. For a regular nucleate boiling regime without EW, Rohsenow (Rohsenow, 1951) defined the length scale L_b and velocity scale U_b as departure diameter of bubble and superficial velocity as

$$L_b = C_b \beta [\frac{2\sigma}{g(\rho_l - \rho_v)}]^{1/4} \text{ , and} \tag{4.5.8}$$

$$U_b = \frac{q^{"}}{\rho_v h_{lv}}. \tag{4.5.9}$$

However, Forster and Zuber (Forster & Zuber, 1955) used bubble growth radius R and the velocity of the interface $\dot{R}$ as a non-dimensional scales for L_b and U_b

$$L_b = 2R = Ja(\pi \alpha_l t)^{1/2} \text{ and} \tag{4.5.10}$$

$$U_b = Ja(\frac{\pi \alpha_l}{4t})^{1/2}. \tag{4.5.11}$$

Forster and Zuber’s model seemed to have a better description on the bubble growing stage and an intimate relation with wall temperature conditions. As regard to the EW aided bubble dynamic process. It may have different forms on those two scaling factors, theoretical and experimental data were still short in the literature to fit in this correlation. Thus more research study on this subject need to be carried out.

5.2 Experimental observations for bubble dynamics

In Figure 5.1, at 4.15 W/cm^2 and 5.62 W/cm^2 wall heat flux, the numbers of nucleate bubbles decreased after applying the EW signal, it indicated that the number of nucleation sites decreases after the surface become more hydrophilic due to EW effects.

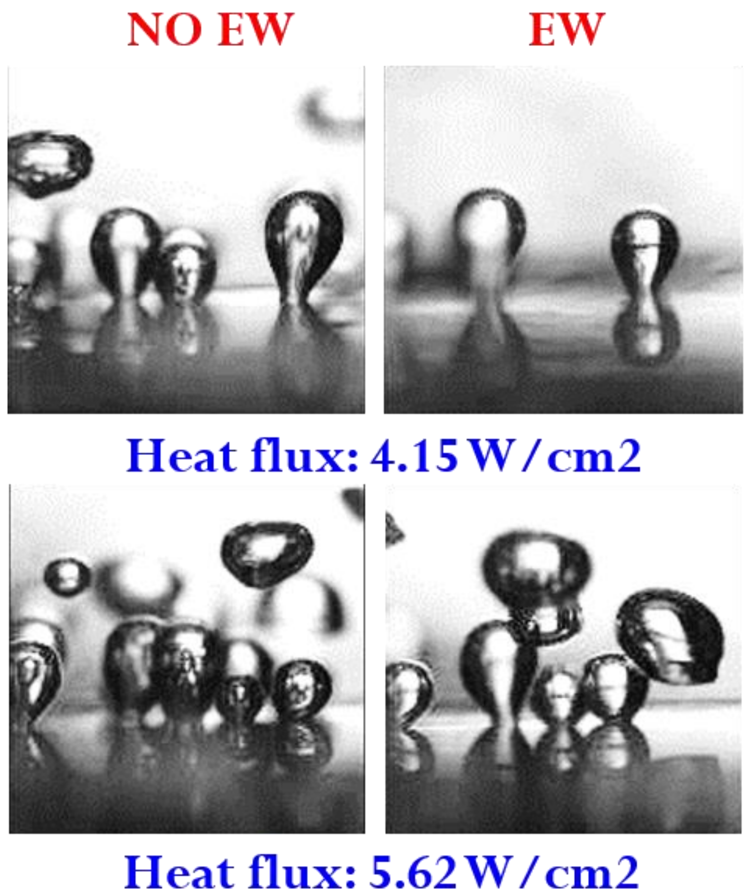

Figure 5.1. **heater surface with and without EW at 4.15 W/cm^2 and 5.62 W/cm^2**

Figure 5.2 also the compared with the shape of bubble contour, especially in the zoom-in region of the contact line, the contact area shrank and this was a clear evidence that EW by changing the contact angle to affect the growth rate and geometry.

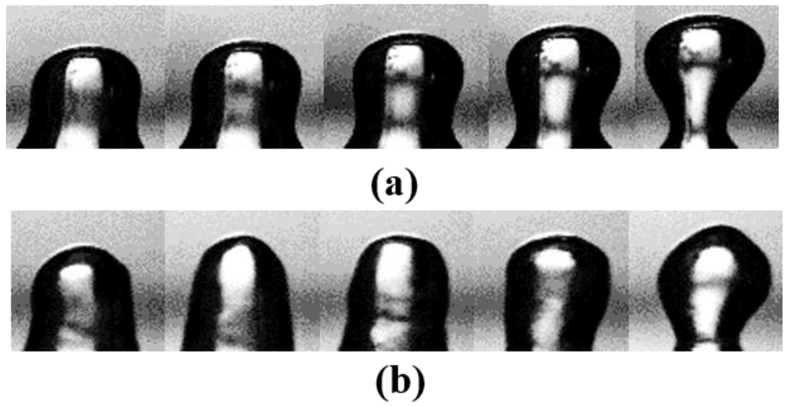

Figure 5.2. At 4.15 W/cm^2, the instant when bubble started to depart from hydrophobic surface and that in the condition of EW

The schematic plot of hydrophobic patterns on the hydrophilic surface in Figure 5.4 to Figure 5.6. Circular hydrophobic patterns with diameter in 0.2 mm, 0.5 mm, 0.8 mm, 1 mm and 2 mm were designed. And a corresponding rectangular shape pattern ranged from 1 mm to 6 mm of releasing in one dimension. For circular patterns, compared with bare hydrophilic and hydrophobic surface, pattern surface has a singular boundary to restrain the bubble growth and contact angle change. The frequency of bubble release was also compare in Table 5.1 and the departure geometry was restrained by the condition of surface in Figure 5.3.

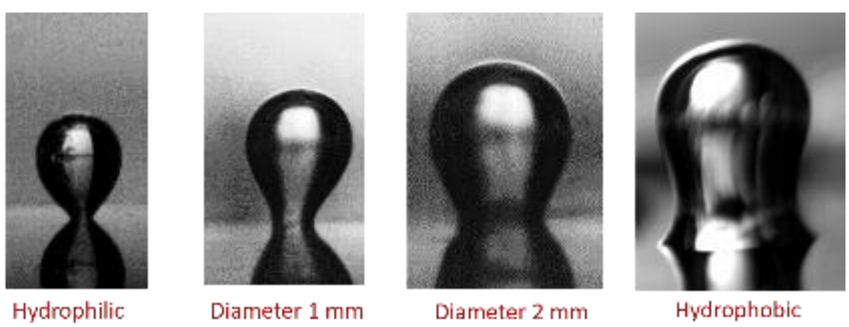

Figure 5.3. Bubble departure geometry on different surface conditions

However, the bubble ebullition cycles were merely affected by EW force for the designed series of pattern sizes. It was simply attributed to the limitation of static contact angle between hydrophobic and hydrophilic. The dynamic contact angle need to surpass this range to get rid of the boundary effect which is difficult to achieve in the presence of EW.

$$\theta_{\text{Hydropho.}} > \theta_d > \theta_{\text{Hydrophi.}} \tag{4.5.12}$$

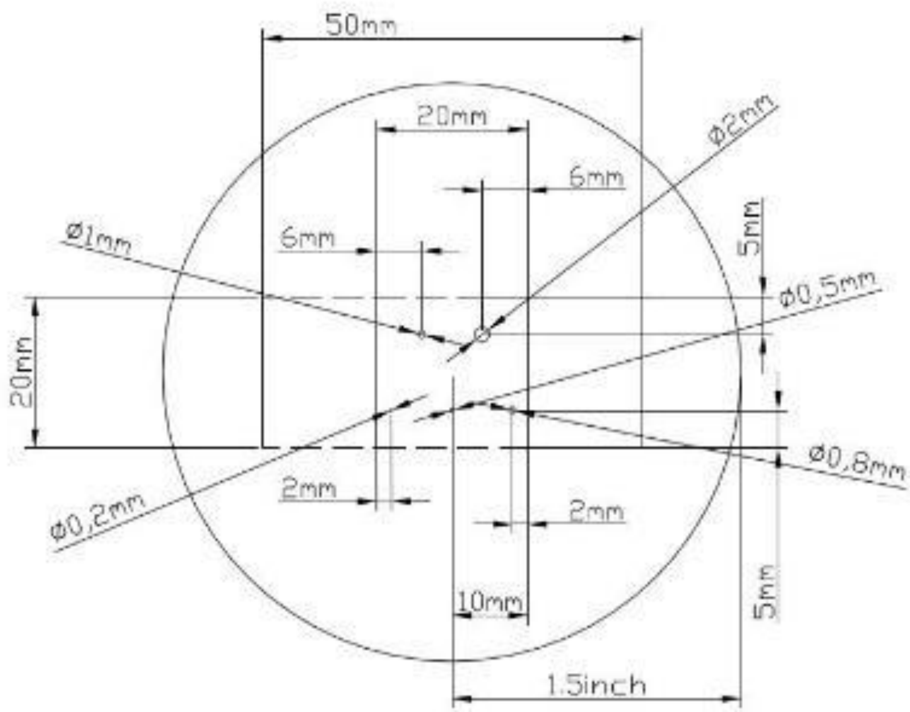

Figure 5.4. Hydrophobic circular pattern on hydrophilic surface with 0.2 mm, 0.5 mm, 0.8 mm, 1 mm and 2 mm in diameter

Table 5.1. Parameters of bubble departure on different surface conditions

Diameter of pattern hydrophobic spots (mm)	Actual average diameter measured under microscope (mm)	Min and Max bubble base diameter (mm)	Bubble departure diameter (mm)	Bubble departure volume (ul)	Bubble contact angle change (deg.)	Bubble departure frequency (Hz)
0.2	0.34-0.38 (0.36)	0-0.6	2.2	8	50-70	4-11
0.5	0.62-0.66 (0.64)	0-0.82	2.6	10.21	50-90	
0.8	0.86-0.9 (0.88)	0.4-0.96	2.85	12		
1	1.2-1.24 (1.22)	0.9-1.12	3	16.5	50-110	
2	2.22-2.26 (2.24)	0.97-1.55	3.3	21		
Hydrophilic	NA	0-0.5	2.0	8	30-70	59-66
Hydrophobic (120 deg.)	NA	1-3		Around 50*	70-130	0.5-1
Hydrophobic (110 deg.)	NA	0.5-1.2	3.7	23	50-120	1.25-2

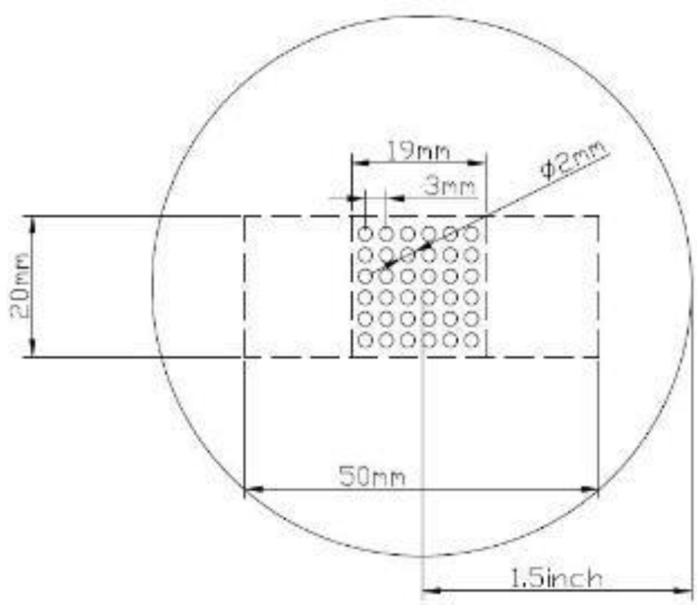

Figure 5.5. Pattern arrays with 2 mm in diameter

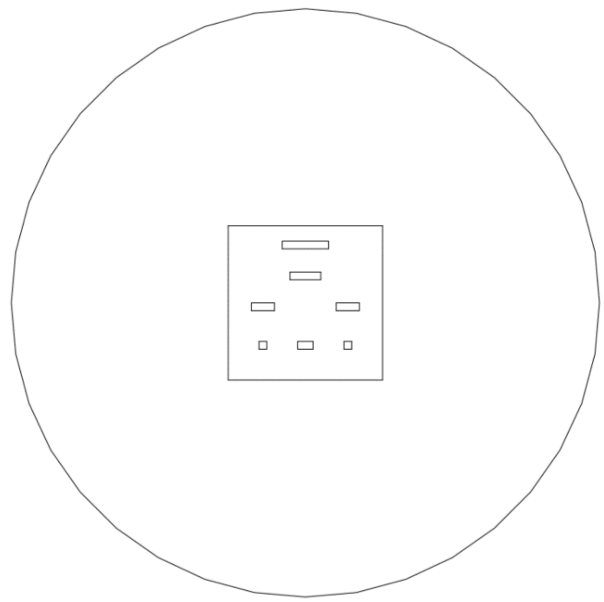

Figure 5.6. Hydrophobic rectangular patterns on hydrophilic surface with size varies from 1 mm*1 mm, 1 mm*2 mm, 1 mm*3 mm, 1 mm*4 mm and 1 mm*6 mm.

For rectangular-like hydrophobic pattern, the bubble growth was only limited by one dimension. The release of the other dimension endowed more bubble expansion flexibility and make liquid rewet possible under EW effect along that direction. The bubble growth evolutionary plot were given in Fig.5.7 and Fig. 5.8. The growth rates were compared in Table 5.2 for four different surface conditions: Hydrophobic surface, Hydrophilic surface, hydrophilic surface with 1 mm*3 mm pattern and hydrophilic surface with 1 mm*3 mm pattern under EW actuation.

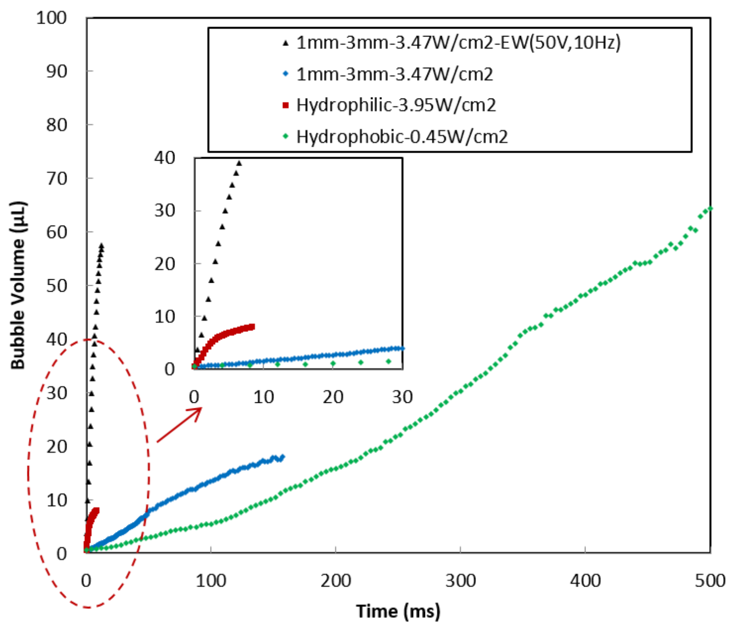

Figure 5.7. bubble volume evolution in one ebullition cycle on hydrophobic surface, hydrophilic surface, 1 mm*3 mm rectangular pattern and 1 mm*3 mm rectangular pattern with EW at 3.47 W/cm^2

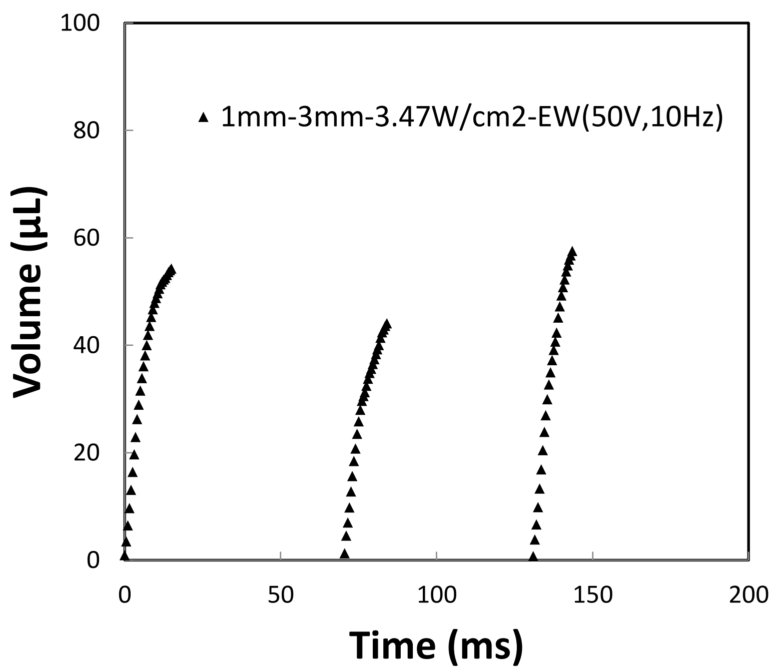

Figure 5.8. Bubble volume evolution in consecutive ebullition cycles on 1 mm*3 mm rectangular pattern with EW at 3.47 W/cm^2

Table 5.2. Bubble growth rate on different surface conditions

	Hydrophobic	Hydrophilic	Pattern (1 mm*3 mm)	Pattern with EW (1 mm*3 mm)
$\frac{dV}{dt}$ (μl/ms)	0.1	1	0.11	5

Chapter 6 Conclusions and Future Work

CHF represents the thermal limit of boiling heat transfer, beyond which the phase change process may transition abruptly into the inefficient film boiling regime and, moreover, catastrophic dryout can occur to endanger the safety operation of the boiling device. Thus, understanding the mechanisms of and enhancing CHF has been a long-standing challenge in heat transfer. In this dissertation work, study capitalized on the ability of using alternating current (AC) electrowetting to modulate the stabilities of liquid-vapor interface and the motion of liquid vapor-solid three-phase contact line and exploited it for the benefit of CHF augmentation. To circumvent the complexities of an actual boiling system, experiment was first carried out by choosing a Leidenfrost drop, which refers to a liquid drop hovering over a highly superheated solid surface, as a model system due to its intimate connection to film boiling and the minimum heat flux. The hypothesis was that CHF will be improved if the Leidenfrost temperature can be elevated by EW. To do so, the effect of the electric field was explored on the dynamics of the vapor film that separates the drop from the hot surface both theoretically and experimentally. It was found that the electrostatic attraction force itself cannot destabilize the film. Instead, it is the accelerated vapor flow through the film and intensified electric field that changes the critical wavelength of the Kelvin-Helmholtz instability, thus leading to the collapse of the film and an increase in the Leidenfrost point. The results show that, without the need for any complicated surface micro/nanostructures, the application of an electric field can effectively elevate the Leidenfrost point of water from 200°C to 380°C. In addition to its potential practical merits, this work offers fundamental insight into the dynamic control mechanism of CHF and film boiling in general. Then, in order to better understand the impact of EW on the liquid-vapor interfacial behaviors, Study also investigated the dynamics of EW-induced motion of both liquid droplets and vapor bubbles. A combined numerical and experimental approach was employed to scrutinize the EW response of a droplet subject to both direct current (DC) and alternating current (AC) actuating signals. Computational fluid dynamics models were developed by using the Volume of Fluid (VOF)-Continuous Surface Force (CSF) method. In particular, a dynamic contact angle model based on the molecular kinetic theory was implemented as the boundary condition at the moving contact line, which considers the effects of both the contact line friction and the pinning force. This model clarified the enduring confusions and misconceptions in the literature. The droplet shape evolution and the interfacial resonance oscillation were investigated in great details. This work will help to clear the hurdles in EW research due to the inadequacies of available numerical and theoretical methods in properly modeling the transient behaviors of EW-actuated droplets. On the bubble aspect, comparisons were made between each stage of nucleation, growth and departure of vapor bubbles on a hydrophilic surface, a hydrophobic surface both with and without the influence of EW. It revealed the effect of the electrical force of the contact line and, therefore, on the bubble dynamics. This is the first attempt in the literature that explores the application of EW in actual boiling conditions, and it opens a new venue for active control boiling heat transfer. Lastly, to demonstrate that EW can indeed enhance CHF, we devised a synchronized high-speed optical imaging and infrared (IR) thermographic technique to characterize boiling heat transfer at the CHF conditions. We obtained simultaneous measurements of the bubble dynamics and the wall temperature and heat flux distributions on the boiling surface. The results showed that CHF can be enhanced by 133% by the use of EW, which has significant technological implications since it has been estimated that a 32% increase in CHF will lead to at least a 20% power density increase in pressurized water reactors. Additionally, by considering the force balance at the contact line of a nucleate bubble, a theoretical model was developed to delineate the conditions for CHF to occur. The model predictions show very good agreement with the experimental measurements, thus attesting to its validity.

Future work 1:

The bubble oscillations at low heat flux boiling regime will agitate the surrounding fluid motions which potentially make a contribution for additional enhancement of convection in nucleate boiling. However, the due to the influence of different factors such as nucleation site density, bubble departure diameter and frequencies and coalescence of adjacent bubbles. Future work could be carried out by increasing the heating surface and create discrete artificial nucleation sites to study the EW-induced micro-convection alone.

Future work 2:

The volume growth rate on the heating surfaces reflects the energy dissipation by liquid evaporation. Hydrophobic patterned surface has achieved great heat transfer efficiency. There will be a great potential addition enhancement when the patterned surface was further enhanced via EW. However, from the early study of EW signal on circular pattern, the effect of contact angle change was trivial. But on the rectangular surface, the growth rate was largely enhanced via EW. In the future, rectangular pattern will be fabricated as pattern array to further enhance the heat transfer coefficient (HTC) a critical heat flux (CHF) in boiling apparatus.

References

Adera, S., Raj, R., Enright, R., & Wang, E. N. (2013). Non-Wetting Droplets on Hot Superhydrophilic Surfaces. *Nature Communications, 4*. doi: 10.1038/ncomms3518

Afkhami, S., & Bussmann, M. (2009). Height functions for applying contact angles to 3D VOF simulations. *International Journal for Numerical Methods in Fluids, 61*(8), 827-847. doi: 10.1002/fld.1974

Afkhami, S., Zaleski, S., & Bussmann, M. (2009). A mesh-dependent model for applying dynamic contact angles to VOF simulations. *Journal of Computational Physics, 228*(15), 5370-5389. doi: 10.1016/j.jcp.2009.04.027

Ahmed, A. B., & Hamed, M. S. (2015). Modeling of transition boiling under an impinging water jet. *International Journal of Heat and Mass Transfer, 91*, 1273-1282. doi: 10.1016/j.ijheatmasstransfer.2015.07.130

Ahn, H. S., Jo, H. J., Kang, S. H., & Kim, M. H. (2011). Effect of liquid spreading due to nano/microstructures on the critical heat flux during pool boiling. *Applied Physics Letters, 98*(7), 071908. doi: doi:

Ahn, H. S., & Kim, M. H. (2012). A review on critical heat flux enhancement with nanofluids and surface modification. *Journal of Heat Transfer, 134*(2), 024001.

Ahn, H. S., & Kim, M. H. (2012). A Review on Critical Heat Flux Enhancement With Nanofluids and Surface Modification. *Journal of Heat Transfer-Transactions of the Asme, 134*(2), 13. doi: 10.1115/1.4005065

Ahn, H. S., Lee, C., Kim, J., & Kim, M. H. (2012). The effect of capillary wicking action of micro/nano structures on pool boiling critical heat flux. *International Journal of Heat and Mass Transfer, 55*(1-3), 89-92. doi: 10.1016/j.ijheatmasstransfer.2011.08.044

Ahn, H. S., Sathyamurthi, V., & Banerjee, D. (2009). Pool Boiling Experiments on a Nano-Structured Surface. *Ieee Transactions on Components and Packaging Technologies*, *32*(1), 156-165. doi: 10.1109/tcapt.2009.2013980

Kang, K.H. (2002). How electrostatic fields change contact angle in electrowetting. *Langmuir, 18*.

Sur, A., Lu, Y., Pascente, C., Ruchhoeft, P., & Dong,L,. (2015). *Nucleated Boiling Heat Transfer Enhancement with Electrowetting*. Paper presented at the American society of thermal and fluids engineers New York.

Annapragada, S. R., Dash, S., Garimella, S. V., & Murthy, J. Y. (2011). Dynamics of Droplet Motion under Electrowetting Actuation. *Langmuir*, *27*(13), 8198-8204. doi: 10.1021/la201322b

Annapragada, S. R., Murthy, J. Y., & Garimella, S. V. (2012). Prediction of droplet dynamics on an incline. *International Journal of Heat and Mass Transfer*, *55*(5-6), 1466-1474. doi: 10.1016/j.ijheatmasstransfer.2011.10.028

Aritra, S., Lu, Y., Pascente, C., Ruchhoeft, P., & Dong,L,. (2016). *Nucleate boiling heat transfer enhancement with electrowetting*.

Ashoke Raman, K., Jaiman, R. K., Lee, T.-S., & Low, H.-T. (2016). A numerical study on electrowetting-induced jumping and transport of droplet. *International Journal of Heat and Mass Transfer, 99*, 805-821. doi:

Atefi, E., Mann, J. A., Jr., & Tavana, H. (2013). A Robust Polynomial Fitting Approach for Contact Angle Measurements. *Langmuir, 29*(19), 5677-5688. doi: 10.1021/la4002972

Bai, L., Zhang, L., Lin, G., & Peterson, G. P. (2016). Pool boiling with high heat flux enabled by a porous artery structure. *Applied Physics Letters, 108*(23), 233901. doi: doi:

Baird, E., & Mohseni, K. (2008). Digitized Heat Transfer: A New Paradigm for Thermal Management of Compact Micro Systems. *IEEE Transactions on Components and Packaging Technologies, 31*(1), 143-151. doi: 10.1109/TCAPT.2008.916810

Baret, J.-C., Decré, M. M. J., & Mugele, F. (2007). Self-Excited Drop Oscillations in Electrowetting. *Langmuir, 23*(9), 5173-5179. doi: 10.1021/la062149f

Berghmans, J. (1976). Electrostatic field and maximum heat-flux. *International Journal of Heat and Mass Transfer, 19*(7), 791-797. doi: 10.1016/0017-9310(76)90133-2

Bernardin, J. D., & Mudawar, I. (1999). The Leidenfrost point: Experimental study and assessment of existing models. *Journal of Heat Transfer-Transactions of the Asme, 121*(4), 894-903. doi: 10.1115/1.2826080

Berthoud, G. (2000). Vapor explosions. *Annual Review of Fluid Mechanics, 32*, 573-611. doi: 10.1146/annurev.fluid.32.1.573

Bhaumik, S. K., Das, S., Chakraborty, S., & DasGupta, S. (2014). Droplet transport through dielectrophoretic actuation using line electrode. *Microfluidics and Nanofluidics, 16*(3), 597-603. doi: 10.1007/s10404-013-1242-5

Bhavnani, S., Narayanan, V., Qu, W., Jensen, M., Kandlikar, S., Kim, J., & Thome, J. (2014). Boiling Augmentation with Micro/Nanostructured Surfaces: Current Status and

Research Outlook. *Nanoscale and Microscale Thermophysical Engineering, 18*(3), 197-222. doi: 10.1080/15567265.2014.923074

Biance, A. L., Clanet, C., & Quere, D. (2003). Leidenfrost drops. *Physics of Fluids, 15*(6), 1632-1637. doi: 10.1063/1.1572161

Blake, T. D. (2006). The physics of moving wetting lines. *Journal of Colloid and Interface Science, 299*(1), 1-13. doi:

Blake, T. D., Clarke, A., & Stattersfield, E. H. (2000). An Investigation of Electrostatic Assist in Dynamic Wetting. *Langmuir, 16*(6), 2928-2935. doi: 10.1021/la990973g

Blake, T. D., & Haynes, J. M. (1969). Kinetics of liquid/liquid displacement. *Journal of Colloid and Interface Science, 30*(3), 421-423. doi: 10.1016/0021-9797(69)90411-1

Brackbill, J. U., Kothe, D. B., & Zemach, C. (1992). A Continuum Method for Modeling Surface-Tension. *Journal of Computational Physics, 100*(2), 335-354. doi: 10.1016/0021-9991(92)90240-y

Bradfield, W. S. (1966). Liquid-Solid Contact in Stable Film Boiling. *Industrial & Engineering Chemistry Fundamentals, 5*(2), 200-204. doi: 10.1021/i160018a008

Bussmann, M., Mostaghimi, J., & Chandra, S. (1999). On a three-dimensional volume tracking model of droplet impact. *Physics of Fluids, 11*(6), 1406-1417. doi: doi:

Carey, V. (Second Edition). *Liquid-vapor phase-change phenomenon*.

Carey, V. P. (2008). *Liquid-vapor phase-change phenomena* (Second ed.).

Carrica, P., DiMarco, P., & Grassi, W. (1996). Electric field effects on film boiling on a wire. *Experimental Heat Transfer, 9*(1), 11-27.

Celestini, F., & Kirstetter, G. (2012). Effect of an electric field on a Leidenfrost droplet. *Soft Matter*, *8*(22), 5992-5995. doi: 10.1039/c2sm25656h

Cha, G., Kim, C.-J., & Ju, Y. S. (2016). Thermal conductance switching based on the actuation of liquid droplets through the electrowetting on dielectric (EWOD) phenomenon. *Applied Thermal Engineering*, *98*, 189-195. doi:

Chang, Y. (1961). An Analysis of the Critical Conditions and Burnout in Boiling Heat Transfer.

Chatterjee, D., Shepherd, H., & Garrell, R. L. (2009). Electromechanical model for actuating liquids in a two-plate droplet microfluidic device. *Lab on a Chip, 9*(9), 1219-1229. doi: 10.1039/b901375j

Chen, L., & Bonaccurso, E. (2014). Electrowetting -- from statics to dynamics. *Advances in colloid and interface science*, *210*, 2-12. doi: 10.1016/j.cis.2013.09.007

Chen, R., Lu, M.-C., Srinivasan, V., Wang, Z., Cho, H. H., & Majumdar, A. (2009). Nanowires for Enhanced Boiling Heat Transfer. *Nano Letters*, *9*(2), 548-553. doi: 10.1021/nl8026857

Chu, K.-H., Enright, R., & Wang, E. N. (2012). Structured surfaces for enhanced pool boiling heat transfer. *Applied Physics Letters, 100*(24), 241603. doi: doi:

Chu, K.-H., Soo Joung, Y., Enright, R., Buie, C. R., & Wang, E. N. (2013). Hierarchically structured surfaces for boiling critical heat flux enhancement. *Applied Physics Letters*, *102*(15), 151602. doi: doi:

Chu, K. H., Joung, Y. S., Enright, R., Buie, C. R., & Wang, E. N. (2013). Hierarchically structured surfaces for boiling critical heat flux enhancement. *Applied Physics Letters, 102*(15). doi: 10.1063/1.4801811

Cox, R. G. (1986a). The Dynamics of the Spreading of Liquids on a Solid-Surface, I. Viscous Flow. *Journal of Fluid Mechanics, 168,* 169-194. doi: 10.1017/s0022112086000332

Cox, R. G. (1986b). The dynamics of the spreading of liquids on a solid surface. Part 1. Viscous flow. *Journal of Fluid Mechanics, 168*, 169-194.

Cox, R. G. (1998). Inertial and viscous effects on dynamic contact angles. *Journal of Fluid Mechanics*, *357*, 249-278. doi: 10.1017/s0022112097008112

Dash, S., Kumari, N., & Garimella, S. V. (2012). Frequency-dependent transient response of an oscillating electrically actuated droplet. *Journal of Micromechanics and Microengineering, 22*(7). doi: 10.1088/0960-1317/22/7/075004

Decamps, C., & De Coninck, J. (2000). Dynamics of spontaneous spreading under electrowetting conditions. *Langmuir, 16*(26), 10150-10153. doi: 10.1021/la000590e

Dhillon, N. S., Buongiorno, J., & Varanasi, K. K. (2015). Critical heat flux maxima during boiling crisis on textured surfaces. *Nature Communications, 6*, 8247. doi: 10.1038/ncomms9247

Dhir, V. K., & Liaw, S. P. (1989). Framework for a Unified Model for Nucleate and Transition Pool Boiling. *Journal of Heat Transfer-Transactions of the Asme, 111*(1-4), 739-746.

Dupeux, G., Bourrianne, P., Magdelaine, Q., Clanet, C., & Quere, D. (2014). Propulsion on a superhydrophobic ratchet. *Scientific Reports, 4*. doi: 10.1038/srep05280

Dussan, E. B. (1979). On the Spreading of Liquids on Solid Surfaces: Static and Dynamic Contact Lines. *Annual Review of Fluid Mechanics, 11*(1), 371-400. doi: 10.1146/annurev.fl.11.010179.002103

Mugele, F. & Baret, J.C (2005). Electrowetting:from basics to applications. *Journal of physics: condensed matter*.

Forster, H. K., & Zuber, N. (1955). Dynamics of vapor bubbles and boiling heat transfer. *AIChE Journal, 1*(4), 531-535. doi: 10.1002/aic.690010425

Frenkel, J. I. (1946). *Kinetic Theory of Liquids*. Oxford: Oxford University Press.

Tomar, G., Biswas, G., Sharma, A. & Welch, S.W.J. (2009). Influence of electric field on saturated film boiling. *Physics of Fluids*.

Galloway, J. E., & Mudawar, I. (1993). CHF MECHANISM IN FLOW BOILING FROM A SHORT HEATED WALL .1. EXAMINATION OF NEAR-WALL CONDITIONS WITH THE AID OF PHOTOMICROGRAPHY AND HIGH-SPEED VIDEO IMAGING. *International Journal of Heat and Mass Transfer, 36*(10), 2511-2526. doi: 10.1016/s0017-9310(05)80190-5

Gambill, W. R., & Lienhard, J. H. (1989). An Upper Bound for the Critical Boiling Heat Flux. *Journal of Heat Transfer-Transactions of the Asme, 111*(1-4), 815-818.

Garimella, S. V., Persoons, T., Weibel, J., & Yeh, L.-T. (2013). Technological drivers in data centers and telecom systems: Multiscale thermal, electrical, and energy management. *Applied Energy, 107*, 66-80. doi:

Glasstone, S., Laidler, K. J., Eyring, H. J. (1941). *The Theory of Rate Processes*. New York: McGraw-Hill.

Gottfried, B. S., Lee, C. J., & Bell, K. J. (1966). Leidenfrost phenomenon-film boiling of liquid droplets on a flat plate. *International Journal of Heat and Mass Transfer*, *9*(11), 1167. doi: 10.1016/0017-9310(66)90112-8

Hale, R. S., & Bahadur, V. (2015). Electrowetting Heat Pipes for Heat Transport Over Extended Distances. *IEEE Transactions on Components, Packaging and Manufacturing Technology, 5*(10), 1441-1450. doi: 10.1109/TCPMT.2015.2472363

Hao, Y., & Prosperetti, A. (1999). The effect of viscosity on the spherical stability of oscillating gas bubbles. *Physics of Fluids*, *11*(6), 1309-1317. doi: 10.1063/1.869996

Haramura, Y., & Katto, Y. (1983a). A NEW HYDRODYNAMIC MODEL OF CRITICAL HEAT-FLUX, APPLICABLE WIDELY TO BOTH POOL AND FORCED-CONVECTION BOILING ON SUBMERGED BODIES IN SATURATED LIQUIDS. *International Journal of Heat and Mass Transfer, 26*(3), 389-399. doi: 10.1016/0017-9310(83)90043-1

Haramura, Y., & Katto, Y. (1983b). A new hydrodynamic model of critical heat-flux, application widely to both pool and forced-convection boiling on submerged bodies in saturated liquids. *International Journal of Heat and Mass Transfer, 26*(3), 389-399. doi: 10.1016/0017-9310(83)90043-1

Hayes, R. A., & Feenstra, B. J. (2003). Video-speed electronic paper based on electrowetting. *Nature, 425*(6956), 383-385. doi: 10.1038/nature01988

Hirt, C. W., & Nichols, B. D. (1981). Volume of fluid (VOF) method for the dynamics of free boundaries. *Journal of Computational Physics, 39*(1), 201-225. doi:

Hoffman, R. L. (1975). A study of the advancing interface. I. Interface shape in liquid—gas systems. *Journal of Colloid and Interface Science, 50*(2), 228-241. doi:

Hong, J., Kim, Y. K., Kang, K. H., Kim, J., & Lee, S. J. (2014). Effects of drop viscosity on oscillation dynamics induced by AC electrowetting. *Sensors and Actuators B-Chemical, 190*, 48-54. doi: 10.1016/j.snb.2013.08.057

Hong, J., Kim, Y. K., Kang, K. H., Oh, J. M., & Kang, I. S. (2013). Effects of Drop Size and Viscosity on Spreading Dynamics in DC Electrowetting. *Langmuir, 29*(29), 9118-9125. doi: 10.1021/la401801u

Hong, J. S., Ko, S. H., Kang, K. H., & Kang, I. S. (2007). A numerical investigation on AC electrowetting of a droplet. *Microfluidics and Nanofluidics, 5*(2), 263-271. doi: 10.1007/s10404-007-0246-4

Hong, S. J., Hong, J., Seo, H. W., Lee, S. J., & Chung, S. K. (2015). Fast Electrically Driven Capillary Rise Using Overdrive Voltage. *Langmuir, 31*(51), 13718-13724. doi: 10.1021/acs.langmuir.5b02921

Hsu, Y. Y. (1962). On the size range of active nucleation cavities on a heating surface. *Journal of Heat Transfer, 84*.

Hwang, G. S., & Kaviany, M. (2006). Critical heat flux in thin, uniform particle coatings. *International Journal of Heat and Mass Transfer, 49*(5-6), 844-849. doi: 10.1016/j.ijheatmasstransfer.2005.09.020

Jeong, J. H., & Kwon, Y. C. (2006). Effects of ultrasonic vibration on subcooled pool boiling critical heat flux. *Heat and Mass Transfer, 42*(12), 1155-1161. doi: 10.1007/s00231-005-0079-1

JG, L. (1756). Aquae communis nonnullis qualitatibus tractatus.

Jo, H., Kaviany, M., Kim, S. H., & Kim, M. H. (2014). Heterogeneous bubble nucleation on ideally-smooth horizontal heated surface. *International Journal of Heat and Mass Transfer, 71*, 149-157. doi: 10.1016/j.ijheatmasstransfer.2013.12.040

Johnson, R. L. (1968). Effect of an electric field on boiling heat transfer. *AIAA Journal, 6*(8), 1456. doi: 10.2514/3.4788

Jones, T. B. (2009). More about the electromechanics of electrowetting. *Mechanics Research Communications, 36*(1), 2-9. doi: 10.1016/j.mechrescom.2008.08.012

Jones, T. B., Fowler, J. D., Chang, Y. S., & Kim, C. J. (2003). Frequency-based relationship of electrowetting and dielectrophoretic liquid microactuation. *Langmuir, 19*(18), 7646-7651. doi: 10.1021/la0347511

Jones, T. B., Wang, K. L., & Yao, D. J. (2004). Frequency-dependent electromechanics of aqueous liquids: Electrowetting and dielectrophoresis. *Langmuir, 20*(7), 2813-2818.

Jun, S., Kim, J., Son, D., Kim, H. Y., & You, S. M. (2016). Enhancement of Pool Boiling Heat Transfer in Water Using Sintered Copper Microporous Coatings. *Nuclear Engineering and Technology, 48*(4), 932-940. doi:

Kandlikar, S. G. (2001). A theoretical model to predict pool boiling CHF incorporating effects of contact angle and orientation. *Journal of Heat Transfer-Transactions of the Asme, 123*(6), 1071-1079. doi: 10.1115/1.1409265

Kang, K. H. (2002). How electrostatic fields change contact angle in electrowetting. *Langmuir, 18*(26), 10318-10322. doi: 10.1021/la0263615

Keshavarz-Motamed, Z., Kadem, L., & Dolatabadi, A. (2010). Effects of dynamic contact angle on numerical modeling of electrowetting in parallel plate microchannels. *Microfluidics and Nanofluidics, 8*(1), 47-56. doi: 10.1007/s10404-009-0460-3

Kim, D. E., Yu, D. I., Jerng, D. W., Kim, M. H., & Ahn, H. S. (2015). Review of boiling heat transfer enhancement on micro/nanostructured surfaces. *Experimental Thermal and Fluid Science, 66,* 173-196. doi:

Kim, H., Truong, B., Buongiorno, J., & Hu, L. W. (2011). On the effect of surface roughness height, wettability, and nanoporosity on Leidenfrost phenomena. *Applied Physics Letters, 98*(8). doi: 10.1063/1.3560060

Kim, J. M., Kang, S. H., Yu, D. I., Park, H. S., Moriyama, K., & Kim, M. H. (2017). Smart surface in flow boiling: Spontaneous change of wettability. *International Journal of Heat and Mass Transfer, 105,* 147-156. doi: 10.1016/j.ijheatmasstransfer.2016.09.047

Kim, S. H., Ahn, H. S., Kim, J., Kaviany, M., & Kim, M. H. (2013). Dynamics of water droplet on a heated nanotubes surface. *Applied Physics Letters, 102*(23). doi: 10.1063/1.4809944

Kim, S. J., Bang, I. C., Buongiorno, J., & Hu, L. W. (2007). Surface wettability change during pool boiling of nanofluids and its effect on critical heat flux. *International Journal of Heat and Mass Transfer, 50*(19-20), 4105-4116. doi: 10.1016/j.ijheatmasstransfer.2007.02.002

Klausner, J. F., Mei, R., Bernhard, D. M., & Zeng, L. Z. (1993). Vapor Bubble Departure in Forced-Convection Boiling. *International Journal of Heat and Mass Transfer, 36*(3), 651-662. doi: 10.1016/0017-9310(93)80041-r

Ko, Lee, & Kang. (2009). A synthetic jet produced by electrowetting-driven bubble oscillations

in aqueous solution. *Applied Physics Letters, 94*.

Kuiper, S., & Hendriks, B. H. W. (2004). Variable-focus liquid lens for miniature cameras. *Applied Physics Letters, 85*(7), 1128-1130. doi: 10.1063/1.1779954

Kutatelasze, S. S. (1948). On the Transition to Film Boiling under Natural Convection. *Kotloturbostroenie*, 10.

Kwon, H. M., Bird, J. C., & Varanasi, K. K. (2013). Increasing Leidenfrost point using micro-nano hierarchical surface structures. *Applied Physics Letters, 103*(20). doi: 10.1063/1.4828673

L, R. (1917). On the pressure developed in a liquid during the collapse of a spherical cavity. *Philos.Mag., 34*.

Lamb, H. (1932). *Hydrodynamics*. New York: Cambridge University Press.

Lee, J. H., Lee, T., & Jeong, Y. H. (2012). Experimental study on the pool boiling CHF enhancement using magnetite-water nanofluids. *International Journal of Heat and Mass Transfer, 55*(9-10), 2656-2663. doi: 10.1016/j.ijheatmasstransfer.2011.12.027

Li, X. L., He, G. W., & Zhang, X. (2013). Numerical simulation of drop oscillation in AC electrowetting. *Science China-Physics Mechanics & Astronomy, 56*(2), 383-394. doi: 10.1007/s11433-012-4986-0

Li, Z., Zhou, Z. W., & Hu, G. H. (2012). Dissipative Particle Dynamics Simulation of Droplet Oscillations in AC Electrowetting. *Journal of Adhesion Science and Technology, 26*(12-17), 1883-1895. doi: 10.1163/156856111x600217

Lienhard, J. H., & Dhir, V. K. (1973). Hydrodynamic prediction of peak pool-boiling heat fluxes from finite bodies. *Journal of Heat Transfer-Transactions of the Asme, 95*(2), 152-158.

Lienhard, J. H., & Hasan, M. (1979). Prediction Boiling Burout with the Mechanical Energy Stability-cretirion. *Journal of Heat Transfer-Transactions of the Asme, 101*(2), 276-279.

Liter, S. G., & Kaviany, M. (2001). Pool-boiling CHF enhancement by modulated porous-layer coating: theory and experiment. *International Journal of Heat and Mass Transfer, 44*(22), 4287-4311. doi: 10.1016/s0017-9310(01)00084-9

Lu, M. (2010). Exploring the Limits of Boiling and Evaporative Heat Transfer Using Micro/Nano Structures.

Lu, M. C., Chen, R. K., Srinivasan, V., Carey, V., & Majumdar, A. (2011). Critical heat flux of pool boiling on Si nanowire array-coated surfaces. *International Journal of Heat and Mass Transfer, 54*(25-26), 5359-5367. doi: 10.1016/j.ijheatmasstransfer.2011.08.007

Lu, M. C., Huang, C. H., Huang, C. T., & Chen, Y. C. (2015). A modified hydrodynamic model for pool boiling CHF considering the effects of heater size and nucleation site density. *International Journal of Thermal Sciences, 91*, 133-141. doi: 10.1016/j.ijthermalsci.2015.01.011

Lu, Y.-W., & Kandlikar, S. G. (2011). Nanoscale Surface Modification Techniques for Pool Boiling Enhancement—A Critical Review and Future Directions. *Heat Transfer Engineering, 32*(10), 827-842.

Lu, Y., Sur, A., Pascente, C., Annapragada, S. R., Ruchhoeft, P., & Liu, D. (2017). Dynamics of droplet motion induced by Electrowetting. *International Journal of Heat and Mass Transfer, 106*.

Lu, Y., Sur, A., Pascente, C., Ruchhoeft, P., and Liu, D. (2016). *Enhancing critical heat flux with electrowetting.* Paper presented at the ASME 2016 International Mechanical Engineering Congress & Exposition, Phoenix, AZ.

Lunkad, S. F., Buwa, V. V., & Nigam, K. D. P. (2007). Numerical simulations of drop impact and spreading on horizontal and inclined surfaces. *Chemical Engineering Science, 62*(24), 7214-7224. doi: 10.1016/j.ces.2007.07.036

Maeng, Y. H., Song, S. L., & Lee, J. Y. (2016). Unaffectedness of improved wettability on critical heat flux enhancement with TiO2 sputtered surface. *Applied Physics Letters, 108*(7). doi: 10.1063/1.4942094

Mahadevan, L., & Pomeau, Y. (1999). Rolling droplets. *Physics of Fluids, 11*(9), 2449-2453. doi: 10.1063/1.870107

Marco, P. D., & Grassi, W. (1993). Saturated Pool Boiling Enhancement by Means of an Electric Field. *Journal of Enhanced Heat Transfer, 1*.

Mochizuki, M., Singh, R., Nguyen, T., & Nguyen, T. (2014). Heat pipe based passive emergency core cooling system for safe shutdown of nuclear power reactor. *Applied Thermal Engineering, 73*(1), 699-706. doi: 10.1016/j.applthermaleng.2014.07.004

MS., P., & A., P. (1977). Bubble Dynamics and Cavitation. *Ann. Rev. Fluid Mech., 9*.

Mugele, F., Baret, J.-C., & Steinhauser, D. (2006). Microfluidic mixing through electrowetting-induced droplet oscillations. *Applied Physics Letters, 88*(20), 204106. doi: doi:

Mugele, F., & Baret, J. C. (2005). Electrowetting: From basics to applications. *Journal of Physics-Condensed Matter, 17*(28), R705-R774.

Ng, B. T., Hung, Y. M., & Tan, M. K. (2015). Suppression of the Leidenfrost effect via low frequency vibrations. *Soft Matter, 11*(4), 775-784. doi: 10.1039/c4sm02272f

Ng, B. T., Hung, Y. M., & Tan, M. K. (2016). Acoustically-controlled Leidenfrost droplets. *Journal of Colloid and Interface Science, 465*, 26-32. doi: 10.1016/j.jcis.2015.11.047

Nichita, B. A., Zun, I., Thome, J. R. (2010). *A VOF method coupled with a dynamic contact angle model for simulation of two-phase flows with partial wetting*. Paper presented at the 7th International Conference on Multiphase Flow, Tampa, Florida.

O'Hanley, H., Coyle, C., Buongiorno, J., McKrell, T., Hu, L. W., Rubner, M., & Cohen, R. (2013). Separate effects of surface roughness, wettability, and porosity on the boiling critical heat flux. *Applied Physics Letters, 103*(2), 5. doi: 10.1063/1.4813450

Ogata, K. (2003). *System Dynamics*: Pearson.

Oh, J. M., Ko, S. H., & Kang, K. H. (2008). Shape Oscillation of a Drop in ac Electrowetting. *Langmuir, 24*(15), 8379-8386. doi: 10.1021/la8007359

Oh, J. M., Ko, S. H., & Kang, K. H. (2010). Analysis of electrowetting-driven spreading of a drop in air. *Physics of Fluids, 22*(3). doi: 10.1063/1.3360331

Oh, J. M., Legendre, D., & Mugele, F. (2012). Shaken not stirred —On internal flow patterns in oscillating sessile drops. *EPL, 98*(3).

Paneru, M., Priest, C., Sedev, R., & Ralston, J. (2010). Static and Dynamic Electrowetting of an Ionic Liquid in a Solid/Liquid/Liquid System. *Journal of the American Chemical Society, 132*(24), 8301-8308. doi: 10.1021/ja9106397

Park, S. D., & Bang, I. C. (2014). Experimental study of a universal CHF enhancement mechanism in nanofluids using hydrodynamic instability. *International Journal of Heat and Mass Transfer, 70*, 844-850. doi: 10.1016/j.ijheatmasstransfer.2013.11.066

Piroird, K., Clanet, C., & Quere, D. (2012). Magnetic control of Leidenfrost drops. *Physical Review E, 85*(5). doi: 10.1103/PhysRevE.85.056311

Plesset, M. S., & Prosperetti, A. (1977). BUBBLE DYNAMICS AND CAVITATION. *Annual Review of Fluid Mechanics, 9*, 145-185. doi: 10.1146/annurev.fl.09.010177.001045

Quan, X. J., Dong, L. N., & Cheng, P. (2014). A CHF model for saturated pool boiling on a heated surface with micro/nano-scale structures. *International Journal of Heat and Mass Transfer, 76*, 452-458. doi: 10.1016/j.ijheatmasstransfer.2014.04.037

Quere, D. (2013). Leidenfrost Dynamics. In S. H. Davis & P. Moin (Eds.), *Annual Review of Fluid Mechanics, Vol 45* (Vol. 45, pp. 197-215).

Ranabothu, S. R., Karnezis, C., & Dai, L. L. (2005). Dynamic wetting: Hydrodynamic or molecular-kinetic? *Journal of Colloid and Interface Science, 288*(1), 213-221. doi:

Renardy, M., Renardy, Y., & Li, J. (2001). Numerical Simulation of Moving Contact Line Problems Using a Volume-of-Fluid Method. *Journal of Computational Physics, 171*(1), 243-263. doi:

Rohsenow. (1951). *A method of correlating heat transfer data for surface boiling of liquids* (Vol. 74).

Roisman, I. V., Opfer, L., Tropea, C., Raessi, M., Mostaghimi, J., & Chandra, S. (2008). Drop impact onto a dry surface: Role of the dynamic contact angle. *Colloids and Surfaces a-Physicochemical and Engineering Aspects, 322*(1-3), 183-191. doi: 10.1016/j.colsurfa.2008.03.005

Roques-Carmes, T., Hayes, R. A., & Schlangen, L. J. M. (2004). A physical model describing the electro-optic behavior of switchable optical elements based on electrowetting. *Journal of Applied Physics, 96*(11), 6267-6271. doi: 10.1063/1.1810192

Schneemilch, M., Hayes, R. A., Petrov, J. G., & Ralston, J. (1998). Dynamic Wetting and Dewetting of a Low-Energy Surface by Pure Liquids. *Langmuir, 14*(24), 7047-7051. doi: 10.1021/la980476k

Sen, P., & Kim, C.-J. C. (2009). Capillary Spreading Dynamics of Electrowetted Sessile Droplets in Air. *Langmuir, 25*(8), 4302-4305. doi: 10.1021/la900077u

SG, K. (2001). A Theoretical Model to Predict Pool Boiling CHF Incorporating Effects of Contact Angle and Orientation. *Journal of Heat Transfer, 123,* 1071-1079.

Shahriari, A., Hermes, M., & Bahadur, V. (2016a). Electrical control and enhancement of boiling heat transfer during quenching. *Applied Physics Letters, 108*(9). doi: 10.1063/1.4943230

Shahriari, A., Hermes, M., & Bahadur, V. (2016b). Electrical control and enhancement of boiling heat transfer during quenching. *Applied Physics Letters*, *108*(9), 5. doi: 10.1063/1.4943230

Shahriari, A., Wurz, J., & Bahadur, V. (2014). Heat Transfer Enhancement Accompanying Leidenfrost State Suppression at Ultrahigh Temperatures. *Langmuir, 30*(40), 12074-12081. doi: 10.1021/la502456d

Shojaeian, M., & Koşar, A. (2015). Pool boiling and flow boiling on micro- and nanostructured surfaces. *Experimental Thermal and Fluid Science*, *63*, 45-73. doi:

Sikalo, S., Tropea, C., & Ganic, E. N. (2005). Dynamic wetting angle of a spreading droplet. *Experimental Thermal and Fluid Science*, *29*(7), 795-802. doi: 10.1016/j.expthermflusci.2005.03.006

SK, C. (2010). Bubble actuation by electrowetting-on-dielectric (EWOD) and its applications: A review. *International Journal of Precision Engineering and Manufacturing*, *11*.

Stratton, J. A. Electromagnetic theory, chapter 2.

Sur, A. (2014). *An experimental investigation of electrowetting modulated nucleate boiling.* (Ph.D.), University of Houston, Houston, TX.

Sur, A., & Liu, D. (2012). Adiabatic air-water two-phase flow in circular microchannels. *International Journal of Thermal Sciences*, *53*, 18-34. doi: 10.1016/j.ijthermalsci.2011.09.021

Sur, A., Lu, Y., Pascente, C., Ruchhoeft, P., and Liu, D. (2016). Nucleate boiling heat transfer enhancement with electrowetting. *Journal of Heat Transfer, in review.*

Takata, Y., Hidaka, S., Cao, J. M., Nakamura, T., Yamamoto, H., Masuda, M., & Ito, T. (2005). Effect of surface wettability on boiling and evaporation. *Energy, 30*(2-4), 209-220. doi: 10.1016/j.energy.2004.05.004

Takata, Y., Hidaka, S., Masuda, M., & Ito, T. (2003). Pool boiling on a superhydrophilic surface. *International Journal of Energy Research, 27*(2), 111-119. doi: 10.1002/er.861

Tanaka, H. (1988). On the stability of vapor film in pool film boiling. *International Journal of Heat and Mass Transfer, 31*(1), 129-134.

Tanner, L. H. (1979). The spreading of silicone oil drops on horizontal surfaces. *Journal of Physics D: Applied Physics, 12*(9), 1473.

Tran, T., Staat, H. J. J., Prosperetti, A., Sun, C., & Lohse, D. (2012). Drop Impact on Superheated Surfaces. *Physical Review Letters, 108*(3). doi: 10.1103/PhysRevLett.108.036101

Tran, T., Staat, H. J. J., Susarrey-Arce, A., Foertsch, T. C., van Houselt, A., Gardeniers, H., Prosperetti, A. Lohse, D. & Sun, C. (2013). Droplet impact on superheated micro-structured surfaces. *Soft Matter, 9*(12), 3272-3282. doi: 10.1039/c3sm27643k

Vakarelski, I. U., Patankar, N. A., Marston, J. O., Chan, D. Y. C., & Thoroddsen, S. T. (2012). Stabilization of Leidenfrost vapour layer by textured superhydrophobic surfaces. *Nature, 489*(7415), 274-277. doi: 10.1038/nature11418

Verplaetsen, F., & Berghmans, J. A. (1997). Study of the influence of an electric field on the liquid-vapor interface during film boiling of stagnant fluids. *Ieee Transactions on Industry Applications, 33*(6), 1512-1518. doi: 10.1109/28.649963

Verplaetsen, F. M., & Berghmans, J. A. (1999). Film boiling of an electrically insulating fluid in the presence of an electric field. *Heat and Mass Transfer, 35*(3), 235-241. doi: 10.1007/s002310050319

Voinov, O. V. Hydrodynamics of wetting. *Fluid Dynamics, 11*(5), 714-721. doi: 10.1007/BF01012963

Grassi, W., & Testi, D. (2006). Heat Transfer Enhancement by Electric Fields in Several Heat Exchange Regimes. In N. Y. A. o. sciences (Ed.), (Vol. 1077).

Welch, S.W.J. (2007). Direct simulation of film boiling including electrohydrodynamic forces. *Physics of Fluids, 19*.

Wachters, L. H., & Westerli.Na. (1966). HEAT TRANSFER FROM A HOT WALL TO IMPINGING WATER DROPS IN SPHEROIDAL STATE. *Chemical Engineering Science, 21*(11), 1047-&. doi: 10.1016/0009-2509(66)85100-x

Walker, S. W., Shapiro, B., & Nochetto, R. H. (2009). Electrowetting with contact line pinning: Computational modeling and comparisons with experiments. *Physics of Fluids, 21*(10), 102103. doi: doi:

Wang, H., Peterson, R., & Asme. (2007). *Flow boiling enhancement in microchannels with diffusion bonded wire mesh*.

Wang, K. L., & Jones, T. B. (2005). Electrowetting dynamics of microfluidic actuation. *Langmuir, 21*(9), 4211-4217. doi: 10.1021/la0468702

Wang, K. L., Jones, T. B., & Raisanen, A. (2007). Dynamic control of DEP actuation and droplet dispensing. *Journal of Micromechanics and Microengineering, 17*(1), 76-80. doi: 10.1088/0960-1317/17/1/010

Wang, X. D., Peng, X. F., & Lee, D. Z. (2003). Dynamic wetting and stress singularity on contact line. *Science in China Series E-Technological Sciences*, *46*(4), 407-417. doi: 10.1360/02ye0407

Welch, S. W. J., & Biswas, G. (2007). Direct simulation of film boiling including electrohydrodynamic forces. *Physics of Fluids, 19*(1). doi: 10.1063/1.2433995

Wendelstorf, J., Spitzer, K. H., & Wendelstorf, R. (2008). Spray water cooling heat transfer at high temperatures and liquid mass fluxes. *International Journal of Heat and Mass Transfer, 51*(19-20), 4902-4910. doi: 10.1016/j.ijheatmasstransfer.2008.01.032

Woodson, H. H., & Melcher, J. R. (1968). Electromechanical Dynamics Part 2 Chapter 8.

Y, Z., & SK, C. (2006). Micro air bubble manipulation by electrowetting on dielectric (EWOD):

transporting, splitting, merging and eliminating of bubbles. *Lab on a Chip, 7*.

Yih, C. S. (1968). Stability of a Horizontal Fluid Interface in a Periodic Vertical Electric Field. *Physics of Fluids, 11*(7), 1447-&. doi: 10.1063/1.1692127

Yokoi, K., Vadillo, D., Hinch, J., & Hutchings, I. (2009). Numerical studies of the influence of the dynamic contact angle on a droplet impacting on a dry surface. *Physics of Fluids, 21*(7). doi: 10.1063/1.3158468

Yoshimitsu, Z., Nakajima, A., Watanabe, T., & Hashimoto, K. (2002). Effects of surface structure on the hydrophobicity and sliding behavior of water droplets. *Langmuir, 18*(15), 5818-5822. doi: 10.1021/la020088p

Zuber, N. (1959). Hydrodynamic aspects of boiling heat transfer.